GEOMETRY AND FLUENCE EFFECTS ON PHOTOREFRACTIVE POLYMER DEVICES FOR HOLOGRAPHY

by

Brittany Lynn

A Dissertation Submitted to the Faculty of the

DEPARTMENT OF OPTICAL SCIENCES

In Partial Fulfillment of the Requirements
For the Degree of

DOCTOR OF PHILOSOPHY

In the Graduate College

THE UNIVERSITY OF ARIZONA

2015

THE UNIVERSITY OF ARIZONA
GRADUATE COLLEGE

As members of the Dissertation Committee, we certify that we have read the dissertation prepared by Brittany Lynn, titled Geometry and Sensitization Effects on Photorefractive Polymer Devices and recommend that it be accepted as fulfilling the dissertation requirement for the Degree of Doctor of Philosophy.

____ Date: April 22, 2015
Nasser Peyghambarian

____ Date: April 22, 2015
Robert A. Norwood

____ Date: April 22, 2015
Ewan Wright

Final approval and acceptance of this dissertation is contingent upon the candidate's submission of the final copies of the dissertation to the Graduate College.

I hereby certify that I have read this dissertation prepared under my direction and recommend that it be accepted as fulfilling the dissertation requirement.

____ Date: April 22, 2015
Dissertation Director: Nasser Peyghambarian

____ Date: April 22, 2015
Dissertation Director: Robert A. Norwood

STATEMENT BY AUTHOR

SIGNED: Brittany Lynn

ACKNOWLEDGEMENTS

The work performed here and the scientist that I have become would not have been possible without the remarkable mentors that I have encountered during my years at the College of Optical Sciences. I want to thank Prof. N. Peyhambarian and Prof. Robert Norwood for the opportunity to study such an exciting and diverse field. The support that they have provided in publications and conferences have been phenomenal opportunities for development. I want to thank Prof. Ewan Wright for his love of teaching and for serving on my committee. Dr. Pierre-Alexandre Blanche as well has been an indispensable role model, not only for his scientific knowledge and techniques, but also in giving me the opportunities to be a mentor myself. The experience we shared in the NSF I-CORPS program was once-in-a-lifetime and I want to express my sincere gratitude for all of his support over the last five years. I also would like to thank my research colleagues Colton Bigler, Soroush Mehravar, Dmitriy Churin, Maryam Tanabal, and Ben Cromey for their contributions to this work. Special recognition goes to Alex Miles for his endless supply of interesting conversation topics and value as a scientific partner.

DEDICATION

To my family, near and far, for their support in making all of this possible.

TABLE OF CONTENTS

LIST OF FIGURES

LIST OF FIGURES

LIST OF FIGURES

ABSTRACT

This work presents the recent advances in photorefractive polymers for use in updatable holographic displays. A model with which to predict the effect of coplanar electrode geometry on diffraction uniformity in photorefractive (PR) polymer display devices was developed. Assumptions made in the standard use cases with constant electric field throughout the bulk of the media are no longer valid in the regions of extreme electric fields present in this type of device. Using electric field induced second harmonic generation (EFISHG) observed with multiphoton microscopy, the physical response in regions of internal electric fields which fall outside the standard regimes of validity were probed. Adjustments to the standard model were made, and the results of the new model were corroborated by holographic four-wave mixing measurements.

The recent development of a single mode fiber-based pulsed laser with variable pulse length, energy, and repetition rate has enabled the characterization of photorefractive devices in a previously inaccessible regime located between millisecond and nanosecond pulse recording. A pulse width range of nine orders of magnitude opens the door to device and supporting laser optimization for use in video-rate holographic display. Device optimization has resulted in 5x improvement in single pulse four-wave mixing diffraction efficiencies to 10 - 11.5 % at pulse widths ranging between 6 ns and 100 μs. The grating recording time was likewise reduced by 5x to 16 ms at an applied bias of 72.5 V/μm. These improvements support 30 Hz update rates, which combined with the 3.3 - 10 kHz repetition rate pulsed laser, pave the way for real-time updatable holographic display.

1 PHOTOREFRACTIVE POLYMERS FOR DISPLAY HOLOGRAPHY

1.1 Introduction

Holography has captured the interest of the scientific community since its invention by Dennis Gabor under the guise of an electron interference microscope.[1] In an article published in 1948, he describes a new imaging method developed while attempting to record the electron beam aberration imparted by the magnetic lens elements. In this technique, the intersection of the electron beam deviated by an object under consideration with an unaltered electron beam transmitted around the object was recorded at a location just beyond the plane of the object. The recorded image was in the form of a series of fringes, or sinusoidally varying intensity patterns which illustrated lines of constant phase between the two beams, effectively recording into a silver halide emulsion both the amplitude and direction of the wavefront that was diffracted from the object. Reconstruction by an optical field made to imitate the transmitted electron beam wavefront reproduced an image behind the film of the original object as though it was present. This work, for which Gabor was awarded the Nobel Prize in Physics in 1971, was restricted to imaging very small objects due to the limited coherence of the sources available at the time. Commercialization of the helium-neon laser in the early 1960's greatly expanded the application of holography due to the exceptional coherence lengths and narrow spectral width of laser emission, two important factors in obtaining high contrast fringes across an entire scene.

Photo-sensitive recording media were re-examined at this time in a quest to enhance hologram "brightness". Diffraction efficiency is the efficiency with which the hologram diffracts light into a single location, corresponding to the perceived hologram brightness. Appropriate materials exhibited resolution fine enough to record micron sized fringe patterns and sensitivity high enough to respond to the illumination. An additional requirement was the ability to form the material into thick films to produce thick, or volume holograms, a configuration that can approach 100 % diffraction efficiency into a single order.[2] Dichromated gelatin, initially implemented in volume holograms by Shankoff in 1968, was formed into 1.3 μm thick films and exhibited 95 % diffraction efficiency into the first order.[3] One of the disadvantages of using films made from silver halide emulsions and dichromated gelatin is that they require significant chemical processing in order to fix the holographic fringes into the material. Swelling and shrinkage of the media must also be accounted for in the development process. A photopolymer is a medium in which there is no wet processing required and shrinkage is minimized. Fixing is achieved through exposure to ultraviolet light, halting the optically induced polymerization necessary to record the hologram in these films. This allows for immediate access to the recorded hologram and a simplification of the recording procedure.[4]

The previously described range of recording media is permanent in nature, meaning that the hologram cannot be erased or rewritten. Photorefractive polymers exhibit the same high resolution and volume hologram capabilities but are also updatable and self-developing, allowing the holographer to erase the existing hologram and record another one with no decrease in efficiency or resolution. This material has thrown open the door of holography to rewritable applications ranging from dynamic imaging of scattering media to updatable three-dimensional (3D) displays.[5–8]

Recording volume holograms requires the ability to locally change the refractive index of a medium in response to incident illumination. In photorefractive polymers, this occurs as a result of three processes: 1) photons excite charges within the film in regions of high intensity; 2) the charges move in response to an externally applied electric field until they are trapped in the areas of low intensity, creating a locally varying electric field; 3) nonlinear optical molecules rotate in response to the electric field producing an oscillating refractive index modulation. The phenomenon of optically modified refractive index through localized charge redistribution was first observed in the mid 1960's by Ashkin et al. and recorded as an aside regarding their research into nonlinear optical effects in a variety of ferroelectric crystals.[9] During their experiments, they observed a transient beam deflection upon illumination of their crystals by high-intensity laser radiation that they attributed to an optically induced change of the refractive index in the region of high intensity. The magnitude of the refractive index change was found to be linearly related to the intensity of the illumination and was reversible in some of their crystals through the application of a larger, low power beam. Subsequent experiments indicated that the presence of impurities within the crystal negated the effect but also that the effect could be enhanced by applying an electric field across the crystal. The following year, Chen published results of his study on this effect as seen in potassium tantalate niobate under an applied electric field.[10] He postulated that trapped electrons within the crystal were photoexcited into the conduction band in regions of intense laser irradiation. These electrons then drifted toward the positive electrode and were trapped in the dark area, creating a space charge field between the migrated electrons and the holes they left behind, reducing the electric field within the crystal in this location. The nonlinear nature of the ferroelectric crystals led to a modulated index of refraction due to the linear electro-optic effect, or a change in the refractive index in response to an electric field. Removal of the external DC field allowed for the thermal excitation and redistribution of charges due to diffusion, healing the "damage" as he called it. Shortly afterward, he recorded an updatable volume hologram in a lithium niobate crystal, realizing diffraction efficiencies of more than 42 %.[11]

Driven by this success in inorganic photorefractive crystals, there was an effort to find an organic photorefractive alternative due to the ability of organics to exhibit large electro-optic responses, the workhorse mechanism behind photorefraction in inorganic crystals. An additional advantage to the implementation of polymers was the relative ease of polymer synthesis and large area device fabrication in contrast to the difficulty of defect-free crystal growth on similar scales. Ducharme et al. made the initial discovery of the photorefractive effect in an organic polymer in 1991, successfully recording holographic fringes into a 350µm thick film of the material.[12] This small scale prototype composite suffered from low diffraction efficiency, slow response time and a short shelf-life due to aggregation of various components, but it proved that photorefraction was possible in polymers and sparked a great deal of interest among researchers. Devices made from modern photorefractive polymers have reached 100 % diffraction efficiency, exhibit millisecond response times and have been formed into 12 inch × 12 inch active area devices a tenth of a millimeter thick.[5, 13, 14]

1.2 Basics of Grating Formation and Erasure

Holographic fringes are the result of constructive and destructive interference between two coherent beams creating a spatially varying intensity with a sinusoidal envelope. This fringe pattern is defined by the properties of the interfering beams and the space in which they interfere, namely the wavelength (λ), angle of the beams with respect to the sample normal (α_1 and α_2) and index of refraction of the medium (n). The grating vector ($\vec{K}$) relates these quantities through

$$\vec{K} = \frac{2\pi}{\Lambda} = 2\pi \frac{2n\, sin[(\alpha_2 - \alpha_1)/2]}{\lambda} \tag{1-1}$$

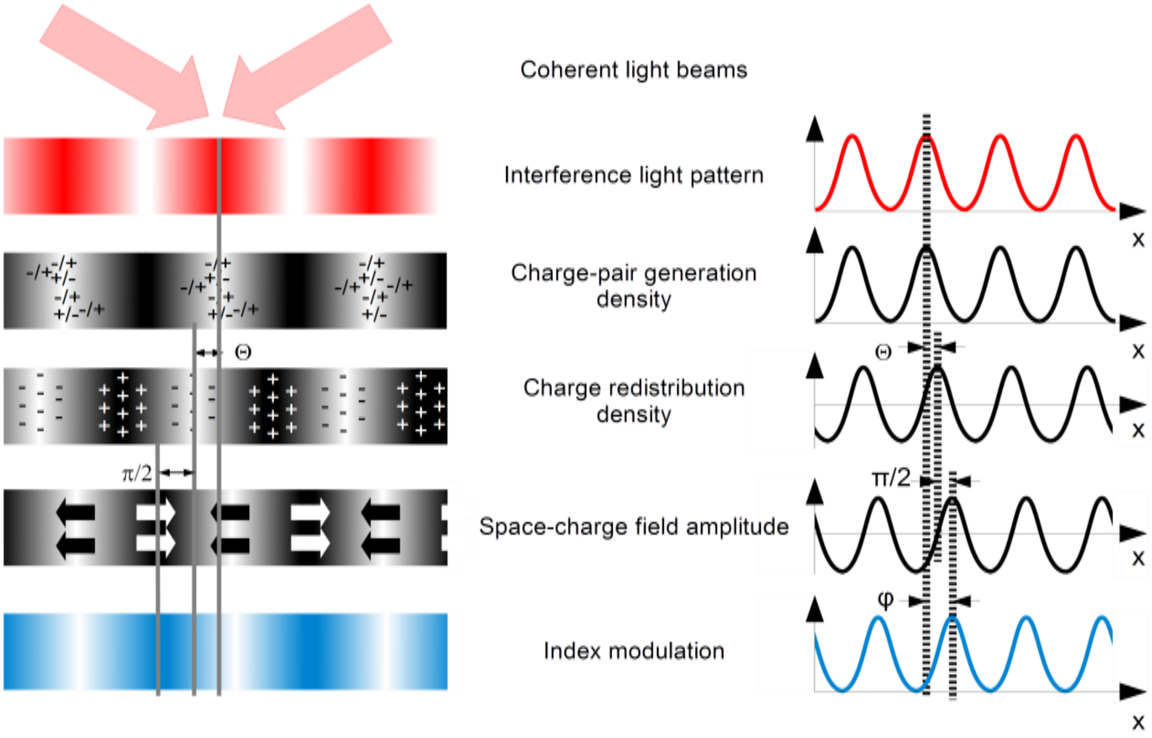

Figure 1-1: Illustration of the formation of refractive index gratings within photorefractive material.

producing a vector oriented orthogonally to the fringe plane and inversely related to the fringe period (λ). When a photorefractive polymer film is placed in the region of interference, excitons, or electron-hole pairs bound through Coulomb forces are generated in the regions of high intensity, as illustrated in Figure 1-1. These excitons can undergo geminate recombination or can dissociate into a positive and negative charge. The majority carrier in a system is the entity with the highest mobility within the polymer transport matrix, and in the case of most charge transporting polymers used in photorefractive systems, holes are the most mobile. These holes begin to migrate away from the regions of high intensity through diffusion and drift transport mechanisms. In polymeric media, diffusion is generally minimal due to the energetic disorder of these systems, so an external electric field of magnitude 10-80 V/μm is applied across the bulk to facilitate drift of the mobile charges. The mobility of drift driven charges is field dependent, so higher applied fields result in larger mobilities, leading to faster and larger material response.[15]

Since the holes will travel along the direction of the applied electric field, care must be taken in configuring the hologram recording system. For the majority of photorefractive polymer applications, the transparent electrodes used to apply the electric field will cover the entire active area of the device, resulting in an electric field oriented orthogonally to the sample face. When recording a hologram in a reflection grating configuration (Figure 1-2a), the two interfering beams approach the sample from opposite sides, counter-propagating to create fringes aligned with the sample plane and maximizing the projection of the corresponding grating vector onto the applied electric field. In this case, the excited holes are drawn out of one fringe and travel along the applied electric field perpendicular to the fringes and into the dark region of the fringe, taking the shortest possible path from bright to dark fringe. Alternatively, a transmission grating is formed by two beams which are incident from the same side of the sample, and in a case where they approach symmetrically with respect to the surface normal (Figure 1-2b), the grating vector is orthogonal to the applied electric field vector. As the electric field is aligned with the fringes, holes move along the fringe without traveling into and being trapped in the dark region, preventing the development of the desired index modulation. To make this transmission configuration viable, the sample plane must be tilted with respect to the grating vector, allowing some projection of the grating vector onto the applied electric field vector and transporting holes across fringes into the regions of lower intensity (Figure 1-2c).

Spatial modulation of the positive and negative charges resulting from this transport leads to the creation of a spatially modulated electric field known as the space-charge field. The magnitude of the space-charge field generally ranges from 1 % to 10 % of the applied electric

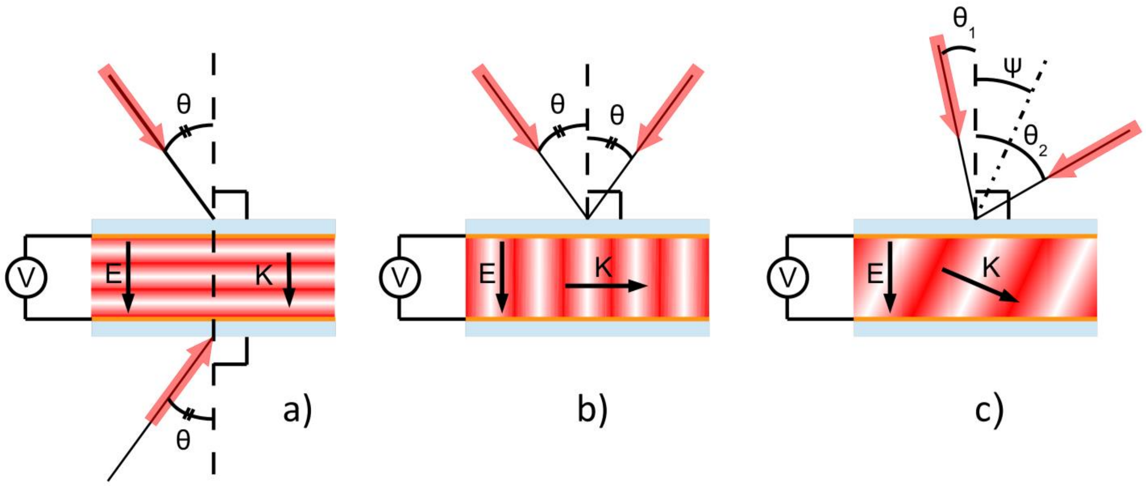

Figure 1-2: Holographic recording geometries in which a) illustrates a reflection grating configuration in which the writing and reference beams are symmetric with respect to the sample normal. Transmission geometries with b) symmetric writing and reference beams and c) asymmetric writing and reference beams.

field. Mimicking the intensity oscillation of the writing beams, the space-charge field profile is shifted relative to the charge profile due to the gradient relation between charge density and the electric field. Transport properties of the polymer matrix additionally affect the magnitude of the shift of the charge structure with respect to the fringes with diffusion driven systems exhibiting a quarter fringe shift and drift resulting in shifts less than a quarter of a fringe $(\pi/2)$.[16]

One of the substituents in the photorefractive polymer system is a collection of small polar molecules, often chromophores, which orient along the externally applied electric field prior to illumination. The orientational mobility necessary for this poling is afforded by the addition of another small molecule to the system called a plasticizer, which reduces the glass transition temperature of the polymeric compound by disrupting the long-range order of the polymer.[17] At the glass transition temperature (T_g), the polymer host is flexible and the molecules are free to rotate and orient towards the poling field. By reducing the T_g to the temperature at which the gratings will be recorded, the poling response of the system is increased. This poling of the homogeneous polymer composite breaks the centrosymmetry of the system and enables an optical response that is linearly dependent on the magnitude of the applied electric field and the first hyperpolarizability of the chromophore. This response is called the linear electro-optic effect or Pockels effect, inducing a birefringence, or polarization and propagation direction dependent index of refraction, within the film. In response to the superposition of the locally oscillating space-charge field and the external electric field, this effect leads to a locally oscillating birefringence, effectively recording the illumination pattern as a refractive index grating.[16] Additionally, the orientation of the molecules themselves in the direction of the space-charge field adds to the grating response and has been termed orientational enhancement. The orientational enhancement effect is quadratically related to the applied and space-charge fields and increases the diffraction efficiency of the grating by an order of magnitude over that of a purely linear electro-optic based grating.[17]

Just as the index of refraction is spatially modulated in response to an interference pattern, it can be homogenized through illumination by a plane wave, or structureless beam as the ability to erase and rewrite the grating is one of the primary benefits to using of photorefractive polymers as holographic recording media. This uniform beam excites the charges as before but instead of being trapped in the dark regions, they are able to migrate through the film to equilibrate the charge density. At this time, the film has been returned to its original state, and a new hologram can be recorded.

1.3 Photorefractive Dynamics

Physical descriptions of the processes contributing to the buildup and decay of the space-charge field in photorefractive polymer devices have been a topic of research for the past few decades. This advancement leads toward an understanding of the interrelation between the photorefractive response of the device and the properties of the polymer matrix. The basis for these models is work in photorefractive crystal dynamics performed in the late 1970's by Moharam and Young[18] and Kukhtarev et al.[19] In these models, dynamic formation of the space-charge gratings was analyzed based on a transport band model common to crystalline semiconductor materials, presenting a conduction and valence band with a series of donor and acceptor impurities acting as shallow trapping sites. This system allowed calculations of the resulting index of refraction within the crystal, as well as its erasure, to be performed with the photorefractive index response based solely on the linear electro-optic effect. While these models sufficiently describe grating buildup and decay within a crystalline environment, a model for polymeric systems must take into account effects such as the field dependence of the quantum efficiency and carrier mobilities (with mobility dependent parameters such as recombination and trapping rates) as well as the orientational effect that the chromophores have on the final refractive index modulation.

Schildkraut and Buettner took these field-dependent effects into account in their model of the space-charge build-up in photorefractive polymers. Their hole transport analysis takes into account the mobility dependence of the recombination rates as per Langevin theory and includes the effect of deep hole traps within the system in addition to that of the shallow trapping sites. A deep hole trap is one that is subject to thermal detrapping, but at a rate that is on the order of 10^{-4} per second in comparison to the shallow detrapping rate on the order of 1 per second.[20] Subsequent work by Schildkraut and Cui delved into elucidating an analytical relationship between photoconductive properties and grating formation using the deep trap model in a steady state environment.[21] Further work published by Ostroverkhova and Singer in 2002 extended this model to apply to a dynamic system and included a shallow trap level in the analysis.[22] This shallow trap has a detrapping rate on the order of 0.1-1 $\sec^{-1}$ and was included to account for experimental indications of dispersive charge transport within the highly disordered media as, well as the sub-linear intensity dependence of the holographic response. Oh, Li and Kim added a trap density dependence to the hole mobility in Ostroverkhova's model in 2008, bringing the model closer to agreement with experimental results and enabling more detailed understanding of the effect that trap density plays on formation of the space-charge field.[23] The subsequent analysis will follow from Ostroverkhova's modification of Schildkraut and Buettner's work on space-charge dynamics and will clarify the derivation of relationships between material parameters and the photorefractive response.

The main assumptions made in the derivation of this model are taken from those commonly used in polymeric photoconducting media models and analysis. It is assumed that the photorefractive polymer composite is initially electronically neutral with electron-accepting type sensitizers distributed throughout the volume with density N_A. When optically excited by incident light of intensity I for sensitizing species with photogeneration cross-section s, an electron is transferred from the surrounding matrix to the sensitizer and the hole is free to move within the hole only transporting polymer matrix with free hole density ρ. The holes hop between the HOMO (highest occupied molecular orbital) levels within the media through drift and diffusion mechanisms. The hole may be trapped by another molecular species (of density M_{T1} for shallow traps and M_{T2} for deep traps) within the compound at rate γ_T from which it can be thermally detrapped (at the rate β_1 for shallow traps and β_2 for deep traps). M_1 and M_2 are the density of filled shallow and deep traps, respectively. Additionally, the hole can recombine with an anionic sensitizer (density N_A^i) at rate γ requiring photoexcitation to detrap. The dynamics of this system are illustrated in Figure 1-3 and are related through the following system of nonlinear equations:

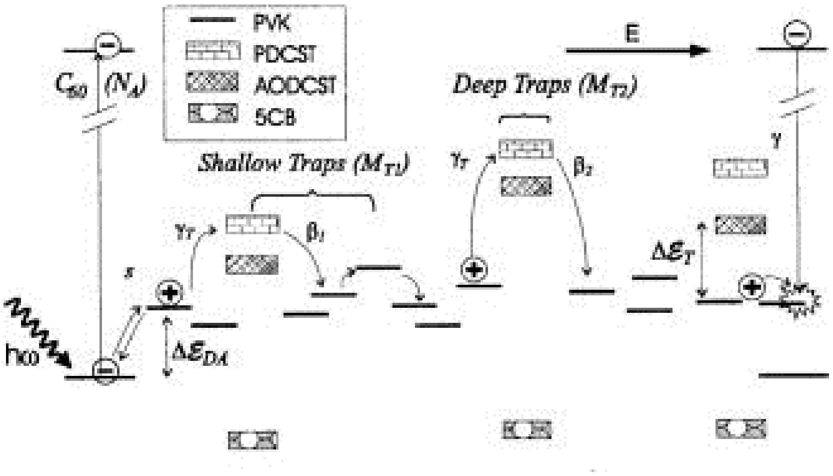

Figure 1-3: Schematic representation of Ostroverkhova and Singer's modified Schildkraut model for photorefractive dynamics. Also illustrated are the relative energies of the chromophores PDCST, AODCST and 5CB to PVK. Reproduced from [22], with permission from AIP Publishing LLC.

$$\frac{\partial \rho}{\partial t} = \frac{\partial N_A^i}{\partial t} - \frac{\partial M_1}{\partial t} - \frac{\partial M_2}{\partial t} - \frac{1}{e}\frac{\partial J}{\partial x} \tag{1-2}$$

$$\frac{\partial M_1}{\partial t} = \gamma_T(M_{T1} - M_1)\rho - \beta_1 M_1 \tag{1-3}$$

$$\frac{\partial M_2}{\partial t} = \gamma_T(M_{T2} - M_2)\rho - \beta_2 M_2 \tag{1-4}$$

$$\frac{\partial N_A^i}{\partial t} = sI\left(N_A - N_A^i\right) - \gamma N_A^i \rho \tag{1-5}$$

$$\frac{\partial E}{\partial x} = \frac{e}{\epsilon_0 \epsilon}\left(\rho + M_1 + M_2 - N_A^i\right) \tag{1-6}$$

$$J = e\mu\rho E - e\mu\xi\frac{\partial \rho}{\partial x} \tag{1-7}$$

(1-2) details the dynamics of the free holes within the system and is dependent on the ionization and trapping rates as well as the spatial variation of the photocurrent density. The first part of (1-3) and (1-4) relate the rate of change of filled shallow and deep trap densities to the trapping rate, the density of holes that can be trapped and the number of available traps. The second part includes the liberation of holes from the traps at the respective detrapping rate. (1-5) similarly describes the rate of change of ionized acceptors with ionization and recombination rates and the total number of ionized and un-ionized acceptors. The spatial variation of the electric field (E)

across the volume is defined by (1-6) and relates to the free charge and combined trap densities as well as the anionic sensitizer molecule density. The final equation (1-7) in the system describes the photocurrent (J) in the system as the sum of the drift (the first term) and diffusion (second term) contributions. The diffusion coefficient (ξ) is given by $\xi = k_B T/e$ where e is the elementary charge, k_B is Boltzmann's constant and T is the temperature of the system. The dielectric constant and the permittivity of free space are ϵ and ϵ_0 respectively.

The photogeneration cross-section (s) is a parameter that incorporates the photogeneration efficiency (φ), the absorption coefficient of the material (α) the illumination energy ($\hbar\omega$) and N_A^i through $s = \alpha\varphi/\hbar\omega N_A^i$. As the photogeneration efficiency is electric field dependent, so is the photogeneration cross-section. The hole mobility (μ) is another field dependent term since an applied electric field effectively decreases the energetic difference between transport sites, with a higher electric field further decreasing the barrier to hopping and increasing the apparent mobility. Mobility additionally depends on the temperature of the system and, according to Oh, Li and Kim[24], the initial trap density. The effects of dispersive transport can also be taken into account here, adding path length dependence to the mobility, but we will use an average mobility in this case in order to facilitate the derivations of mobility relations to the photorefractive process. Detrapping rates for shallow and deep traps (β_1 and β_2) are assumed to be constant with electric field as the magnitude of the effect of the applied electric field with respect to the trap depth is negligible. The trapping rate (γ_T), on the other hand depends on the mobility of the holes, as higher mobility leads to more trapping encounters over the same period of time, and its electric field and temperature dependences follow that of the mobility. Finally, the recombination rate (γ) is described by Langevin theory regarding geminate recombination and leads to the relation $\gamma = e\mu/\epsilon\epsilon_0$, but as this relation is dependent on the mobility of charge carriers, this parameter follows the same trend as the mobility.[22]

In taking the DC and first-order Fourier decomposition terms of this system, the steady state and main frequency response can be analyzed separately by making the assumption that the material interaction can be decomposed into a response due to the average intensity applied to the media (spatially invariant responses are indicated by the subscript 0) and a response due to the sinusoidal pattern of the interference, which takes the form $I(x) = I_0 + I_1 \cos(Kx)$. Experimental data has validated this kind of analysis for a variety of photorefractive polymer cases.[22] The steady-state Fourier components describe the dynamics of free charge generation, transport and trapping and relate these dynamic processes to the physically measureable parameter, current density. The first order Fourier terms relate the parameters found through the steady state analysis to the properties and dynamics of the space-charge field development. This approach allows the speed of the diffractive response to be related to material parameters inherent to the material and a comparison to be made among various compositions.

One of these comparisons is the contribution to the performance by deep and shallow traps. In photorefractive polymer systems, deep traps arise when the HOMO level of the chromophore lies above that of the transport molecule at which point the chromophores begin to take part in the transport of the holes. The shallow traps are considered to be from impurities, defects and orientational effects within the transport molecule itself.[23, 25, 26] Ostroverkhova and Singer compared the dynamics of plasticized PVK (polyvinylcarbazole) compounds with two different chromophores, AODCST (2-[4-bis(2-methoxyethyl)amino] benzylidene]-malononitrile]) and 5CB (4′-(n-pentyl)-4-cyanobiphenyl), the energetics of which are illustrated in Figure 1-3. The HOMO level of the AODCST chromophore lies above that of the PVK, indicating that it would play a role in the transport and trapping of the holes while 5CB lies below that of PVK, creating a system with no appreciable deep trap density. The AODCST systems exhibited a faster initial rise than 5CB in the grating formation but took longer to reach steady-state diffraction. The fast time response performance enhancement of AODCST over 5CB was attributed to the additional AODCST states available within the transport manifold while the longer settling time was attributed to the proliferation of deep traps within the material. While the system with deep traps is slower in overall response time, the diffraction efficiency reaches a higher steady-state value, a phenomena attributed to the number density of deep traps themselves. Their conclusion was that the fastest chromophore system would be one in which the energy level of the chromophore was similar to that of the transport molecule to lend itself to transport while having a narrow enough density of states such that the number of deep traps is minimized.[22]

Though this type of rate equation analysis is a robust method by which the build-up dynamics and relative dependences can be thoroughly studied, some of the primary associations to photorefractive responses can be gleaned from these relations if linearized by simplifying to particular cases such as those discussed by West and Binks.[15] One such case is that in which there is no appreciable deep trap density, such as TPD (tetraphenyldiaminobiphenyl):DCST varieties. Making the additional assumptions that holes have relatively short lifetimes prior to recombination and that there are more shallow traps in the system than free charges, (1-2)-(1-7) yield the exponential time evolution of the free charge density under the assumption of constant filled trap density ($M = M_{10} + N_{A0}^{i}$)

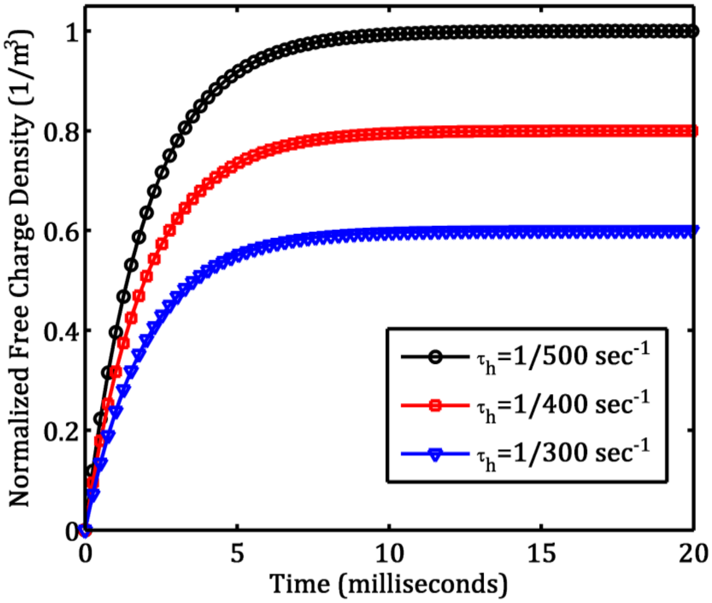

Figure 1-4: Normalized free hole density dynamics for three different values of hole recombination lifetimes. All other parameters are assumed constant.

$$\rho_0(t) = sI_0(N_A - M)\tau_h \left[1 - e^{-t/\tau_h}\right] \tag{1-8}$$

where τ_h is the hole recombination lifetime, $1/\gamma M_{10}$. Figure 1-4 illustrates the rate of growth and steady state density dependence on the hole recombination lifetime. When holding all other parameters constant, the higher the recombination rate, the faster the free hole density increases to reach a larger steady state value.[15]

By convention, three parameters of the electric field formed by the spatially varying illumination can be defined as the diffusion field (E_D), or the field strength equal to the mean thermal energy across one radian of the period; the saturation field (E_q), or the maximum electric field that can be sustained as a result of the fringe pattern (of grating vector K); and the mobility field (E_M), or the field necessary for a hole to drift one radian of the period within its recombination lifetime:

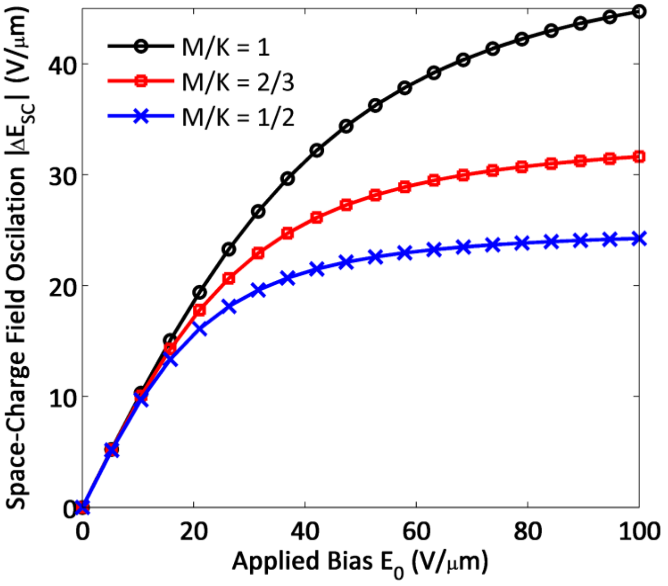

Figure 1-5: Magnitude of the space-charge field modulation as a function of applied electric field for normalized trap density to spatial frequency ratios of 1 (circles), 2/3 (squares) and ½ (triangles). A saturation field parameter of 50 V/μm was assumed and the diffusion contribution was neglected.

$$E_D = \frac{k_B T}{e} K \tag{1-9}$$

$$E_q = \frac{eM}{\epsilon K}\left(1 - \frac{M}{N_A}\right) \tag{1-10}$$

$$E_M = {}^{\gamma M}\!/_{\mu K} \tag{1-11}$$

Through the solution of the simplified case of the dynamic equations and making the additional generally valid assumption that $E_D \ll E_0, E_q$ the steady-state amplitude of the space-charge field is given by

$$|E_{SC}| \approx \left|\frac{-E_q E_0}{(E_q + iE_0)} \frac{I_1}{I_0}\right| \tag{1-12}$$

in which I_0 is the constant, DC part of the incident intensity pattern and I_1 is the intensity of the modulation following $I(x) = I_0 + I_1 \cos\,(Kx)$. Under the assumption that the grating buildup is not trap density limited, the space-charge field magnitude is limited to the projection of the poling field (E_0) onto the grating vector ($E_{SC} \leq E_0 \cos\varphi$). The characteristic time to reach the steady-state response is

$$Re(\tau_{rise}) = Re\left(\frac{\epsilon}{\rho_0 e\mu}\frac{E_q(E_M + iE_0)}{E_M\left(E_q + iE_0\right)}\right) \tag{1-13}$$

and the phase shift (Φ) between the incident optical pattern and resulting space charge field

$$\Phi = tan^{-1}\left(\frac{-E_0}{E_q}\right) \tag{1-14}$$

One of the readily apparent conclusions that can be made from these equations is that the magnitude of the space-charge field oscillation is dependent on the ratio of the trap density to the spatial frequency of the fringes within the media as shown in Figure 1-5 with respect to a normalized M/K value. This indicates that to obtain large space-charge fields in a high-resolution environment (large $\vec{K}$), there must also be a high density of traps available. The phase shift is also dependent on the trap density, with the magnitude of this shift playing a large part in the phenomena of photorefractive gain. Alternatively, the trap density (assuming the absence of deep traps within the media) has no bearing on the speed of the response in this type of composite. The magnitude of the space charge field additionally has the term I_1/I_0 which describes the contrast of the fringe pattern. Higher fringe contrast, therefore, leads to larger space charge fields.[15]

As mentioned in the previous section, E_{SC} and E_0 are linearly superimposed to form the resulting field $\overrightarrow{E_{res}} = \overrightarrow{E_0} + \overrightarrow{E_{SC}}\cos(Kx + \Phi)$ as shown in Figure 1-6. The angle between the space-charge field vector and the applied electric field can be found through

$$cos\,\alpha = \frac{E_0 + E_{SC}\,cos\,\varphi\,cos(Kx + \Phi)}{E_{res}} \tag{1-15}$$

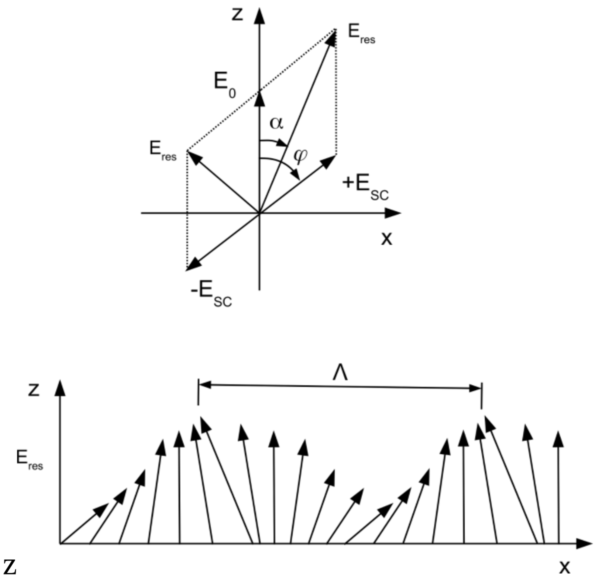

Figure 1-6: The resulting electric field (E_{res}) due to the space charge field (E_{SC}) and the applied electric field (E_0) and an illustration of the spatial dependence of E_{res}.

in which φ is the angle between the grating vector and the applied electric field. These parameters can be related to the spatially oscillating change in refractive index that the media undergoes in the case of a *p*-polarized probe beam, Δn_p, where the *p*-polarization is in the plane of the applied electric field and the space-charge field, through

$$\Delta n_{p,p}(x) \propto E_{res}^2 \left[cos^2(\alpha - \beta) + \frac{\Delta n_0}{n_e - n_0} \right] \tag{1-16}$$

where β is the degree from perpendicularity of the probe beam propagation with respect to the external electric field and $\frac{\Delta n_0}{n_e - n_0}$ is a material parameter. For most orientational enhancement based materials with near room temperature T_g, $\Delta n_0 \approx \frac{1}{3}(n_e - n_0)$. In the case of an *s*-polarized probe beam, the polarization is always perpendicular to the direction of the poling field and the equation simplifies to

$$\Delta n_{p,s}(x) \propto E_{res}^2 \left[\frac{\Delta n_0}{n_e - n_0} \right] \approx \frac{1}{3} E_{res}^2 \tag{1-17}$$

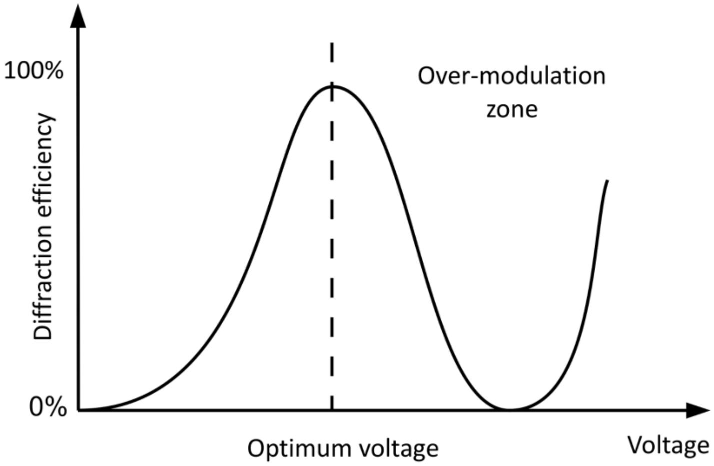

Figure 1-7: Illustration of the diffraction efficiency measured in a four-wave mixing experiment as a function of applied field.

Diffraction efficiency is a physical parameter that can be externally measured and relates to the change in refractive index through a distance, L, assuming a thick volume hologram as per Kogelnik[2] through

$$\eta = sin^2\left(\frac{\pi \Delta n L}{\lambda \cos \theta_{in}}\right) \tag{1-18}$$

where θ_{in} is the angle of the probe beam with respect to the sample normal. The Δn dependence translates to an E_{res} dependence with the associated trap density and applied electric field effects. Additionally, the sinusoidal dependence on the electric field, illustrated in Figure 1-7, leads to a corresponding diffraction efficiency overmodulation, or peak diffraction efficiency at a specific electric field followed by a decrease in response with increasing field. In the case mentioned here, the orientational enhancement effect is included in the $\frac{\Delta n_0}{n_e - n_0}$ term, and will be discussed in further detail in a later section, as will the E^2 dependence of the refractive index modulation.

1.4 Components and Physical Implications

Recent interest in organic photovoltaic (OPV) technology has led to an increased effort in understanding the physics of photogeneration and conduction in organic semiconductors. PR polymers and photovoltaic materials are similar in basic behavior, as each one depends on the generation and transport of photoexcited charges within an organic matrix, allowing significant gains in understanding to be made in PR polymers following those in OPVs.

Multiple types of organic and organic-hybrid materials exist that exhibit photorefractive properties such as amorphous glass composites and polymer dispersed liquid crystal blends, but this review will focus solely on organic photorefractive polymers. This polymer composite family comprises two basic configurations; the guest-host polymer composite and the fully functionalized polymer composite. A guest-host composite is a polymer matrix in which small molecules have been dispersed, each performing a distinct function necessary for photorefraction within the bulk. This provides for simple experimentation with new or different ratios of constituents as well as expanding the range of materials that can be incorporated but does have to deal with potential phase separation of the constituents. The fully functionalized system combines a number of functionalities onto a single polymer backbone, reducing the number of distinct entities within the media. This results in a more phase stable system but at the cost of increased synthetic complexity. Some of the higher performing composites are a combination of the two types, with partially functionalized backbones leading to increased phase stability while retaining the majority of the simplicity of the guest-host synthetic scheme. The individual molecules providing the various functionalities are discussed in the following sections.

1.4.1 Sensitizers

The sensitivity of PR polymers is determined by the material's ability to convert incident radiation into a refractive index modulation, with the generation of mobile charges in response to photoexcitation as the first step in this process. The efficiency with which incident photons are converted into charge carriers, or the photogeneration efficiency (φ), is therefore a fundamental parameter within the grating formation dynamics. Increasing this efficiency can translate into an increase in the overall PR sensitivity and performance, but standard conductive polymers used in PR composites generally have absorption bands located in the ultraviolet region of the spectrum, limiting their usefulness for visible and infrared holographic applications. By doping these polymers with entities exhibiting high molar absorptivity at the desired wavelengths, the photorefractive response can be significantly improved.

Organic dyes are the most common family of sensitizers implemented in photorefractive devices due to the available diversity of molecular structures and relative ease of design and synthesis. They pose less risk to the environment than noble metal based sensitization complexes, and the solubility can be adjusted to improve bulk homogeneity within the polymer matrix.[27] The most common sensitizers used in photorefractive polymer systems are fullerenes and trinitrofluorenones, but a host of other molecules such as graphene and semiconducting nanoparticles have been implemented and characterized.[28–33] General photogeneration efficiencies of photorefractive devices are around a few percent and take into account not only the quantum efficiency of the molecule but also its ability to translate that charge into a free carrier.[34]

A photon can excite an electronic transition within a molecule if the energy of the photon ($E_{photon} = hc/\lambda$) corresponds to that of an allowed transition. This excitation takes the form of

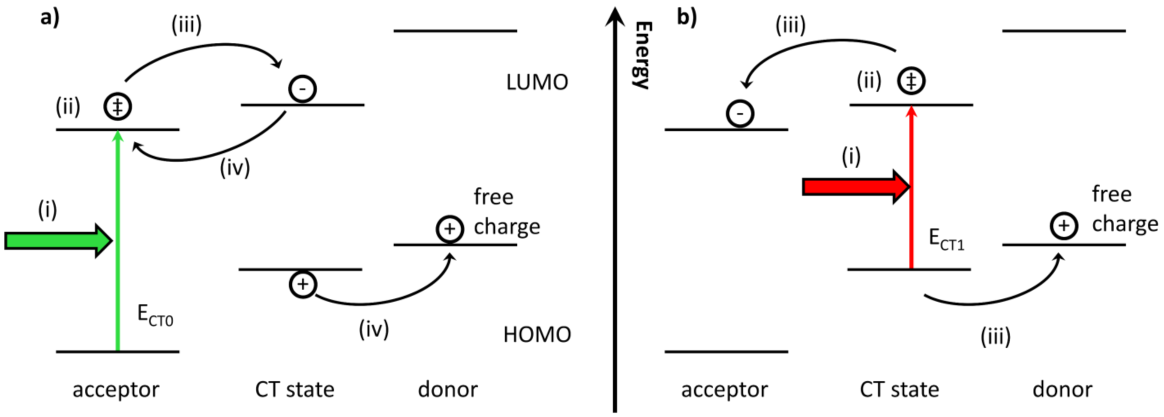

Figure 1-8: Illustration of charge generation concepts in organic systems. a) The $CT_0 \rightarrow CT_1$ mechanism of charge generation begins with absorption of a photon (i) with energy corresponding to the CT_0 state of the acceptor, creating an exciton (ii). This exciton can diffuse to the charge transfer (*CT*) state (iii) at which time it can dissociate into free charges (iv) if the energy of the *CT* state is smaller than that of the acceptor energy. b) Alternatively, the *CT* state can be excited directly by a photon of the appropriate energy (i) creating an exciton (ii) followed by charge separation (iii).

a pair of opposite charges separated by a distance related to the excited state orbital, defining the thermalization or Coulomb radius. The coulombic potential between the pair is inversely related to the thermalization radius and defines the energy that must be put into the system to dissociate them and produce a mobile charge.

Dissociation of the ionic pair can occur if the thermal energy is high enough to overcome the coulombic forces or if an external field is applied to overcome the electric potential binding the two charges.[15] Upon dissociation, the hole can migrate through the polymeric media while the electron remains bound to the sensitizer species forming an anion. In 1934, Onsager developed a model describing the effects of an external electric field on the dissociation and recombination of a solution of weak electrolytes derived from the Smoluchowski equation relating to drift and diffusion.[35, 36] His addition to the prevailing electrolyte conduction theory was the implementation of a relation between the thermalization radius and the externally applied electric field with respect to the effect on the measured current. The problem with this theory was that the experimentally determined thermalization radius of a standard sensitizer within an organic matrix is a few tenths of nanometers as opposed to the few nanometers as predicted by Onsager.[37–39] Braun made a conceptual adjustment in the 1980's in which he extended the thermalization radius to include not only the generation of the exciton from the ground state, labeled CT_0 , but also the further dissociation of the exciton across the charge-transfer state as introduced by Lyons in the late 1950's.[40] The charge–transfer complex consists of the extended orbital between the charge accepting sensitizer and the donor molecule from which the charge is transferred, and is termed the first excited state of the charge-transfer complex, or CT_1 as illustrated in Figure 1-8.[41] The thermalization radius of this complex corresponds to the original scale of the Onsager model, allowing its extension to organic semiconducting media such as photorefractive polymer systems. Experiments have shown that as opposed to the $CT_0 \rightarrow CT_1$ mechanism, the CT_1 state can be directly excited in a subset of photorefractive materials as indicated by an absorption band that does not correspond to either of the base constituents. This makes possible the application of high energy gap compounds such as PVK and trinitrofluorenones in the visible and near infrared regime, wavelengths at which the pure molecules do not absorb.[42–44]

Model

The coulombic energy between the pair in the CT_1 state (ΔE_C) is given by the equation for the Coulomb potential, taking into account the increased thermalization radius for the CT_1 state (a)

$$\Delta E_C \approx \frac{e^2}{4\pi\epsilon\epsilon_0 a} \tag{1-19}$$

where e is the elemental charge, ϵ is the dielectric constant of the polymer media (generally on the order of 3-4.5 [22]) and ϵ_0 is the dielectric permittivity of free space. The charge transfer kinetics of the system are described through the field dependent dissociation rate ($k_d(E)$), the bimolecular rate of hole-electron recombination (k_r), and the rate at which the excited carriers decay into the ground state (k_f), a rate which is not dependent on the applied electric field. The lifetime of the excitation (τ) has been experimentally determined to lie within the nanosecond regime and is given by

$$\tau(E) = \frac{1}{k_f + k_d(E)} \tag{1-20}$$

and the probability with which the pair will dissociate to form mobile carriers ($P(E)$) is

$$P(E) = k_d(E)\tau(E) = \frac{k_d(E)}{k_f + k_d(E)}. \tag{1-21}$$

Using the equilibrium constant for the ion pair developed by Fuoss,[45] the equilibrium constant in the no field limit is

$$K(0) = \frac{3}{4\pi a^3} e^{\frac{-\Delta E_C}{kT}} \tag{1-22}$$

Onsager's addition of the field dependent reduction of the ionization energy modifies the equilibrium constant to the following form, which is simplified through the Taylor expansion of the Bessel function of the first kind, J_1.

$$K(E) = K(0) \frac{J_1\left[2\sqrt{2}\left(-b(E)\right)^{\frac{1}{2}}\right]}{\sqrt{2}\left(-b(E)\right)^{\frac{1}{2}}} \approx K(0)\left\{1 + b(E) + \frac{1}{3}b(E)^2 + \cdots\right\} \tag{1-23}$$

$$b(E) = \frac{e^3 E}{8\pi\epsilon\epsilon_0 k^2 T^2}$$

This leads to the realization that even though $k_d(E)$ and $K(0)$ are expected to be highly dependent on the thermalization radius, the relative increase of the dissociation rate constant is independent of this radius. Assuming a Langevin form for the recombination rate of the geminate pairs, the bimolecular rate of hole-electron recombination takes the form

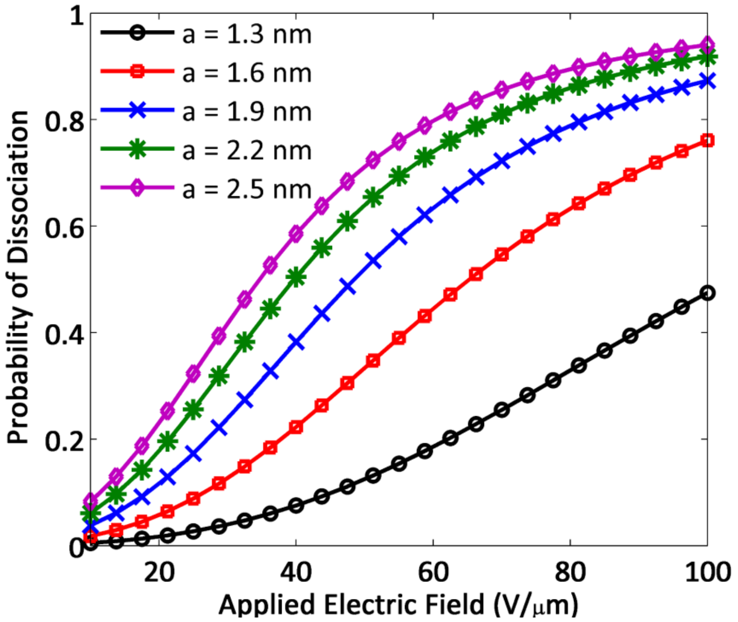

Figure 1-9: Probability of dissociation as a function of applied bias for thermalization radii from 1.3 nm to 2.5 nm.

$$k_r = \frac{\langle \mu \rangle e}{\epsilon \epsilon_0} \tag{1-24}$$

where $\langle \mu \rangle$ is the spatially averaged mobility of both mobile species. The electric field dependent dissociation rate is therefore

$$k_d(E) = \frac{3\langle \mu \rangle e}{4\pi \epsilon \epsilon_0 a^3} e^{\frac{-\Delta E_C}{kT}} \left\{ 1 + b(E) + \frac{b(E)^2}{3} \ldots \right\} \tag{1-25}$$

and the according dissociation probability[41]

$$P(E) = \frac{\tau(E) 3\langle \mu \rangle e}{4\pi \epsilon \epsilon_0 a^3} e^{\frac{-\Delta E_C}{kT}} \left\{ 1 + b(E) + \frac{b(E)^2}{3} \ldots \right\} \tag{1-26}$$

The dissociation probability is related to the photogeneration efficiency through the additional term φ_0 describing the primary quantum yield, or the probability of forming the bound-pair state, with its relation to the charge thermalization and dependence on the applied electric field illustrated in Figure 1-9. The product of the two probabilities, $\varphi = \varphi_0 P(E)$, gives the total photogeneration efficiency of the system or the efficiency with which a photon absorbed by the media will successfully generate a mobile hole that contributes to charge transport.[46]

As the excitation energy for the majority of polymeric semiconductors that are used in photorefractive polymers are in the ultraviolet range (> 3 eV)[47], sensitizers must be added to the matrix in order to facilitate use in the visible and infrared excitation spectrum. The excitation gap for materials fitting this requirement is generally between 0.8 eV for the telecommunication wavelengths near 1550 nm through 2.25 eV, corresponding to operation in the center of the visible spectrum at 550 nm. Additional requirements regarding the energy levels with respect to the hole transporting polymers are that the LUMO (lowest unoccupied molecular orbital) and HOMO energies of the sensitizer lie below those of the polymer allowing the donation of an electron to and receipt of a hole from the sensitizer upon photoexcitation. Work performed by Hendrickx et al. interrogated a polystyrene matrix doped with various hole conducting arylimine derivatives exhibiting an array of ionization potentials.[42] Their findings illustrated that the larger the difference between the HOMO levels of the sensitizer and hole conductor, the more efficiently the complex is able to extract the charge carrier, increasing the dissociation efficiency. They also investigated the relation between the Braun CT thermalization radius and dissociation efficiency by adjusting the concentration of the arylimine within the matrix, effectively altering the size of the charge transfer complex. They experimentally verified the inverse relation between the thermalization radius and dissociation efficiency, finding that increased arylimine concentration was accompanied by increased dissociation efficiency. Koeber et al. performed a series of experiments on a TPD based polymer in the NIR investigating the effect of the ionization potential on the photoelectric and holographic properties, finding that the lower the

HOMO level of the sensitizer, the longer the charge carrier lifetime and the faster the holographic response.[29]

Sensitizers additionally play the role of the primary trap within the polymer matrix, as once they are reduced, a negatively charged anion is formed. This has been experimentally supported by the demonstration of correlation between anion and trap densities by Grunnet-Jepsen et al. using absorption spectroscopy in C_{60} sensitized PVK with dicyanostryrene chromophores.[48] Calculating the trap density via its relationship to the experimentally determined phase shift of the space-charge field through the saturation field, they found that the absorption spectra of the system indicated cationic C_{60} density directly corresponded to trap density.

In light of the need to maximize the efficiency with which incident photons can create a refractive index grating, one must also take into account that in order to use the grating in a diffractive manner, a probe beam must pass through the sample. This is evident from the definition of sensitivity[49]

$$S = \frac{\sqrt{\eta}}{I_{tot} L t} \tag{1-27}$$

relating the square root of the external diffraction efficiency (η) to the total writing intensity (I), medium thickness (L) and the exposure time (t). The external diffraction efficiency can be defined, excluding surface reflections, as[2]

$$\eta = \frac{I_{diff}}{I_{tot}} = \frac{I_{diff}}{I_{diff} + I_{trans} + I_{tot} e^{-\alpha L}} \tag{1-28}$$

where α is the absorption coefficient of the device at the wavelength of the probe beam. This illustrates the fact that the overall diffraction efficiency, and by association, the sensitivity of the photorefractive polymer, depends on transmitting as much of the probe beam as possible,

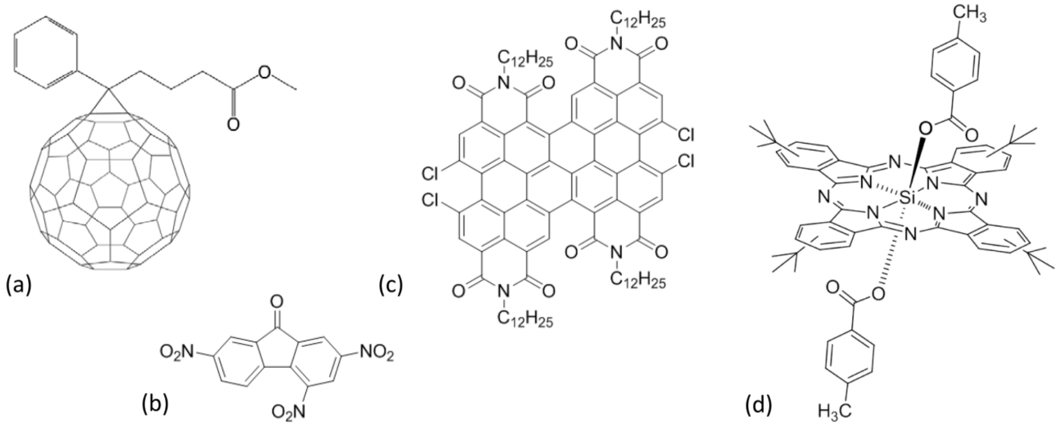

Figure 1-10: Sensitizers commonly used within photorefractive polymeric systems: a) C_{60} PCBM ([6,6]-phenyl-C61-butyric acid methyl ester), b) TNF (2,4,7-trinitrofluorenone), c) DiPBI (dimer perylene bisimide), (d) silicon phthalocyanine.

requiring a balance to be struck between efficient use of photons in grating recording and transmittance of the probe beam. For a system in which the reading wavelength is not the same as the writing wavelengths, there is more freedom in the optical parameters of the device but in order to satisfy these competing parameters in degenerate wavelength systems, values between 50 and 200 cm^{-1} are generally realized with doping levels around 0.1 to 2 wt%.[50]

Molecules

Three main absorption regimes of interest exist within photorefractive polymer applications: the 450-650 nm regime for display applications, the 700-1100 nm regime to take advantage of the transparency window of biological tissue, and the 1300-1550 nm range for telecommunications based applications.

The current workhorse sensitizer for photorefractive polymers in the visible regime is the fullerene C_{60} or its close relation [6,6]-phenyl-C61-butyric acid methyl ester (PCBM) which is a C_{60} molecule modified by a solubility enhancing ester, shown in Figure 1-10a. The first photorefractive polymer introduced by Ducharme et al. was an unsensitized system, exhibiting diffraction efficiency on the order of 10^{-5} and required minutes to reach steady state diffraction at 13 W/cm^2. [12] Shortly afterward, Silence et al. integrated C_{60} to contribute to photoexcitation of charge carriers and obtained not only a factor of ten increase in diffraction efficiency (10^{-4}), but also a response time shortened to 200 ms at an order of magnitude lower irradiance of 1.3 W/cm^2. [51] More recently, significant advances have been made by Eralp et al. in a PATPD (polyacrylic-TPD), 7-DCST (4-homopiperidino benzylidine-malonitrile), ECZ (ethyl carbazole), and C_{60} composite.[28] Their devices reached diffraction efficiencies of 85 %-95 % in 4 ms under an irradiance of 1.2 W/cm^2. Investigation of single pulse exposure of the same composition revealed 56 % internal diffraction efficiency after 2 ms upon irradiation by a single 1 ns pulse of fluence 4 mJ/cm^2. An electric field of 95 V/µm was applied for all measurements.

While the devices under study by Moon, Choi and Kim based on a similar TPD hole conducting polymer (poly-TPD, P-IP-DC (2-{3-[(E)-2-(piperidino)-1-ethenyl]-5,5-dimethyl-2-cyclohexenylidene}-malononitrile, BBP (benzyl butyl phthalate), PCBM) exhibited only 67 % diffraction efficiency, these results were achieved in 170 ms at an applied electric field of 30 V/µm and 60 mW/cm^2. [52] This external electric field is significantly lower than for other similarly performing devices, yet the gain remained high at 215 cm^{-1} when driven at 80 V/µm. Kober et al. extended the application of various fullerene based sensitizers in TPD film out to 830 nm for use in biological applications.[29] They used a TPD alternative PF6-TPD (poly-hexyl-triophene:N,N'-bis (4-methylphenyl)-N,N'-bis-(phenyl)-benzidine)) in a composite PF6-TPD: DMNPAA/MNPAA: ECZ:fullerene. The C_{84} based PCBM molecule exhibited near 100 % diffraction efficiencies and sub 100 ms response times at 640 mW/cm^2 irradiance.

TNF, or 2,4,7-trinitrofluorenone (Figure 1-10b) was one of the first sensitizers to exhibit a significant gain of 220 cm^{-1} at 90 V/µm and 100 % diffraction efficiency in the visible regime,

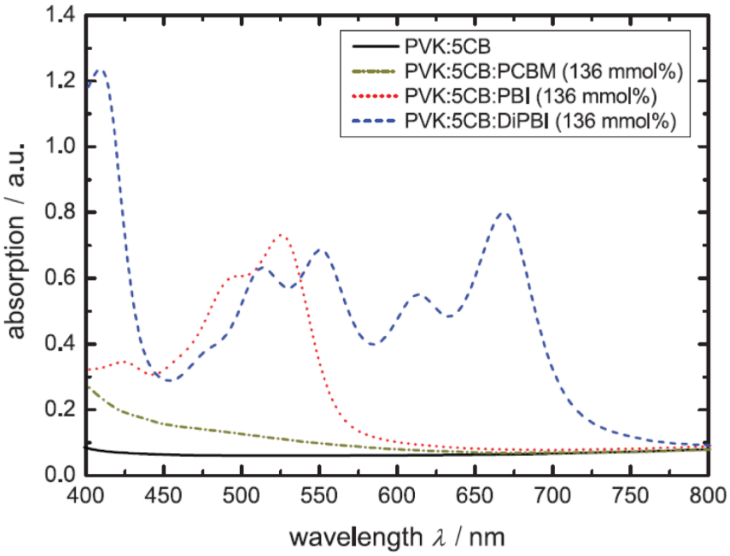

Figure 1-11: Absorption spectra of unsensitized sample (solid line) and samples sensitized with PCBM (green dot-dash), PBI (red dotted) and DiPBI (blue dashed). Reproduced from [53], with permission from WILEY-VCH.

but required 100 ms and a writing irradiance of 1 W/cm^2 to reach steady-state.[13] Since this time, work has been directed towards decreasing the response time and overmodulation field while maintaining the excellent performance parameters described by Meerholz et al. The best performing guest-host composite based on TNF was recently reported by Tsutsumi et al. in a device composed of PVK:7-DCST:CzEPA (carbazolylethylpropionate):TNF.[30] While the gain of this system was only 20 cm^{-1}, the diffraction efficiency peaked at 68 % at 45 V/µm with a fast response time of 24 ms at 1.5 W/cm^2. An additional characterization performed on these 100 µm thick samples was holographic image recording of real objects as well as computer generated ones.

Monolithic, multifunctional systems have improved as well, with Gallego-Gomez et al. reporting a polymer:DCDHF:ECZ:THF system exhibiting diffraction efficiency over 80 % at 65 V/µm (irradiance 360 mW/cm^2), gain of 350 cm^{-1} at 120 V/µm and fast response time of only 35 ms in these 37 µm thick samples.[31] Even though the glass transition temperature of this composite is far below room temperature, phase stability has been observed in excess of two years.

Ditte et al. have recently implemented perylene bisimide (PBI) and its dimer form (DiPBI), shown in Figure 1-10c, as novel sensitizing agents within a PVK:5CB based photorefractive polymer system.[53] Extensive use and characterization within the fields of organic light emitting diodes (OLEDs) and organic field effect transistors (OFETs) have shown PBI derivatives to be highly photostable and exhibit high electron affinities and charge carrier mobilities. Their additional strong absorption across the visible regime makes them an attractive species of study for inclusion as a photorefractive sensitizer (Figure 1-11). In their work, Ditte et al. observed a photoconductivity gain of 120 and 32 cm^{-1} respectively for PBI and DiPBI over PCBM at similar concentrations (~2.5 pS/cm and 1.5 pS/cm respectively vs. 0.021 pS/cm). The gain response of the 50 µm thick DiPBI sample was twice the magnitude of that of the PCBM at ¼ the loading (180 cm^{-1} vs. 90 cm^{-1} at an applied voltage of 70 V/µm) and PR speeds of 5.9 sec^{-1}, over 30 times faster than their PCBM doped system. No four wave mixing experiments were performed, leaving the feasibility of this material for holographic applications unclear but the performance to date indicates that this could be a viable system for analysis.

In order to extend the sensitivity out to 1064 nm, Grishina et al. doped PVK with graphene, a hexagonally symmetric monolayer of carbon atoms.[32] Graphene has been shown to have excellent chemical stability and charge carriers can travel a few microns within the highly conjugated sheet without scattering. Absorptivity measurements of the PVK:graphene system signify that the graphene absorbs uniformly across the visible and infrared regime and is a superposition of the two component absorbances, indicating that no significant charge-transfer complex is formed in this donor/acceptor system. This wide absorption band of graphene lends itself to use across various application ranges but in a system loaded at 0.15 wt% graphene to PVK, scattering due to the graphene sensitizers was found to hamper the photorefractive effect significantly, resulting in gain of only 7.1 cm^{-1} at an applied electric field of 133 V/µm and making the device as tested unviable. The quantum yield of thermalized electron-hole pairs for this system, however, is on the order of unity, indicating that this is indeed a sensitizer of interest and additional work may be warranted in reducing the scattering.

Another carbon based system exhibiting sensitivity in this regime is the carbon nanotube (CNT), which also has significant absorption across the visible and infrared range and has been investigated by a number of researchers. Vannikov et al. introduced carbon nanotubes into photorefractive polymers for use in the near-infrared (1064 nm) in a high glass transition temperature system composed of an aromatic polyimide (API) matrix doped with 0.25 wt% single walled CNTs (SWCNTs).[54] In these systems, there were no nonlinear optical chromophores and orientational enhancement was not a factor due to the high T_g so the photorefractive response was due entirely to the third-order electronic polarizability of the nanotubes. In these early systems, gain of 54 cm^{-1} and diffraction efficiency of 1.3 % was reported at an applied external electric field of 54 V/µm and time constants were in the range of 1 to 10 seconds.

Since this work, significant effort by a variety of researchers has been performed with Lingam, Kalghatgi and Winiarz recently grafting PVK to single and multi-walled CNTs in order to facilitate solubility with the room temperature T_g photoconducting matrix PVK:7-DCST:TCP (tritolylphosphate):CNT.[55] Absorption spectra of these grafted systems involving single and multi-walled CNTs indicate that grafting PVK to the CNTs does not create a charge transfer complex as expected but gain of 78.1 cm^{-1} at 80 V/µm and external diffraction efficiencies at 633

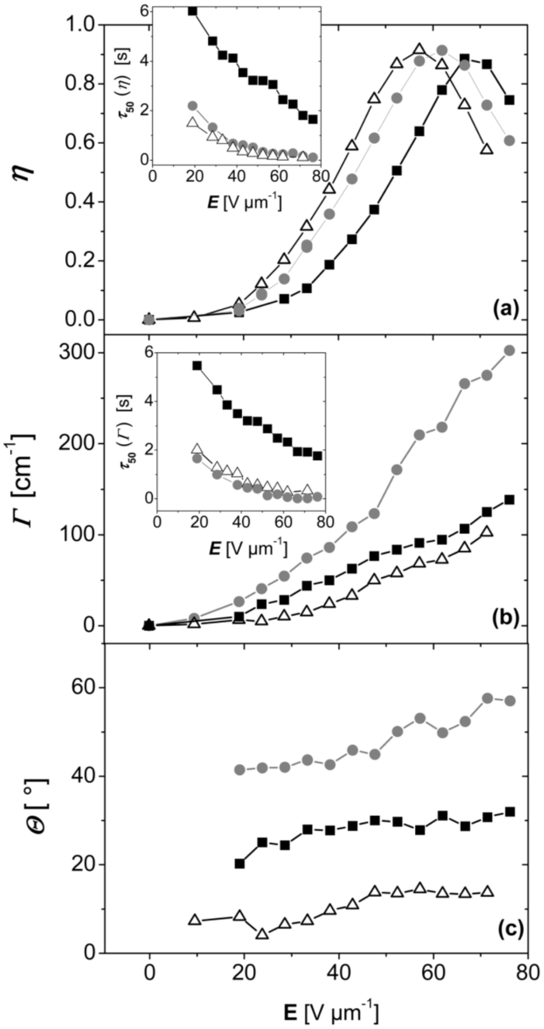

Figure 1-12: Photorefractive performance of composites sensitized with ZnPc (black squares), SiPc (grey circles) and C_{60} (open triangles). Reproduced from [57], with permission from American Chemical Society.

nm reaching almost 44 % at 50 V/µm (1.6 W/cm^2) in the 0.02 wt% MWCNT device shows an enhanced photorefractive performance. The charge generation quantum efficiency of this system was measured at 80 V/µm to be around 0.1 % with performance increasing with CNT loading until aggregation began to cause scattering within the media. No rates or time constants were given. More recently, Vannikov et al. studied the effect of adding a cyanine dye to their high T_g CNT sensitized system, investigating PVK:CNT:Dye blends finding a 14 fold increase in quantum efficiency through the addition of the dye, indicating that the cyanine was additionally contributing to photo-absorption and charge generation.[56] A maximum diffraction efficiency of 1.1 % is similar to that indicated in their 2005 publication but gains of 120 cm^{-1} at 100 V/µm and a characteristic response time of 0.4 seconds show significant improvement.

Phthalocyanines (Figure 1-10d) are a family of highly thermal- and photo-stable organic dyes that have been widely used in organic semiconductor research and have attracted interest over the last few years for use within photorefractive polymers. They exhibit broad absorption bands across the visible and near-infrared regions with HOMO and LUMO energy tunability based on the choice of the central atom and peripheral constituents. Molar extinction of these compounds is on the order of 10^5 $mol^{-1}cm^{-1}$ while that of the PCBM varieties lie in the 1000 to 2000 $mol^{-1}cm^{-1}$ range at 600 nm indicating that they absorb significantly more photons per molecule than PCBM alternatives. This high absorption as well as the tendency to aggregate at high concentrations limits the wt.% achievable in the polymer composite but Gallego-Gomez et al. were able to obtain sufficient transparency in a silicon phthalocyanine sensitized system with near half the concentration of the standard 0.5 wt% PCBM loading.[57] They found that these materials were stable under applied fields of up to 100 V/µm and remained phase stable for several months under standard storage conditions. In their room temperature T_g PVK:PDCST:BBP:Pc composites, 91 % diffraction efficiencies and gains of 350 cm^{-1} at 75 V/µm were reported and response times were as low as 100 ms at an irradiance of 320 mW/cm^2 (Figure 1-12).

Nanoparticles, or nanometer scale crystalline materials, have been gaining traction throughout organic semiconductor applications. Many of these are driven by the unique ability of semiconductor nanoparticles to exhibit tunable bandgaps through size control and

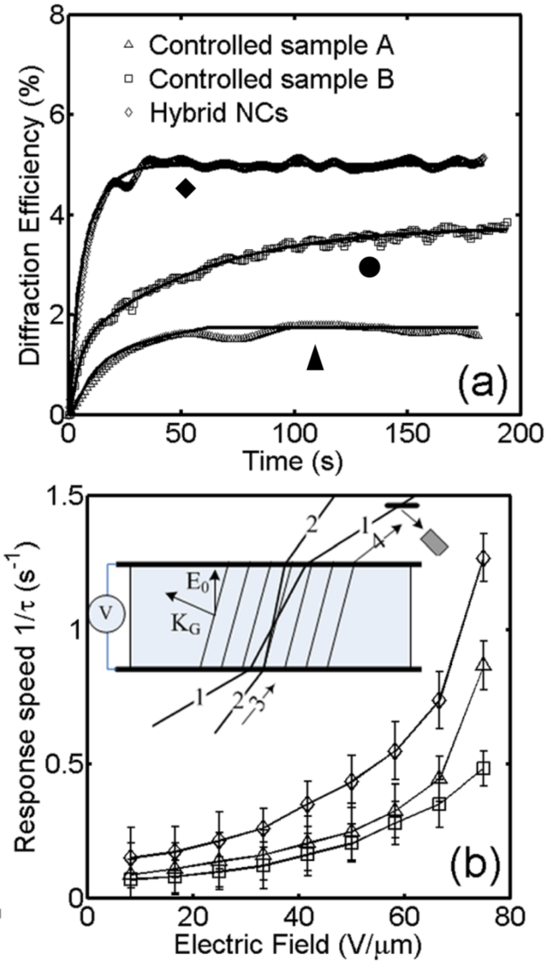

Figure 1-13: a) Diffraction efficiency dynamics of the Au:CdSe/CdTe blend, control sample A containing only Au NPs and control sample B containing only CdSe/CdTe NPs. Measurement performed at 66 V/μm. b) Photorefractive response speed as a function of applied electric field. Reproduced from [64], with permission from AIP Publishing LLC.

HOMO/LUMO level adjustment through the use of various inorganic semiconducting materials.[58] As sensitizers in photorefractive polymers, these materials are also interesting for their possible use as photogeneration media in the infrared, a range at which many other sensitizing materials have limited absorptivity and photogeneration efficiency.

A variety of nanoparticles have been implemented as sensitizers for use at visible excitation wavelengths with CdTe, CdSe, and CdS being the most prolifically studied. These materials generally show gains of less than 80 cm^{-1} and diffraction efficiencies peaking near

20 % to 30 %.[59–61] The performance barrier in many of these cases is the restriction placed on doping concentration due to aggregation by the nanoparticles which in turn affects their overall sensitization ability.[33] X. Li et al. recorded the photorefractive performance enhancement resulting from the implementation of Type II core/shell CdSe/CdTe nanoparticles compared to simple CdSe core-only particles in a PVK:DABM:ECZ:NP composite.[62] The gain and diffraction efficiency doubled through the addition of a shell layer and the response speed increased noticeably as well. The authors attribute these improvements to enriched free-carrier generation due to the shell layer energetics.

Zhu et al. examined the integration of lead sulfide (PbS) nanoparticles to impart sensitivity in the infrared regime as well as the effect that the ligand density had on photorefractive properties.[63] Ligands on nanoparticles are commonly used to functionalize the surface in order to increase solubility and deter aggregation, but ligands also act as a thin electrical barrier, decreasing the charge extraction efficiency. Zhu found that decreasing the surface coverage of a carbamate ligand on the nanoparticles increased the photocurrent by more than a factor of three and reached a quantum efficiency of more than 3 % at 100 V/µm and 1.3 µm wavelength. The net gain coefficient was similarly improved between the fully capped and reduced capping systems, from 22.6 cm^{-1} to 85.2 cm^{-1}, one of the highest net gains reported in an infrared sensitized system.

C. Li et al. probed the effects of exciton-plasmon coupling by creating a photorefractive material sensitized by a blend of gold (Au) and Type II CdSe/CdTe nanoparticles at nanomolar concentrations.[64] Within the PVK:DABM: EZC:Au:Cdse/CdTe system, control samples were fabricated using each type of nanoparticle separately in order to analyze the ability of the blend to enhance charge separation efficiency and speed. Figure 1-13 illustrates that the addition of the

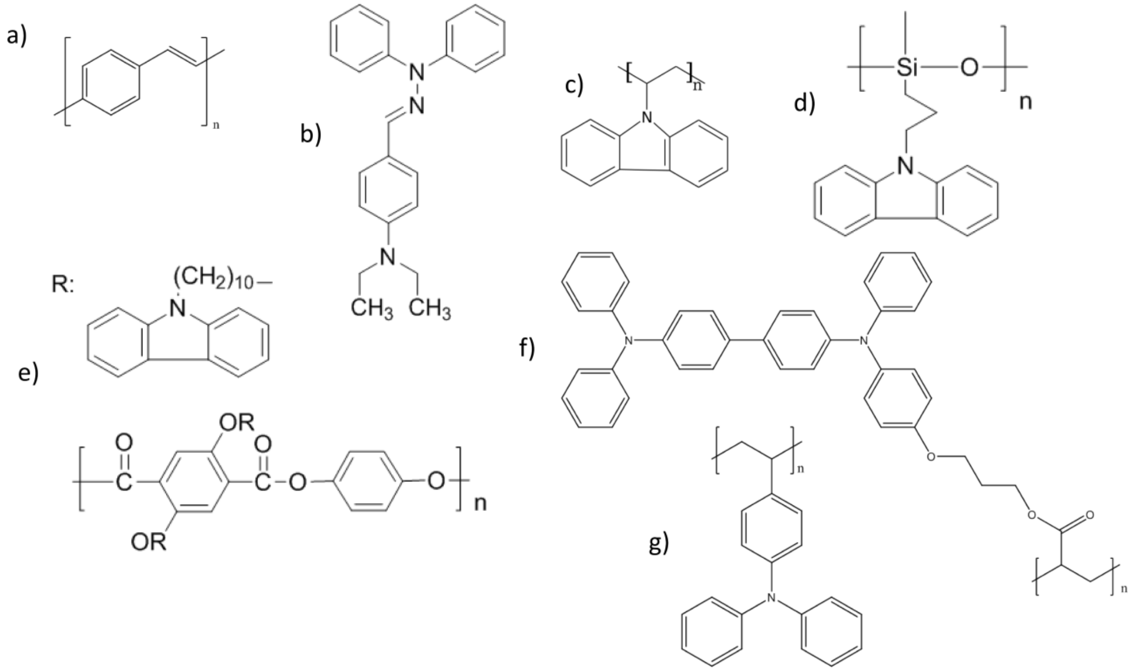

Figure 1-14: Photoconductive polymers commonly used within photorefractive polymeric systems: a) PPV (Poly(phenylene vinylene)), b) DEH (p-diethylaminobenzaldehyde-diphenylhydrazone), c) PVK (polyvinylcarbazole), d) PSX (poly[methyl-3-(9-carbazolyl)propylsiloxane]), e) (PPT-CZn poly(p-phenylene terephthalate) backbone with carbazole pendants connected through n alkyl spacers, f) PATPD (polyacrylic tetraphenyldiaminobiphenyl), g) PDAS (poly(4-diphenylamino)styrene).

Au:CdSe/CdTe blend increased the diffraction efficiency of the system beyond that of either control and decreased the response time by 66 % and 110 % to 1.25 sec^{-1}. The authors attribute this performance enhancement to faster charge carrier separation due to exciton-plasmon coupling effects.

1.4.2 Photoconductive Polymer

The polymer matrix which comprises more than half of the weight of the photorefractive media plays many roles. One of these is as a structural support, imparting the overall physical rigidity necessary for implementation into a device. Strict optical performance requirements apply to polymers used in this application, most significantly those related to the transparency of the bulk material at the wavelength of use and long-term stability. Small regions of inhomogeneity in a device, either due to phase separation or polymer crystallization cause variation of the refractive index. This can manifest as undesired refraction within the bulk of the medium or scattering, increasing system loss and degrading device performance.

The other primary role is that of charge transport, providing the path along which the holes travel in response to the space-charge field. Conductive polymers can generally be divided into two main families: those which conduct based on main chain conjugation, and those which conduct through side chain conjugation. Main chain conjugated polymers such as PPV in Figure 1-14a have a chief structural backbone that is conjugated over many repeat units of monomer. This conjugation takes the form of alternating single-double bonds and creates a delocalization of the charges allowing them to contribute to charge transport.[65] Increasing the conjugation of the backbone leads to a higher charge transport functionality but at the same time increasing the number of rotationally resistant double bonds, which reduces the flexibility of the polymer itself.[66] This rigidity leads to a more ordered system that can be prone to structured three-dimensional packing, or crystallization, especially in the case of polymers with relatively low molecular weights.[67]

Side chain conjugated polymers, such as PVK (Figure 1-14c) and PATPD (Figure 1-14f) are those in which the structural backbone is composed of few to no double bonds and does not contribute significantly to charge transport. All of the energetic delocalization occurs between side chain moieties that are close enough in proximity for some degree of orbital overlap, leading to hopping charge transport between the pendants. The energy barrier to hopping is higher than that of transport through main chain charge delocalization and, therefore, the charge carriers have a lower effective mobility in this type of system. The conjugation of the pendant itself is

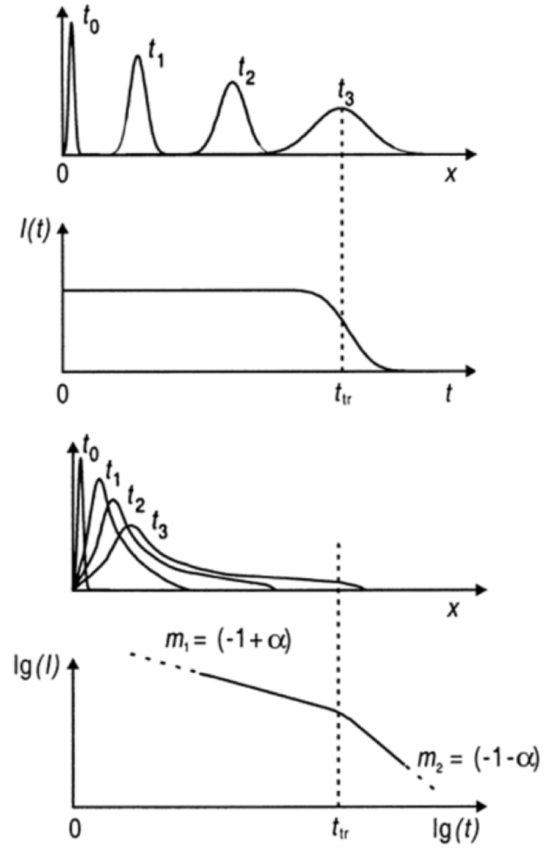

Figure 1-15: Gaussian (crystalline) vs. dispersive (semicrystalline/amorphous) transport. The two top figures illustrate Gaussian transport and the two lower figures illustrate dispersive transport. The upper graphs illustrate representative charge carrier packet motion with time while the lower graphs illustrate the current measured as a function of time. Reproduced from [66] with permission from Wiley-VCH.

what drives the transport in this case as the more conjugated the entity, the more the charge is delocalized within it, and transport can occur through it. Bulky side moieties also decrease the likelihood of crystallization, while the molecular weight of the overall polymer plays no part in this effect due to the flexibility of the main chain.[68]

Model

Charge transport in crystalline semiconductors occurs within well-defined HOMO and LUMO bands extending across the crystalline media and the Gaussian form of the charge carrier "packet" is only broadened by thermal diffusion. In semiconducting polymeric systems, the charge packet experiences the same Gaussian broadening due to thermal diffusion but experiences further variations in charge mobility due to hopping, molecular disorder and trapping. This type of transport is called dispersive transport with the differences between the effects of the two types of transport on charge packets illustrated in Figure 1-15. [66]

Hopping probability between polymer entities is affected by the long-range order of the system and the distance between conductive species. These interactions are described in the theory set forth by Marcus[69], with subsequent alterations for polymeric systems made by others.[70–72] The conceptual basis of these models is that the rate of transfer between two similar states of adjacent molecules is dependent on the electronic coupling or wavefunction overlap between the two entities, fulfilling the Franck-Condon principle. This takes the form of the integration of the initial (I) and final (F) state wavefunctions into the standard analysis. Quantum mechanical corrections tothis model take into account vibrational states and add the effect of the overlap between the initial and final vibrational states, i_{vib} and f_{vib} respectively. The charge transfer rate (k_{CT}) based on perturbation theory is defined as[73]

$$k_{CT} = \frac{2\pi}{\hbar} |\langle I|H|F\rangle|^2 |\langle i_{vib}|f_{vib}\rangle|^2 \rho(E_f) \tag{1-29}$$

where H is the system Hamiltonian and $\rho(E_f)$ is the density of states of the final system. In the high temperature regime where the vibrational states can be approximated as classical, the last two terms in (1-29) follow an Arrhenius distribution

$$|\langle i_{vib}|f_{vib}\rangle|^2 \rho(E_f) = \sqrt{\frac{1}{4\pi\lambda_0 k_B T}}\, exp\left(\frac{-(\Delta G^0 + \lambda_0)^2}{4\lambda_0 k_B T}\right) \tag{1-30}$$

$$k_{CT} = \frac{2\pi}{\hbar} |\langle I|H|F\rangle|^2 \sqrt{\frac{1}{4\pi\lambda_0 k_B T}}\, e^{\frac{-(\Delta G^0 + \lambda_0)^2}{4\lambda_0 k_B T}} \tag{1-31}$$

in which λ_0 is the reorganization energy induced by the charge transfer, the structural changes of which add to the charge transport barrier.[74] The charge transfer rate is related to mobility through

$$\mu = \frac{a^2 k_{CT}}{k_B T} \tag{1-32}$$

where a is the inter-molecular spacing.[75] The a^2 term in the definition of the diffusion coefficient decreases with increasing conformational freedom of the side chains as it allows them to pack more closely. This negative effect on mobility (as it is related to the distance per hop) is more than countered by the increased value of the overlap integrals between the molecular wavefunctions. It is based on this fact that in systems exhibiting higher main chain flexibility, an associated higher charge mobility has been observed, as shown by Li et al.[68]

The electric field dependence can be described through the consideration of the Poole-Frenkel effect, describing the associated reduction of the effect of the Coulomb potential on a charge carrier. The relation between the mobility and electric field follows

$$\mu(E) = \mu(0)\, exp\left(\sqrt{\frac{Ee^3}{\pi\epsilon\epsilon_0}} \Big/ k_B T\right) \tag{1-33}$$

This simple relation is only valid at low field strengths, as higher fields start affecting trapping and wavefunction overlaps in more significant ways.[46] Although the charge carriers in most semiconducting polymers are holes[76], Benerjee et al. found that at electric fields above 40 V/µm in a system composed of PVK:PDCST:ECZ-BBP:C_{60}, the mobility of the electrons begins to reach a significant level.[77]

Another electric field effect that comes into play regarding the majority of photorefractive polymers derives from the presence of polar molecules within the matrix.[78] The dipolar disorder model states that randomly oriented dipoles within the medium increase the width of the energy distribution of the transport manifold. The Gaussian width of this distribution that is due to the dipolar contribution increases with increasing dipole moment and concentration and decreases with increasing transport site separation. Goonesekera and Ducharme found that not only the polar chromophore, but also the polarity of the charge transport agent (CTA) follows this relation.[79] Though a large chromophore dipole moment is necessary for significant nonlinear effects, this also leads to lower mobilities and overall a longer photorefractive response time.

Molecules

The first report of the photorefractive effect in a polymeric system by Ducharme et al. was based on a nonlinear host matrix of bis-A-NPDA, bisphenol-A-diglycidylether (bisA) combined with the nonlinear chromophore 4-nitro-1, 2-phenylenediamine (NPDA).[12] While this cross-linkable polymer provided all of the nonlinear optical functionality needed for the device, it was not charge transporting, leading the researchers to include the charge transporting molecule p-diethylaminobenzaldehyde-diphenylhydrazone (DEH)[80] (Figure 1-14b) in a range of concentrations. They found that for increasing concentrations of DEH, the photoconductivity, gain and diffraction efficiency increased, indicating that higher mobilities of the photoinduced charges contributed positively to the development of the space charge field. Transport in this system occurred via hopping between the interspersed DEH molecules, not along a polymer main or side chain.

Shortly following this report, Zhang, Cui and Prasad developed a device in which the polymer matrix functionality and the charge transporting agent were both provided by PVK (Figure 1-14c) while photosensitization was provided by C_{60}.[81] Combined with the nonlinear chromophore DEANST (4-N,N-diethylamino-β-nitrostyrene), this composite exhibited photorefractive properties similar to its fully functionalized contemporaries. One of the major contributions of this system was its separation of photoexcitation, charge transport, and nonlinear functionalities, enabling future analysis and optimization of each component separately. The first photorefractive polymer device to reach 100 % diffraction efficiency was in a PVK based system reported by Meerholz et al. (PVK:DMNPAA (2,5-dimethyl-(4-p-nitrophenylazo) anisole):ECZ:TNF) leading to the proliferation of PVK in photorefractive research.[13] While PVK based composites have exhibited high diffraction efficiency and gain, this side-chain transporting polymer has low hole mobilities on the order of 10^{-7} to 10^{-6} $cm^2/(Vs)$ [82] leading to long response times.[38] Mansurova et al. increased the hole lifetime in a PVK:TNF composite through the addition of 20 nm diameter copper-doped $LiNbO_3$ particles.[83] These particles do not contribute directly to charge generation or transport but instead act as electron traps within the system, equalizing the sensitizer anions and in the steady-state, increasing the number of non-equilibrium holes. Though these nanoparticles were shown to reduce the mobility within the system due to a larger drift barrier, the barrier to recombination and corresponding hole lifetime increased at a faster rate, leading to an overall higher photoconductivity within the system.

Kinashi et al. recently performed a study on a series of PVK:7-DCST:ECZ:PCBM/TNF polymers characterizing the effect of polymer molecular weight and grating spacing on photorefractive polymer performance.[84] They found that between 23,000 g/mol and 860,000 g/mol, the diffraction efficiency, response rate and sensitivity all increased with increasing molecular weight in the TNF sensitized system. This was attributed to the increasing density of dimer cation sites on larger molecular weight polymer chains, adding to the number density of traps within the system. Grating spacing analysis was performed on PCBM sensitized materials with the results (shown in Figure 1-16) clearly indicating a trend of decreasing gain

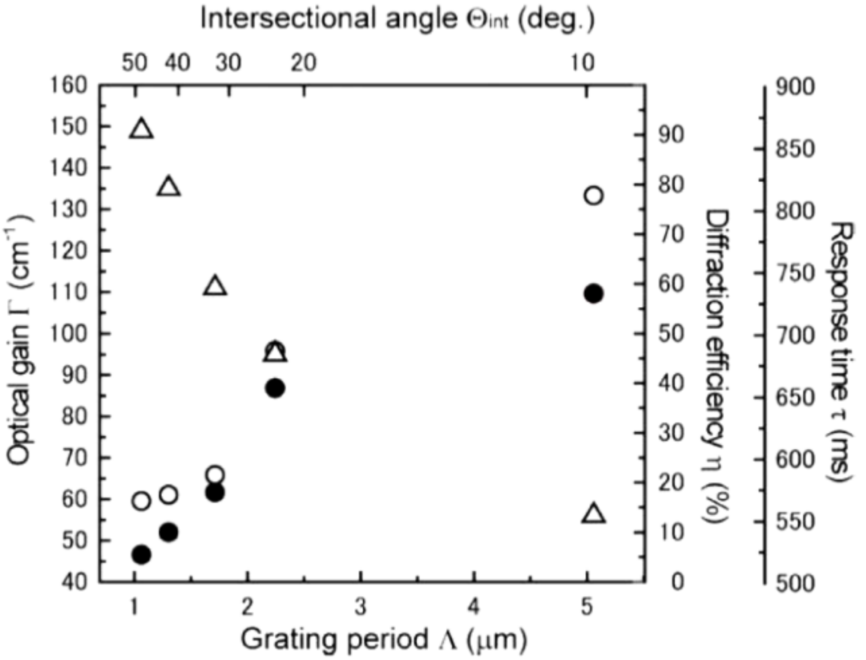

Figure 1-16: Analysis of relation between the grating period and optical gain (triangles), diffraction efficiency (filled circles) and response time (open circles). Reproduced from [84], with permission from Wiley-VCH.

with grating period but at the same time an increasing diffraction efficiency and response time with grating period increase. While the total offset between the incident illumination and the resulting index remains constant throughout the range of grating conditions, the phase offset relative to the grating spacing increases, leading to the relation between increasing gain and decreasing grating spacing. The decrease in diffraction efficiency and increase in response time with decreasing grating spacing are indicative of a trap limited response, with higher spatial frequencies requiring more traps to resolve than are available in the system.

One drawback to PVK is that the HOMO level (5.9eV) is below that of many of the commonly integrated chromophores, leading to transport in the chromophore molecule taking on an energetically favorable probability. The chromophores act as traps in this case, increasing the ionized acceptor density and the associated deep trap density. This leads to a decrease over time in the photoconductivity and speed of grating formation as the sample is illuminated.[48, 85]

Aggregation of species within molecularly doped PVK systems is another drawback to their implementation, leading to phase separation and a short shelf life. Polar components within the low T_g plasticized composites, such as high figure of merit chromophores, do not significantly interact with the non-polar carbazole side chains of PVK, leading to low solubility and long term instability.[50]

Similar to PVK, PSX (poly[methyl-3-(9-carbazolyl) propylsiloxane]) is a polysiloxane based backbone with carbazole side chains that exhibits a lower T_g due to the higher flexibility of the backbone. Lower T_g polymers require less plasticizer to achieve high chromophore rotation, increasing the percentage of active media within the volume. Additionally, polar molecules are more soluble in the polar PSX than the non-polar PVK, leading to less aggregation over time.[86, 87] Unimpressive photorefractive responses have offset these beneficial aspects with maximum diffraction efficiencies of 56 % at 30 V/µm and gain of 180 cm^{-1} at 50 V/µm representing standard results for these materials.[88] One interesting interrogation by Wolff et al. was performed with this PSX base (Figure 1-14d) in which the researchers observed an increase in the recording speed during pulse recording by a factor of 1000 when concurrently irradiated by an intense continuous wave (CW) laser. This drastic improvement was attributed to the detrapping of charges from shallow traps by the CW illumination, increasing the effective mobility of the holes. While the response rate increased with increasing CW intensity, the overall diffraction efficiency of the system decreased since more of the sensitizers had already been excited prior to the pulsed illumination and the contrast of the index grating was adversely affected.[89]

Kwon et al. synthesized a rigid poly(p-phenylene terephthalate) backbone with carbazole pendants connected through *n* alkyl spacers (PPT-CZn) (Figure 1-14e).[90] These photoconductive

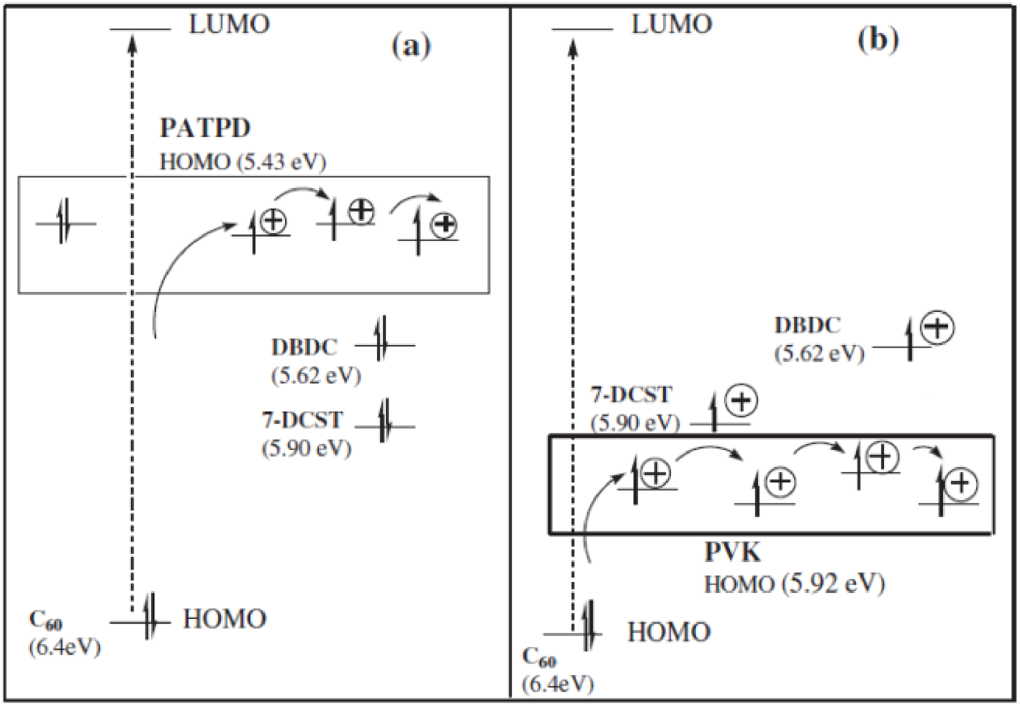

Figure 1-17: Representation of the various charge generation, transport and trapping processes in a) PATPD and b) PVK for the chromophores 7-DCST and DBDC. Reproduced from [94], with permission from Wiley-VCH.

polymers self-organize into layers with the spacing between the backbones determined by the length of the alkyl chain. The longer alkyl chains also lower the glass transition temperature of the system, with chain lengths over eight units long in the PPT-CZ:DDCST:C_{60} system resulting in a sub-room temperature T_g with no plasticizing dopant. Photorefractive properties of these devices are competitive with standard plasticized configurations with 93 % diffraction efficiency at 100 V/µm and gain of 250 cm^{-1} at 60 V/µm. Phase stability was observed under standard storage conditions for over six months. While these devices are unique in their high performance without plasticization, they do suffer from low response rates, with measured values ranging from 0.02 sec^{-1} to 1.3 sec^{-1} at 100 V/µm.[91, 92]

Polymers composed of TPD (tetraphenyldiaminobiphenyl) based monomer have exhibited mobilities of 10^{-4} to 10^{-5} $cm^2/(Vs)$, orders of magnitude larger than PVK systems.[93]

Thomas et al. developed polyacrylic TPD (PATPD), TPD chains connected to the polyacrylate backbone through flexible alkoxy linkers designed to lower the T_g of the polymer matrix (Figure 1-14f). The HOMO level of PATPD is above that of the DCST chromophore usually found in the composites including TPD based transport polymers, shown in Figure 1-17. This makes transport of the charge carriers to the chromophore energetically unfavorable, reducing trap density and preventing the exposure dependent response seen in PVK composites. Phase stability of the PATPD:7-DCST:ECZ:C_{60} device was enhanced, allowing chromophore loadings up to 35-40 wt% to further enhance the index modulation.[94] The response time in this type of device has been observed as low as 300 µs under pulse writing conditions at 95 V/µm.[28] By using a co-polymer system of carbaldehyde aniline (CAAN) groups interspersed with TPD groups on a polyacrylate backbone (PATPD-CAAN:FDCST:ECZ), Tay et al. developed a device that exhibited near 90 % diffraction efficiency at only 40 V/µm and used it to display updatable three dimensional stereograms.[95]

PDAS, or poly(4-diphenylamino)styrene, shown in Figure 1-14g, has a hole mobility of 10^{-4}-10^{-3} $cm^2/(Vs)^{-1}$, higher than those reported for PATPD.[96] Additionally, the ionization potential is 5.78 eV, and like TPD systems, is higher than for commonly used chromophores.[97] Both of these characteristics indicate that this hole conducting polymer would be a valuable addition to the PR arsenal and suggest a fast photorefractive response. Its initial implementation in a PDAS:7-DCST:DPP (diphenyl phthalate):TNF system exhibited performance similar to that of the PVK based reference (diffraction efficiency <1 % and gain 10-20 cm^{-1}, both at 60-65 V/µm) but they did note a decreased response times in the PDAS system of 0.4 sec vs. 1.2 sec in the PVK device as expected. Further implementation in a PDAS:FDCST:ECZ:PCBM device remained on the low end for diffraction efficiency at 35.1 %, but the response time was decreased significantly to 39 ms, allowing a demonstration of real time recording and display of two dimensional images.[98]

1.4.3 Chromophores

Analysis of light-matter interactions generally focuses on the response of the material to the electric field of the irradiation. In a majority of cases, the nonlinear response is neglected since the external electric field amplitude is significantly smaller than the internal electric fields of the atoms and molecules themselves, and its effect on the system is negligible. The proliferation of lasers, however, has enabled the application of high energy fields capable of driving significant nonlinear responses, opening the door to many useful phenomena. A molecule has an induced dipole moment ($\Delta\mu$) related to the internal electric field (E) through

$$\Delta\mu = \alpha E + \beta E^2 + \cdots \tag{1-34}$$

where α is the polarizability and β is the first hyperpolarizability. The internal electric field in chromophores is often due to the charge distribution between the acceptor and donor entities on the molecule. When it is exposed to an optical field (E_{opt}), the total electric field (E_T) is equal to the sum of E_{opt} and E, *with* the microscopic induced polarization (p) related to the dipole through[99]

$$p = \alpha(E_{opt} + E) + \beta(E_{opt} + E)^2 + \cdots \tag{1-35}$$

While all media exhibit a first and third order nonlinear response, the symmetry of the bulk material must be broken in order for the material to show a second order response, such as the linear electro-optic response. This can be achieved through the orientation of these polar anisotropic molecules within the polymer matrix by poling, or aligning them in response to an external field (E_0). Materials can be poled at elevated temperatures and cooled to maintain the orientation or poled in a low T_g polymer during use by application of an external field, thermodynamically returning to a random configuration once the field is removed.

Model

The oriented gas model can be used to relate the microscopic response of the molecules to the macroscopic response of the poled polymer by making some significant approximations: poling occurs above T_g and the chromophores are free to rotate in response to the applied field, ignoring any coupling to or reaction from the surrounding polymer matrix; the chromophores are cylindrically symmetric, with a non-vanishing hyperpolarizability tensor along only one axis (β_{ZZZ}); the permanent dipole moment of the chromophore is oriented along the same axis as the hyperpolarizability; and it is assumed that the chromophores themselves are independent and non-interacting.

The final assumption above allows the simplification of the bulk response into the thermodynamic average of the N individual molecular responses in relation to their dipole orientation. The bulk terms relating the electric field to the material response are $\chi^{(1)}$ and $\chi^{(2)}$, the linear and second order nonlinear optical susceptibilities, respectively. The second order nonlinear optical susceptibility defines the second-order nonlinear optical response and for small poling fields ($\leq$ 100 V/μm), its components along the poling field direction ($\chi^{(2)}_{ZZZ}$) and perpendicular to the poling field direction $\left(\chi^{(2)}_{ZXX}\right)$ are

$$\chi^{(2)}_{ZZZ} = N\frac{\mu^* E_0}{5k_B T}\beta^*_{ZZZ};\ \chi^{(2)}_{ZXX} = N\frac{\mu^* E_0}{15k_B T}\beta^*_{ZZZ} \tag{1-36}$$

The * parameters are those in which local field corrections have been taken into account and are given by

$$\mu^* \approx f_0\mu\, ; \quad \beta^*_{ZZZ} \approx f_\infty^2 f_0 \beta_{ZZZ} \tag{1-37}$$

$$f_0 = \frac{\epsilon(n^2+2)}{2\epsilon + n^2}\, ;\ f_\infty = \frac{n^2+2}{3} \tag{1-38}$$

where f_0 and f_∞ are the Onsager and Lorentz-Lorenz field correction factors for a spherical cavity.[100]

In a photorefractive polymer operating near or above T_g, the linear electro-optic effect relates the susceptibility to the change in refractive index ($\Delta n_{Z,EO}$) due to the total poling field ($E_T = E_{applied} + E_{SC}$):

$$\Delta n_{Z,EO} = \frac{\Delta\chi^{(2)}_{ZZZ}}{2n} E_T = N\frac{\mu^*\beta^*_{ZZZ}}{10nk_BT}E_T^2 \tag{1-39}$$

$$\Delta n_{X,EO} = \frac{\Delta\chi^{(2)}_{ZXX}}{2n} E_T = N\frac{\mu^*\beta^*_{ZZZ}}{30nk_BT}E_T^2 \tag{1-40}$$

Note that this response is now second order with respect to the field due to the field dependence of the hyperpolarizability. The polarization of the reading beam additionally affects the measured refractive indices in the two directions with one factor for light polarized in the plane ($\Delta n_{p,EO}$) and another for out of the plane ($\Delta n_{s,EO}$)

$$\Delta n_{s,EO} = \frac{8\pi}{n}\frac{N\mu^*\beta^*_{ZZZ}}{15k_BT}E_0|E_{SC}|\cos\varphi \tag{1-41}$$

$$\Delta n_{p,EO} = \frac{8\pi}{n}\frac{N\mu^*\beta^*_{ZZZ}}{15k_BT}E_0|E_{SC}|[\cos\varphi\cos\alpha_1\cos\alpha_2 + 3\cos\varphi\sin\alpha_1\sin\alpha_2 + \sin\varphi\sin(\alpha_1+\alpha_2)] \tag{1-42}$$

where φ is the angle between the grating vector and the external field direction and α_1 and α_2, are the angle of the beams with respect to the sample normal.

The refractive index modulation of photorefractive polymers measured in response to illumination exceeds the expected contribution from the linear electro-optic effect above. Moerner et al. in 1994 discovered that this discrepancy was due to the effect of spatially modulated birefringence of the chromophores in addition to the dc response from the external poling field.[17] This effect is due to the linear polarizability of the molecule along the long axis ($\alpha_{\parallel}$) and across the width ($\alpha_{\perp}$) and its relation to the first order susceptibility[101]

$$\chi_{ZZ}^{(1)} = N(\alpha_{\parallel} - \alpha_{\perp})\frac{2}{45}\left(\frac{\mu^* E_T}{k_B T}\right)^2 ;\ \chi_{XX}^{(1)} = -N(\alpha_{\parallel} - \alpha_{\perp})\frac{1}{45}\left(\frac{\mu^* E_T}{k_B T}\right)^2 \tag{1-43}$$

and through this, to the change in refractive index due to birefringence ($\Delta n_{Z,BR}$)[17]

$$\Delta n_{Z,BR} = \frac{\Delta\chi_{ZZ}^{(1)}}{2n} = N\frac{\Delta\alpha}{45n}\left(\frac{\mu^*}{k_B T}\right)^2 E_T^2 \tag{1-44}$$

$$\Delta n_{X,BR} = \frac{\Delta\chi_{XX}^{(1)}}{2n} = -N\frac{\Delta\alpha}{90n}\left(\frac{\mu^*}{k_B T}\right)^2 E_T^2 \tag{1-45}$$

and taking into account angles of incidence and polarization of writing and reading beams,[100]

$$\Delta n_{s,BR} = -\frac{4\pi N}{45n}\Delta\alpha\left(\frac{\mu^*}{k_B T}\right)^2 E_0|E_{SC}|\cos\varphi \tag{1-46}$$

$$\Delta n_{p,BR} = \frac{4\pi N}{45n}\Delta\alpha\left(\frac{\mu^*}{k_B T}\right)^2 E_0|E_{SC}|\Big[2\cos\varphi\sin\alpha_1\sin\alpha_2 - \cos\varphi\cos\alpha_1\cos\alpha_2 + \frac{3}{2}\sin\varphi\sin(\alpha_1+\alpha_2)\Big] \tag{1-47}$$

As the diffraction efficiency of a photorefractive device is proportional to the square of the change in refractive index ($\sin^2(\Delta n) \sim \Delta n^2$ valid in the low efficiency regime), this is an important parameter to enhance in order to maximize the material response. A figure of merit (FOM) was developed to describe the nonlinear optical molecule within a photorefractive polymer matrix summing the first and second order polarizabilities. Removing common terms and neglecting the reading-writing conditions, it takes the form below with the addition of a molar mass (M)

$$FOM = \frac{1}{M}\left(\frac{2}{9k_B T}\Delta\alpha\mu^2 + \beta\mu\right) \tag{1-48}$$

This FOM has been used in the optimization of chromophores for use in PR materials and is dependent on the dipole, linear polarizability and hyperpolarizability.[102] The permanent dipole of a molecule is related to the electron affinity of donor and acceptor groups connected by a π-conjugated bridge. These "push-pull" molecules and the linear response of the molecule to an electric field, or linear polarizability, is to favor charge flow in the direction of the acceptor while opposing flow in the direction of the donor functionality. The magnitude of the linear polarizability is related to the degree of conjugation of the bridge. Often these molecules are called chromophores since the electron delocalization along the molecule creates absorption bands in the visible regime, resulting in highly colored entities.[100]

Hyperpolarizability is attributed to the degree of ground state polarization within the molecule, or the degree of charge separation in the unexcited molecular state. The bond-length alternation (BLA) model has been developed to relate this degree of charge separation to the geometrical average bond length between carbon atoms along the backbone. In a conjugated molecule, this is often a single-double bond series and with weak donors and acceptors, this corresponds to a high degree of BLA. Alternatively, in a system incorporating strong donor and acceptor end groups, the relative contribution of the bond length differences to the overall energy structure is negligible. This relative effect can be parameterized using bond order alternation (BOA), which describes the transfer state of the charge across the molecule.[99] Kippelen et al. calculated the two terms of the FOM based on the BOA parameter and found that the contribution of the hyperpolarizability term to the magnitude was far outweighed by the contribution of the linear polarizability term in contradiction to most nonlinear materials applications (Figure 1-18). The first term is also quadratically dependent on the dipole moment of the molecule, causing it to be of more significance than previously assumed, leading the majority of further work in chromophore optimization to focus on maximizing the linear polarizability and dipole.[102]

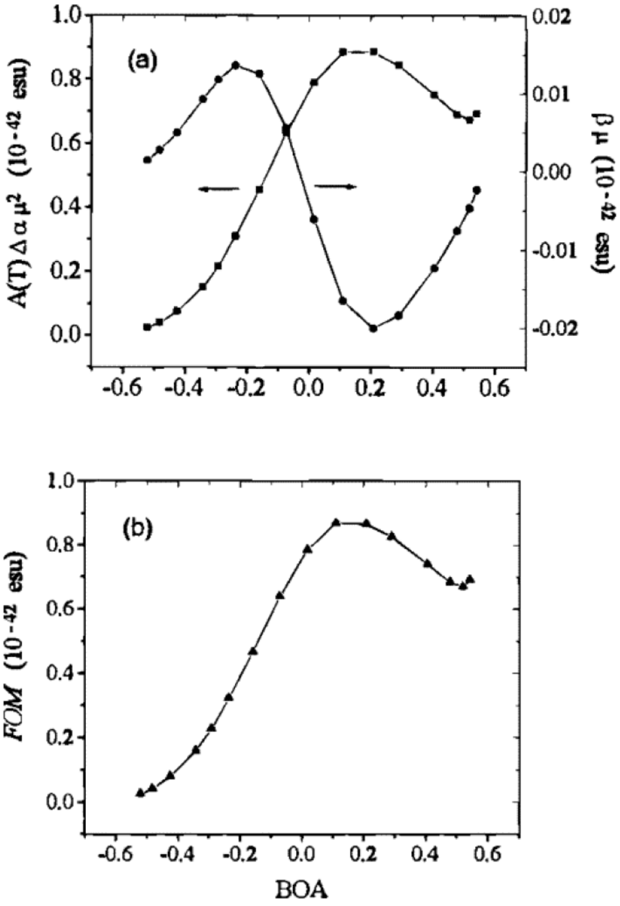

Figure 1-18: Electrooptic (βμ) and orientational (≈Δαμ^2) contributions a), and FOM b) as a function of BOA. Reproduced from [102], with permission from American Chemical Society.

Aggregation of polar molecules is a significant barrier to the incorporation of high FOM (large dipole moment and linear polarizability) chromophores into polymeric systems. Large dipole moments lead to crystallization as high melting temperature solids, resulting in inhomogeneity and scattering within the otherwise amorphous film. The attachment of long alkyl chains on the ends of these molecules creates a buffer between them, reducing the tendency to crystallize but at the same time reducing the FOM as the molar mass increases, often negating the benefit.[88] Large dipole moments and high concentrations also lead to non-optimal poling as the intermolecular interactions between the chromophores begin to disrupt the alignment to the poling field.[103]

Molecules

The chromophore has been found to take part in photorefractive functionalities other than those that are birefringence based in the case of specific polymer formulations. West et al. found that hole transport in a matrix composed of ~50 wt% dye in a non-conductive polymer was not significantly different from that in a similar system with PVK. It should be noted that the HOMO level of the dye was above that of the PVK, a configuration which lends itself nicely to transport from the PVK to the chromophore. This led to the conclusion that chromophores can contribute significantly to charge transport in systems of such high loading.[104] At lower loading in the same type of system, the chromophore was found to act as a trapping agent, again due to the relative HOMO of the dye and CTA. In this case the concentration of the chromophore was not high enough to ensure sufficient percolation of the dye species to provide a transport avenue.[48] With increasing concentration, the mobility of charges does increase for a dye HOMO level appropriate for transport participation. For a HOMO level below that of the transport matrix, as is the case for 5CB in the same figure, there is no appreciable concentration dependence of mobility.[22] The trap depth was also related to the HOMO level of the chromophore with respect to the transport through the analysis of multiple dicyanostyrene (DCST) and cyano ester styrene (CEST) derivatives (FDCST in Figure 1-19a) at 35 wt% within a PVK:chromophore:BBP:C_{60} composition. Across a HOMO level range of 80 meV, the speed of grating formation and photoconductivity were found to increase with decreasing HOMO level, indicating less chromophore participation in transport for lower HOMO energy.[105]

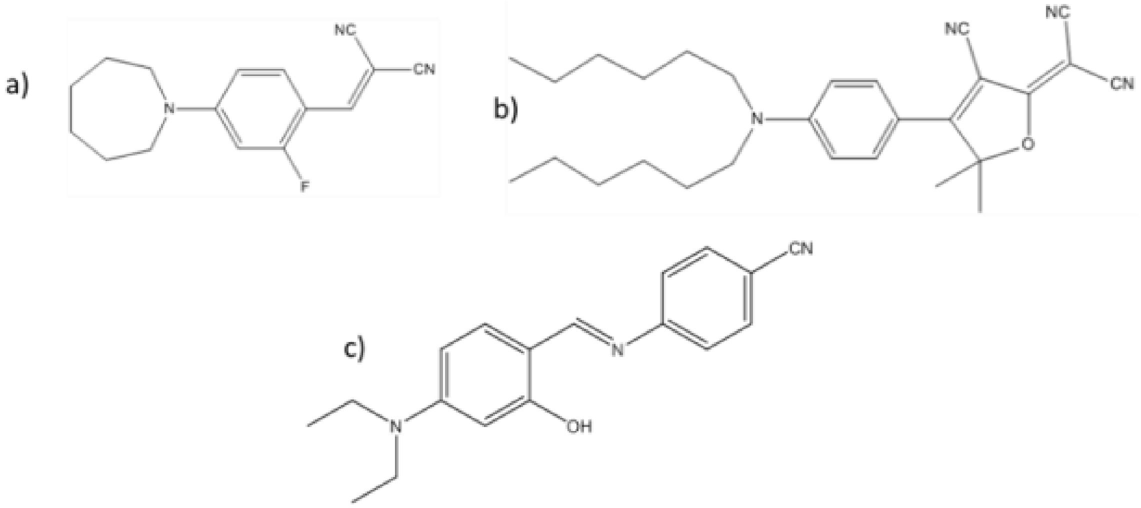

Figure 1-19: Chromophores commonly used within photorefractive polymeric systems: a) FDCST (fluorinateddicyanostyrene 4-homo- piperidino benzylidine malonitrile), b) DCDHF-6 (2-dicyanomethylene- 3-cyano-2,5-dihydrofuran) and c) Dc (4-[(4-(diethylamino)-2-hydroxy- benzylideneamino]benzonitrile).

Due to their high absorption in the visible wavelength regime, many chromophores can also act as sensitizers within the polymer as reported by Ostroverkhova and Singer. In this work, the photogeneration cross section of the film was measured as a function of concentration of AODCST and the liquid crystal 5CB, but while AODCST has significant absorption at the wavelength of measurement, 5CB has very little. Accordingly, the photogeneration cross section increased with increasing concentration of AODCST while remaining constant across various 5CB loadings.[22]

One attractive multifunctional polymeric system under study is based on 30 wt% DCDHF (dicyanomethylenedihydrofuran) and recently achieved high gains and efficiency with fast response times. The first record of a DCDHF-6 (Figure 1-19b) based fully functionalized system reports gain of 180 cm^{-1} and diffraction efficiency of 70 % at 50 V/µm but the characterization of the response time showed vastly different long and short time constants. This indicated that the system response was orientationally limited.[106] Gallego-Gomez et al. recently studied various plasticization levels of this system in order to speed up the writing and erasing times of the material as well as increase the dielectric breakdown limit. They were able to successfully lower the T_g of the composite in order to achieve excellent performance, with a gain of 350 cm^{-1}, buildup and erasure times of tens of milliseconds at 120 V/µm, and near complete diffraction efficiency at 70 V/µm corresponding to a refractive index modulation of 0.024.[31]

Herrera-Ambriz et al. recently reported a new benzonitrile based nonlinear optical chromophore (Figure 1-19c) Dc (4-[(4-diethylamino-2-hydroxy- benzylideneamino] benzonitrile).[107] Their PVK:Dc:ECZ:C_{60} films exhibited high internal diffraction efficiencies of ~90 % at moderate fields of 56 V/µm with a chromophore loading of only 25 wt%. The lower concentration of this chromophore required to effectively diffract may lead to more long term phase stability in functional devices. Additionally, low absorption in the visible wavelength band (absorption peaks at 406 nm) increases the transmission of the probe beam, resulting in increased external diffraction efficiencies compared to similarly performing, lower transmission devices.

1.4.4 Plasticizers

The glass transition temperature of the majority of the polymer systems discussed here are well above the operating temperature, ranging from 100 to 200 °C.[108] Since 70-80 % of the nonlinear optical effect is due to reorientation of the chromophores in competitive systems,[109] either the operating temperature of the system must be increased or the T_g must be lowered to facilitate rotation of the small molecules. Cheng, Swedek and Prasad thermally fixed their gratings by heating the device during the writing process and cooling it back down to hold the image.[110] Li and Wang locally heated the region of recording using a CO_2 laser during writing allowing them to record into high T_g materials.[111] One benefit to these methods is that no external electric field needs to be applied after writing in order to maintain alignment of the chromophores and the

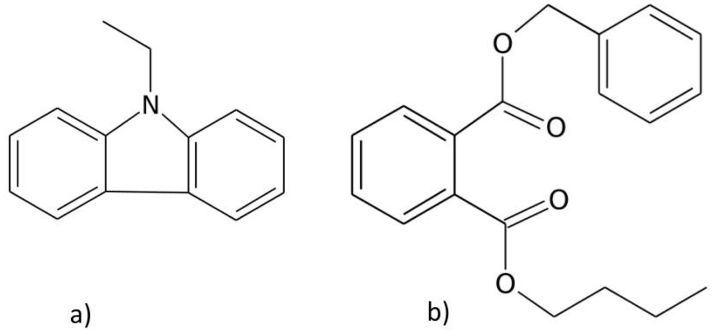

Figure 1-20: Plasticizers commonly used within photorefractive polymeric systems: (a) ECZ (ethyl carbazole), (b) BBP (benzyl butyl phthalate).

gratings will persist for several hours. The main drawback to thermal methods is the thermal degradation of the polymer films, reducing the photorefractive response of the media over time.

Lowering the glass transition temperature is achieved through the addition of inert small molecules into the polymer matrix. These small compounds disperse within the amorphous material and disrupt the long-range order of the polymer chains, increasing the free volume within the bulk and increasing fluidity.[67] It has been shown that in plasticized systems, the speed of the photorefractive response is correlated with the photoconductivity observed in the device, indicating that the conductivity, and not orientation, has become the limiting factor in the rate of grating buildup.[105] Common plasticizers used are ECZ and BBP (Figure 1-20) with loadings generally on the order of 15-30 wt%.[112]

These small molecules do not contribute directly to the photogeneration, conductivity or nonlinear response of the system, and as such decrease the photorefractive response with increasing loading. Additionally, since the molecules are freer to move, aggregation in highly plasticized systems becomes a main avenue of device failure and shelf life reduction.[91] Though the plasticizer itself does not contribute to charge creation or transport, the increased plasticity of the material leads to a distinctly larger dark current in comparison to unplasticized composites.

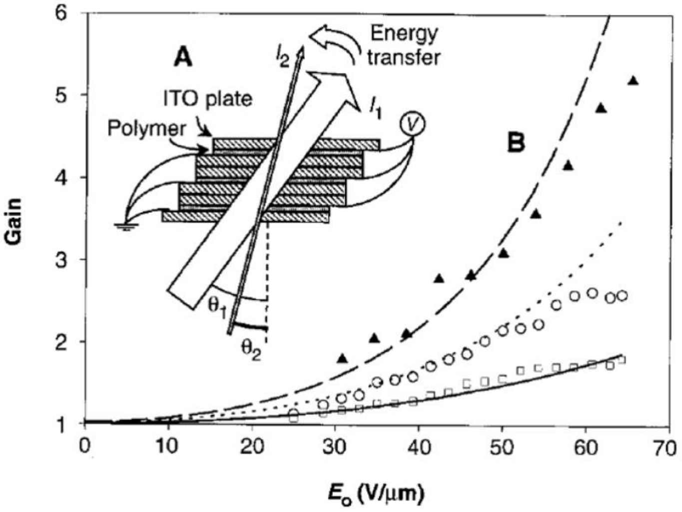

Figure 1-21: A) The multi-layer geometry used in the experiment consisting of 140 µm thick layers. B) Two beam coupling results for single layer (squares), double layer (circles) and triple layer (triangles). Reproduced from [117], with permission from AAAS.

This has been attributed to the increased conformational freedom of the polymers freeing ionic impurities within the bulk. After prolonged application of an electric field, the dark current decays as these charges accumulate near the electrodes.[22]

1.4.5 Electrodes

The electrodes in a photorefractive polymer system are an integral part of the device, as the application of an external electric field is required for operation. It is this electric field that orients the chromophore molecules and breaks the bulk symmetry of the system, enabling the realization of the electro-optic effect in addition to the orientational enhancement of the birefringence. One of the main requirements for these electrodes is their transparency at the wavelength of use while still exhibiting high electrical conductivity.

In a standard "sandwich" geometry PR device, the PR material is located between two transparent conducting electrodes covering the entire active area of the device. When a voltage is applied across the electrodes, the subsequent electric field is constant throughout the material

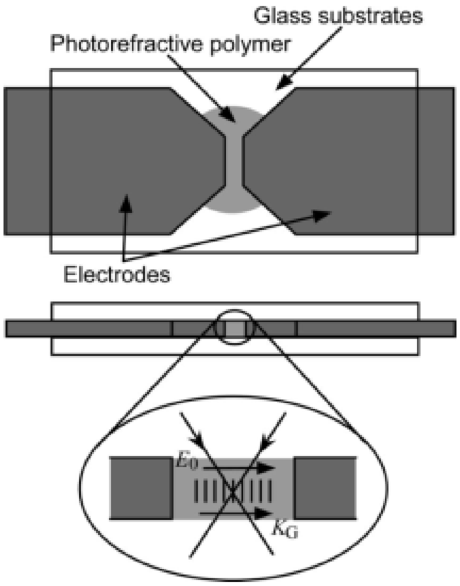

Figure 1-22: Geometry of the coplanar electrode device used by Hayasaki et al. Reproduced from [118], with permission from AIP Publishing LLC.

with units of Volts/distance and is perpendicular to the electrodes in all space (assuming electrodes of infinite extent). General photorefractive polymers require the use of an external electric field between 10-100 V/µm, but in order to generate this across standard device thicknesses of 50-100 µm, an overall voltage of 5-10 kV must be applied across the electrodes.[50, 109] For applications in which thicker films are needed to enhance the photorefractive response or to narrow the Bragg selectivity of the gratings, alternate electrode configurations must be employed.

Modeled after the stratified volume holographic optical element (SVHOE)[113, 114], or a hologram composed of multiple sub-layers of media, Stankus et al. developed a four layer system using stacks of photorefractive polymer films interspersed with transparent electrodes and glass substrates similar to that shown in the inset of Figure 1-21.[115] One of the essential features of their implementation was the coherent addition of the fields from each layer, resulting in diffraction efficiencies of multiple layers surpassing the linear superposition of the layers

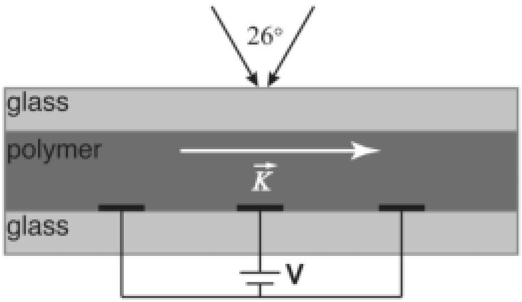

Figure 1-23: Coplanar electrode illustration, not to scale. Reproduced from [119], with permission from The Optical Society.

separately. The other feature was a sharpening of the angular selectivity through the combination of multiple layers according to coupled wave theory.[2] De Vre and Hesselink followed this with a theoretical analysis of the diffraction from layered photorefractive films providing closed form solutions for diffraction efficiency and Bragg selectivity for this type of device.[116] Grunnet-Jepsen, Thompson, and Moerner employed this configuration to develop an externally adjustable gain device for a photorefractive polymer optical amplifier. While

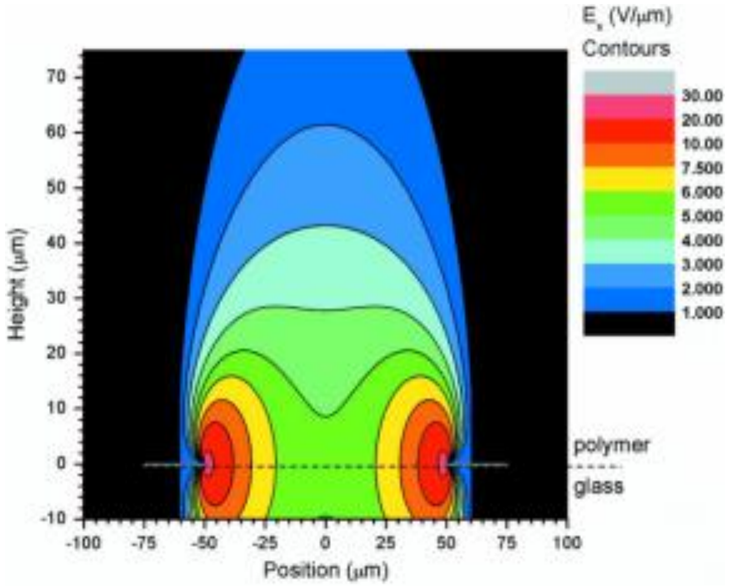

Figure 1-24: Contour map of the electric field projection onto the grating vector above two oppositely charged electrodes. The simulation was performed with 25 µm wide electrodes spaced by 100 µm and at a potential of 1 kV. Reproduced from [119], with permission from The Optical Society.

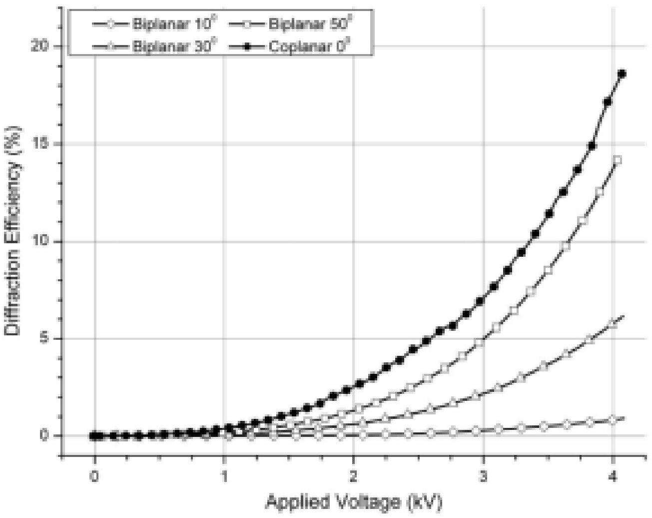

Figure 1-25: Diffraction efficiency as a function of applied voltage comparing the standard sandwich style geometry at various tilt angles to a coplanar geometry. Reproduced from [119], with permission from The Optical Society.

photorefractive gain has reached values over 200 cm^{-1}, the physically obtainable response is significantly smaller due to the thin layers. By stacking these devices, the total gain (not normalized by the sample thickness) increased as the power of the number of layers and for the three layer device reached a factor of 5 gain, shown in Figure 1-21.[117]

Hayasaki et al. implemented an alternative electrode geometry they termed “coplanar” consisting of two aluminum electrodes separated by 100 µm between which the photorefractive polymer was located (Figure 1-22). The effect of this geometry is that the external electric field is applied perpendicular to the plane of incidence of the writing beams, resulting in aligned grating and electric field vectors and maximizing the photorefractive response. Electrode/film thicknesses varying from 100-600 µm were tested with this configuration and values of gain peaked at 35 cm^{-1} for the 600 µm sample. The limiting parameter of this device was the small active area, constraining the angles of incidence and beam sizes used and restricting the applicability of this geometry to display oriented devices.[118]

Christenson et al. implemented a different coplanar device geometry (see Figure 1-23). In this system, both the positive and negative electrodes are in the same plane, but are transparent indium tin oxide (ITO) electrodes and create an electric field that arcs through the polymer film on top from one electrode to the other (Figure 1-24). The geometry of the electric field within the polymer is complex, but for the standard 1:4 or 1:5 electrode width to spacing ratio, the electric field is generally parallel to the electrode plane between the electrodes. The thin transparent electrodes of this device make it more useful for applications which need a large active area. The enhanced projection of the grating vector on the electric field vector afforded by this geometry increased the photorefractive performance, with a 30 µm thick active layer in an unslanted geometry outperforming 105 µm thick standard sandwich samples at peak recording conditions, shown in Figure 1-25.[119]

1.5 Holography and Holographic Displays

The unique dynamic and rewritable properties of PR polymer materials have allowed researchers to explore new applications such as updatable holography and in-situ imaging, many taking advantage of the self-development of the grating. Additionally, the ease with which these devices can be fabricated with large active areas makes them a valuable alternative for applications which have historically used photorefractive crystalline media. This section will begin with a primer on holographic image recording and reconstruction in thick films followed by an overview of recent advancements in the implementation of photorefractive polymers into holography based systems.

As previously discussed, a holographic grating is formed in a material when two beams interfere within a media that can translate that intensity pattern into a correlating pattern in the index of refraction or absorption. For the purpose of this analysis, the beams can be

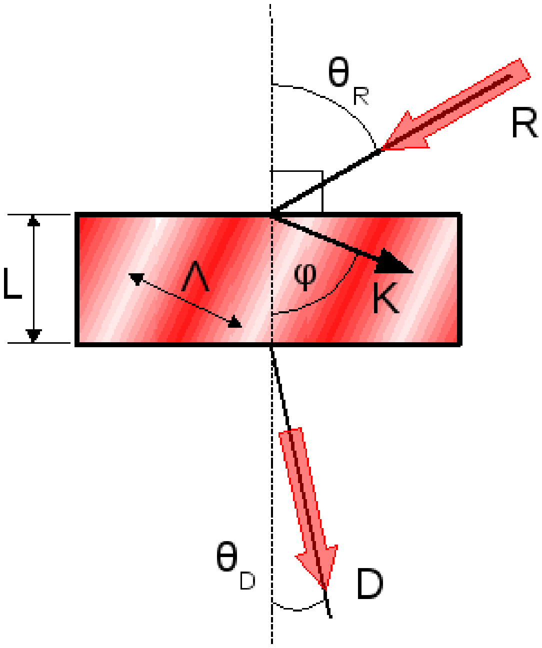

Figure 1-26: System geometry for the coupled wave theory analysis of refractive index modulation based transmission gratings.

approximated as two intersecting plane waves, in which case the film modulation takes on a sinusoidal form. A probe beam incident upon the material at the same angle as one of the original beams used to record the grating will diffract from the structure into the direction of the other recording beam.

Coupled wave theory for thick gratings is used in photorefractive devices to analyze the efficiency with which the incident beam diffracts from the recorded grating structure. The evolution of the the reading beam (R) as it propagates through the grating, gradually becoming the diffracted beam (D), is a function of configuration parameters. In a refractive-index modulation based transmission hologram, the thickness of the grating (L) can be related to a parameter called the "Q" parameter where $Q = 2\pi\lambda L/n\Lambda^2$. Coupled wave theory defines a thick diffraction grating as systems in which $Q > 10$; for a standard case ($L = 50 - 100$ µm, $\lambda = 532$ nm, $n = 1.6$ and $\Lambda = 2$ µm), $Q \approx 25 - 50$, allowing the application of Kogelnik's theory to the majority of photorefractive polymer based devices.[2] Figure 1-26 illustrates the geometry of the system as related to this discussion.

While the full derivation of this analysis will be left to the original paper, the applicable results will be discussed here. The evolution of D resulting from Kogelnik's analysis of thick transmission gratings is[2]

$$D = -i\sqrt{c_R/c_D}\ e^{-\alpha L/c_R}\ e^{-i\xi}\ \frac{sin\sqrt{\nu^2-\xi^2}}{\sqrt{1-\xi^2\,/\,\nu^2}} \tag{1-49}$$

in which the terms c_R and c_D correspond to geometrical factors related to the tilt of the system. Defined as $c_R = \cos\theta_R$ and $c_D = \cos\theta_R - K\cos\varphi\,/k$, θ_R and φ are the angles between the sample normal and the reconstruction beam and grating vector, respectively. The two are equal for an unslanted grating in which both the reference and object beams are incident at equal and opposite angles with respect to the sample normal. The second term of (1-49) adjusts the magnitude of D by the attenuation of the beam intensity through film absorption, with α defining the absorption constant of the material. In the third term, ξ relates the losses due to absorption as well as reconstruction parameters.

$$\xi = \frac{L}{2}\left(\frac{\alpha}{c_R} - \frac{\alpha}{c_D} - i\frac{\vartheta}{c_D}\right) \tag{1-50}$$

$$\vartheta = \Delta\theta K\, sin(\varphi - \theta_R) - \Delta\lambda K^2/4\pi n \tag{1-51}$$

The term ϑ is called the dephasing constant and is used to probe the effect of wavelength and reading angle deviations ($\Delta\lambda$ and $\Delta\theta_R$, respectively) on D. In the case of no angular or wavelength offset, this contribution disappears. The final term in (1-49) describes the overall behavior of the coupling with respect to the distance traveled through the grating in which $\nu = \kappa L/\sqrt{c_R c_D}$ and the coupling constant ($\kappa = (\pi\Delta n)/\lambda - (i\Delta\alpha/2)$) describes the coupling between R and D. The terms Δn and $\Delta\alpha$ are the refractive index and absorption modulation

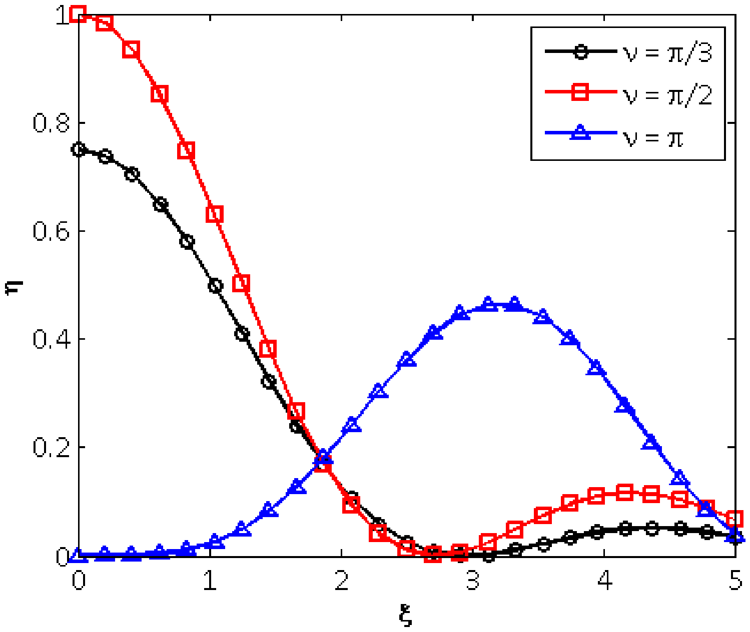

Figure 1-27: Diffraction efficiency as a function of ξ for $\nu = \pi/3$ (circles), $\nu = \pi/2$ (squares) and $\nu = \pi$ (triangles).

terms, respectively. In the case of photorefractive polymers, $\Delta\alpha$ is very small and can be omitted from the analysis, leading to

$$\nu = \frac{\pi \Delta n L}{\lambda \sqrt{c_R c_D}} \tag{1-52}$$

As the efficiency with which R is diffracted into D is given by

$$\eta = \frac{|c_D|}{c_R} D D^* \tag{1-53}$$

the maximum diffraction efficiency occurs when $\nu = \pi/2$, or when $2\Delta n/\lambda = \sqrt{c_R c_D}/L$. Figure 1-27 illustrates the relationship between η and ξ through (1-49) and (1-53). This analysis is performed for a range of ν values that can be experimentally obtained by changing the index modulation, sample thickness, reading wavelength or reading geometry. In the case of ν less than $\pi/2$, the minima of the function shifts to longer ξ while in the case of $\nu = \pi$, the maximum diffraction efficiency is realized only for higher values of ξ.

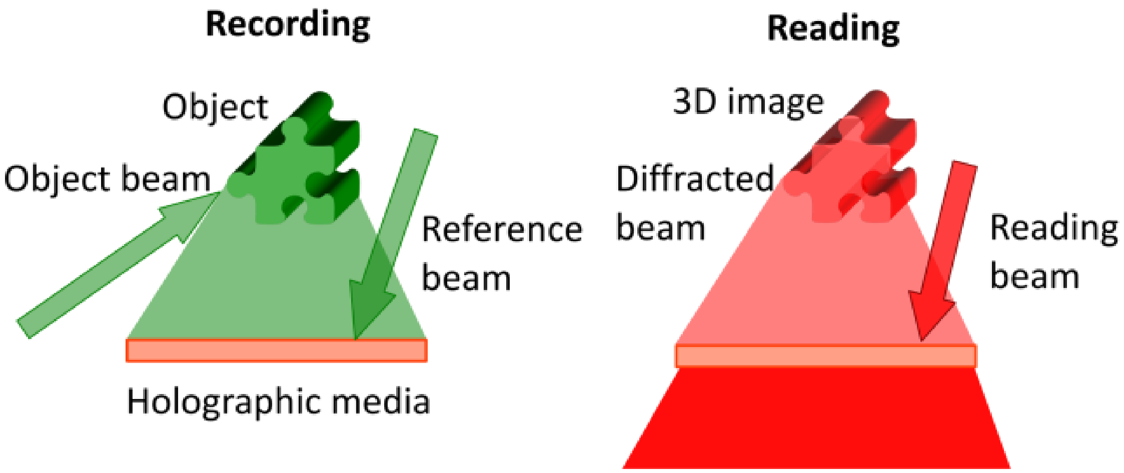

Figure 1-28: Recording and reading geometries for real object holography.

Once the material and system geometry parameters have been optimized to maximize the diffraction efficiency, the holographic grating can then be recorded. Figure 1-28 illustrates the recording and reading geometries of real object holography, or a system in which the information in the object beam is imparted directly from a real object. The object beam is imprinted with the wavefront amplitude and phase information by reflecting if off of the subject of interest onto the photorefractive film. There it interferes with the mutually coherent reference beam, producing the fringe pattern to be recorded. To read the hologram, a reading beam reproducing the wavefront of the reference beam is diffracted by the index grating of the film, recreating the wavefront of the beam as though it were being reflected from the object.[120]

Computer generated models displayed on a spatial light modulator (SLM) provide an alternative to using real objects or scenes. The SLM, in this case, acts as the object, modulating the amplitude and/or phase of the object beam upon reflection or transmission. In the case of both amplitude and phase modulation, the computer generated object beam can approximate the real object beam as closely as the resolution of the SLM allows. In the case of amplitude only or phase-only modulation, the information contained in the object beam is reduced to a two-

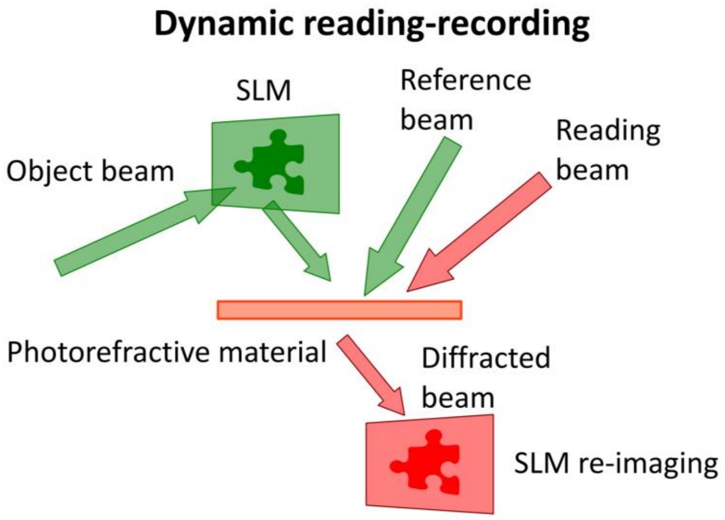

Figure 1-29: Illustration of dynamic holographic reading and recording of a two dimensional image.

dimensional representation of the object, taken from a single viewing perspective, or “view”. This view can be directly recorded into the photorefractive device, creating a hologram of a two-dimensional object, illustrated in Figure 1-29. Alternatively, the three-dimensionality of the reconstructed scene can be approximated through the use of holographic stereography. In these types of systems, the object information is created based on a three-dimensional computer model or series of images of a real object taken from various viewpoints or perspectives. These perspectives are optically multiplexed onto different regions of the recording medium, recording the necessary angles and viewpoints for each film location across the entire display. Reconstruction of the image is performed in the same manner as in real object holography.

Holographic displays have intrigued scientists and the public alike with vivid three-dimensional images appearing to hover in mid-air. Applications range from artistic installments and eye-catching advertisement platforms to holographic television and displays. The flexibility of the photorefractive polymer system lends itself to large screen sizes and response characteristics tunable for each proposed application. Holographic recording and display requires a photorefractive film that has a high sensitivity and fast response time in order to record the wavefront as quickly and efficiently as possible. While the device must be optimized to exhibit high diffraction efficiency for bright image reconstruction, the photorefractive gain is not an important parameter in these applications. The performance of the PR material can be adjusted to match the given application. For video rate displays, short image persistence and pulsed laser response are key metrics. For static or slowly changing applications, image brightness and long persistence are the critical metrics.

Long persistence holograms are useful in cases where the same image or scene will be viewed for minutes to hours. Increasing the glass transition temperature of the photorefractive compound is one way to achieve high-efficiency systems that are stable in this time frame, requiring that the temperature of the media be raised above this temperature for recording and then subsequently cooled. The application of an external field after cooling is also not required to maintain the overall alignment of the chromophores. Li and Wang recorded diffraction grating persistence times of more than two hours in their unplasticized system based on a TPD: carbazole: DCST functionalized matrix doped with 7-DCST. With a T_g of 43 °C, local preheating of the film for 1.5 minutes using a CO_2 laser allowed them to update the film, achieving a peak diffraction efficiency of 92 % and higher than 72 % over the first 5 minutes.[111] Tay et al. recorded a holographic stereogram into a 4”×4” plasticized PATPD-CAAN:FDCST:ECZ film with a room temperature T_g. They were able to achieve both fast recording and hours of persistence by writing the hogels at 9 kV and then dropping the voltage to 4 kV in a process called “voltage kick-off.” The higher writing electric field enhances the recording dynamics of the composite, while the lower reading voltage maintains the grating without contributing as significantly to its decay. This process allowed them to increase the

Figure 1-30: Multi color holographic stereograms. Reproduced from [5], with permission from NPG.

diffraction efficiency from the 1.5 % they obtained by recording for 0.5 seconds at 4 kV to 55 % for the same recording time at 9 kV.[95]

For applications in which high-speed updating is necessary, the ability to quickly record and rewrite the grating is necessary. Tsutsumi et al. fabricated a 1.8 cm^2 area device based on PVK:7-DCST:CzEPA:TNF. This film exhibited 68 % diffraction efficiency at 45 V/µm and a weighted average rise time of 59 ms (1.5 W/cm^2 writing power). They recorded real object holograms as well as a two dimensional image using an SLM displaying an image, requiring 1 second per exposure.[30] Tsujimura et al. also recorded a two dimensional image displayed by an SLM into a PDAS:FDCST:ECZ:PCBM film. While the steady-state diffraction efficiency of their system only reached 35 % at 45 V/µm, they were able refresh their image in only 50 ms.[98]

Blanche et al. continued the work by Tay et al. adding a sensitizer to the PATPD-CAAN composition (PATPD-CAAN:FDCST:ECZ:PCBM) and implementing a 6 ns pulsed laser which delivered 200 mJ per pulse at a repetition rate of 50 Hz. Each hogel was written with a single pulse, shortening the writing time of the entire 4”×4” display to 2 seconds. This high-speed writing enabled the integration of a “telepresence” system, taking a live feed from 16 camera views of a speaker and transmitting it to the holographic printer. Additionally, multi-color reconstruction was performed by angularly multiplexing separate holograms written for each wavelength, the results of which are shown in Figure 1-30.[5, 121] Recent developments in their work have been the exhibition of a 12”×12” active area device, three-color holograms with a color gamut exceeding that of the standard HDTV and display brightness of 2,500 cd/m^2. [122]

Computer generated holograms (CGHs) have recently been written in a photorefractive polymer device by Jolly et al. Instead of holographically recording the necessary views as in holographic stereography, CGHs are calculated by computationally interfering an object and reference beam and recording the resulting fringe pattern directly. This is performed through a process known as direct fringe writing in which the fringes are displayed on an SLM and imaged onto the film where the intensity distribution is recorded. The benefit to this method is that instead of approximating the object wavefront by a series of perspectives, the CGH can directly reproduce the object wavefront within the limitations of the recording resolution. To display the grating with sufficient resolution to capture an analog approximation to the phase grating requires many pixels on the SLM and demagnification of its image onto the PR film to achieve the necessary diffraction angles. The limited number of available pixels requires a balance between the fidelity of the grating and the extent of the image.[6]

2 EXPERIMENTAL TECHNIQUES

2.1 Introduction

While the end goal of photorefractive polymeric media development is efficient diffraction from an index grating, better understanding of the relationship between the individual compounds and characteristics of the device performance can help in the development of faster, more sensitive polymer composites. It is therefore important to measure not only the efficiency with which a probe beam is diffracted (four-wave mixing) or amplified (two-beam coupling) but also more basic phenomena such as photogeneration efficiency and charge carrier mobility. This section describes the measurement layout and analysis of the methods used in this research to test these parameters.

2.2 Birefringence/Electro-Optic Properties

2.2.1 Transmission Ellipsometry

Transmission ellipsometry is one of the simplest methods by which to measure electric-field induced birefringence (defined as $|n_p - n_s|$) in photorefractive polymer devices. As discussed in Section 1.4.3, the orientation of chromophores in response to an externally applied electric field across the sample causes a change in the refractive index with respect to that of the unpoled bulk polymer. Additionally, in the standard use case in which the sample plane is tilted with respect to the optical beam, there is a difference in the refractive index that in-plane and out-of-plane polarizations will experience leading to a bulk birefringence. Figure 2-1 is an illustration of the index ellipsoid of this system under various poling conditions indicated by the order parameter, *S*. Without any applied field, *S* = 0, the chromophores are randomly oriented, and the values of the ordinary and extraordinary refractive index (n_o and n_e respectively) are equal

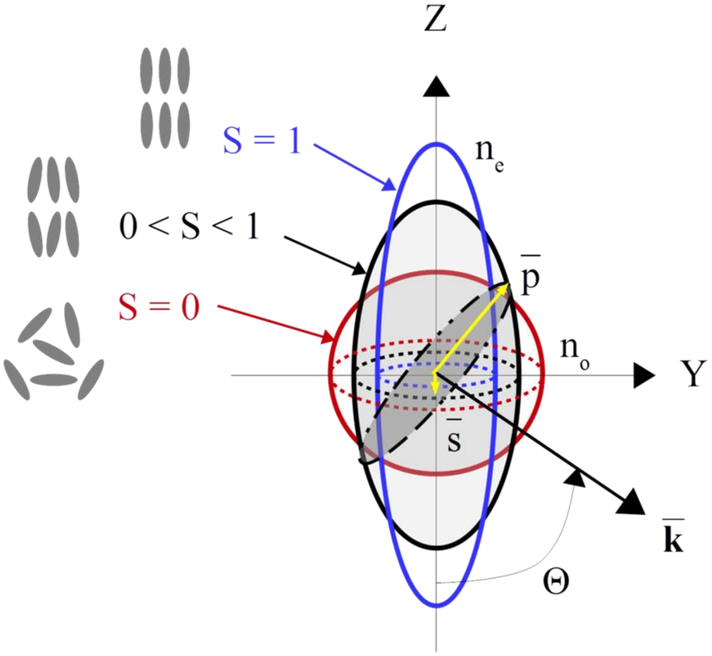

Figure 2-1: Refractive index ellipsoid. The *Y-Z* plane is the plane of incidence in which the propagation vector ($\bar{k}$) lies at angle *θ* with respect to the sample normal. *S* is the molecular order parameter and increases with increasing applied electric field. The *p*-polarization component of the propagating field lies in the *Y-Z* plane and the *s*-polarization component lies out of the plane of the page.

leading to no birefringence for any propagation direction. As a bias is applied along the *Z* axis, the ellipsoid stretches along that axis, increasing n_e while simultaneously decreasing n_o in the region $0 < S < 1$. The refractive index that the *s*- and *p*-polarization components of the propagating beam experience are dependent on the angle of propagation with respect to the sample normal, θ. For an untilted sample ($\theta = 0$), the two components are equal, regardless of degree of order. Increasing the tilt angle increases the refractive index for the *p*-polarization ($n_p(\theta)$) while the *s*-polarization refractive index ($n_s(\theta)$) remains constant and described by

$$n_s(\theta) = n_o \tag{2-1}$$

$$n_p(\theta) = \frac{cos^2\,\theta}{n_o^2} + \frac{sin^2\,\theta}{n_e^2} \tag{2-2}$$

The case in which $S = 1$ indicates that all of the chromophores are completely aligned along the field direction. Poled molecular systems have fundamental limits on the degree of order that is achievable due to intermolecular forces so the devices under test function within the $0 < S < 1$ range.[123]

In this test system, the optical probe is chosen such that it is or can be linearly polarized and the wavelength is in a region of low absorption. In the case of the composites studied here, a weak 1550 nm laser diode source was used with an associated configuration shown in Figure 2-2. The probe beam is polarized using a linear polarizer and the electric-field incident on the sample plane is oriented at 45° with respect to the vertical axis, creating equal degrees of *s*- and *p*-polarization states within the frame of reference of the measurements. The photorefractive device is placed at an angle θ with respect to the vertical axis, imparting an applied electric field component orthogonal to the direction of propagation. A Soleil-Babinet compensator negates any sample birefringence while no external field is applied and is followed by another linear polarizer, referred to as the analyzer with the transmission axis oriented perpendicularly to the initial polarization. The final component is a photodetector which is used to record the intensity of the probe beam. Initially, the polarization of the probe beam is perpendicular to the transmission axis of the analyzer, resulting in zero intensity at the detector plane. Upon the application of a bias across the thickness of the sample, the index of refraction along the horizontal and vertical film axes change, creating a birefringence within the bulk, and imparting a phase shift between the two incident polarizations. The effect of this phase shift is to rotate the linear polarization of the probe beam by an angle $\Delta\delta$ for sample thickness d and probe internal angle of incidence $\bar{\theta}$[124]

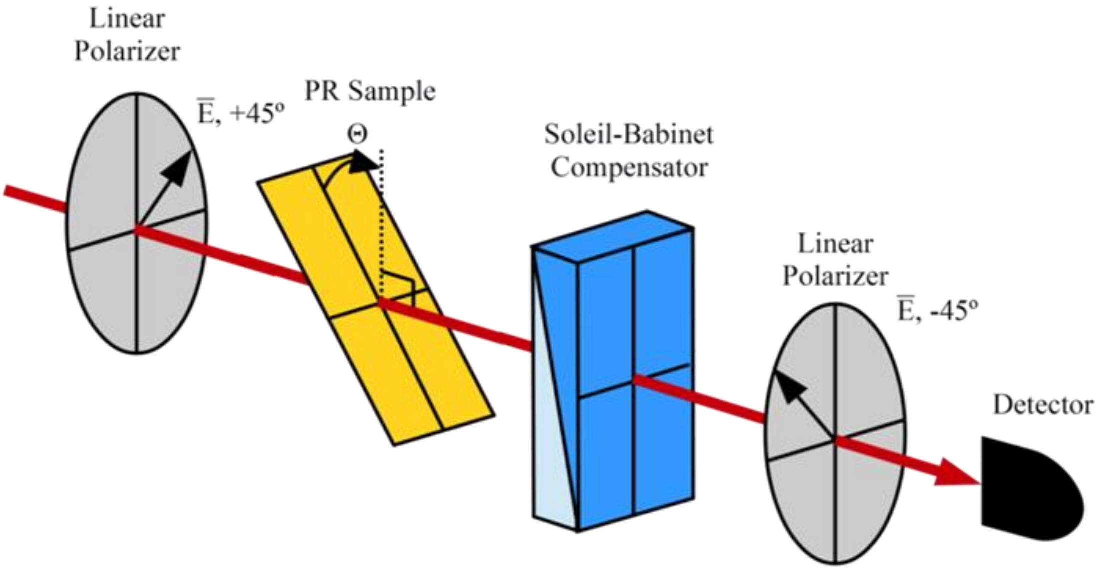

Figure 2-2: Transmission ellipsometry measurement system.

$$\Delta\delta = \frac{2\pi}{\lambda}\left(n_p - n_s\right)\frac{d}{\cos\bar{\theta}} \tag{2-3}$$

which causes some of the probe beam to be transmitted through the analyzer. The transmitted intensity (I) is recorded and can be related to the refractive index modulation through

$$I = \sin^2\Delta\delta = \sin^2\left(\frac{2\pi}{\lambda}\left(n_p - n_s\right)\frac{d}{\cos\bar{\theta}}\right) \tag{2-4}$$

This analysis makes the assumption that the electro-optic contribution is negligible in comparison to the orientational birefringence contribution which is generally valid in these low T_g systems. These measurements can be repeated as a function of the applied electric field or wavelength.

2.2.2 Electric Field Induced Second Harmonic Generation

Electric field induced second harmonic generation (EFISHG) is a standard optical characterization technique for nonlinear optical materials and their response to external stimuli.[125] It is a third-order nonlinear optical process in which one of the three input frequencies is a DC electric field.[126] This externally applied field affects the macroscopic order of the system, namely by orienting the polar chromophores and creating a bulk asymmetry, required for a second order optical response. The nonlinear optical polarizability ($P_i^{2\omega}$) of such a system can be written

$$P_i^{2\omega} = \chi_{ijkl}^{(3)}(-2\omega;\omega,\omega,0)E_j^{\omega}E_k^{\omega}E_l^{0} \tag{2-5}$$

where E_j^{ω} and E_k^{ω} are the incident optical fields of frequency ω, E_l^{0} is the externally applied DC electric field and $\chi_{ijkl}^{(3)}(-2\omega;\omega,\omega,0)$ is the third order susceptibility of the bulk system for EFISHG. In the case of PR polymers, upon the application of the external field, the permanent dipole moment of the chromophore causes the molecules to rotate and partially align to the field. The bulk nonlinear polarizability in this case can be rewritten in a more convenient manner with an electric field dependent second order polarizability replacing the third order polarizability as

$$\begin{aligned} P_i^{2\omega} &= \chi_{ijk}^{(2)}(-2\omega;\omega,\omega)(E^0)\,E_j^{\omega}E_k^{\omega};\quad \chi_{ijk}^{(2)}(-2\omega;\omega,\omega)(E^0) \\ &= \chi_{ijkl}^{(3)}(-2\omega;\omega,\omega,0)E_l^{0} \end{aligned} \tag{2-6}$$

Typical chromophores exhibit cylindrical symmetry with hyperpolarizability confined to the long axis of symmetry along which the dipole is oriented. This results in the tensor elements of the polarizability only being significant in the directions perpendicular or parallel to the poling field. As the purpose of the current study was to analyze the relative field dependence of the orientation of the chromophores subject to a spatially varying bias, only the general form of the second order polarizability is necessary for this analysis.

The optical intensity of the generated second harmonic ($I(2\omega)$) is related to $\chi^{(2)}$, E^0 and the incident optical power ($I(\omega)$) through

$$I(2\omega) \propto \left(\chi^{(2)}\right)^2 I^2(\omega) \propto (E^0)^2 I^2(\omega) \tag{2-7}$$

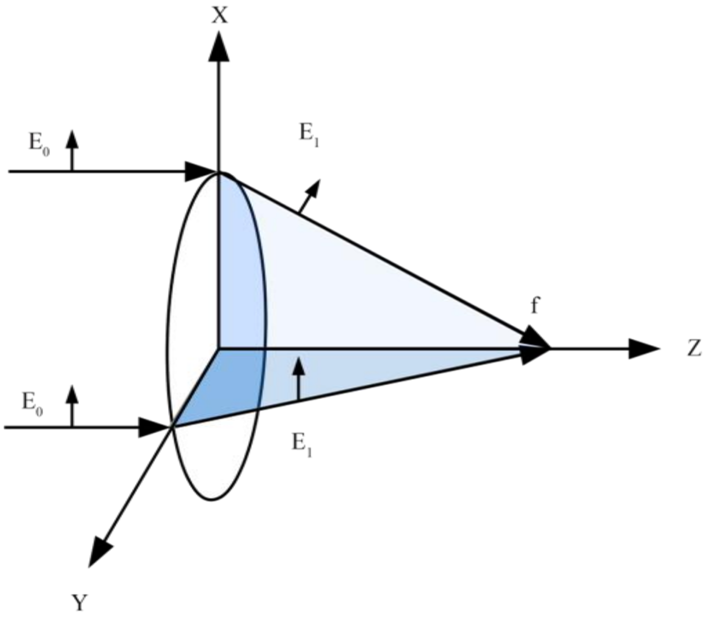

Figure 2-3: Linearly polarized light focused by a high NA aplanatic lens.

This quadratic dependence of the generated second harmonic optical intensity on the degree of molecular orientation translates into a similar quadratic relationship to the applied electric field.

The magnitude of the second-order susceptibility for this type of poled polymer system is relatively small, requiring high fundamental frequency intensity to produce a significant signal at the second harmonic frequency. Generally speaking, this type of system is composed of a high peak power pulsed laser, linear polarization optics to control the incident and measured polarization, a lens to concentrate the beam onto the sample and a filter prior to a detector to limit the measurement to only the second harmonic of the incident frequency. The system employed in this research was a near-IR laser scanning microscope (described in detail by Kieu, et. al.[127]) enabling high-resolution probing of a large area as well as measurements through the depth of the device.

The fundamental illumination was provided by an unpolarized 1560 nm, 190 fs pulse width, 75 MHz repetition rate fiber laser with 50 mW average power. A linear polarizer inserted

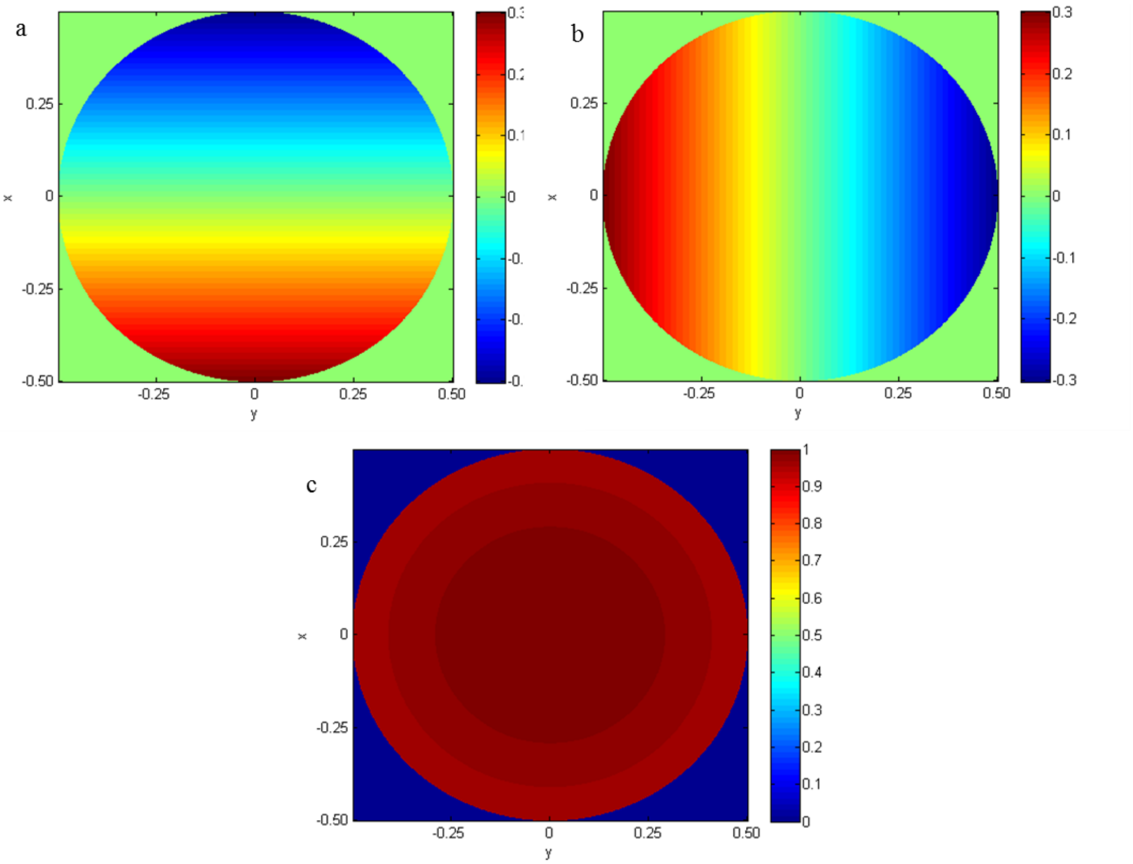

Figure 2-4: (a) *x*, (b) *y*, (c) *z* (axial) vector directions of the propagating electric field at the exit pupil of the microscope objective.

into the collimated fiber laser output linearly polarized the excitation source and resulted in 25 mW average power at the measurement plane. The orientation of the linear polarization was aligned along the direction of chromophore orientation (parallel to the applied electric field) using a half wave plate prior to the scan mirror. The pulses were Gaussian in the time domain with an estimated peak power of 1.54 kW and energy per pulse of 0.333 nJ.[128] The microscope objective in this system was a NewFocus 0.5 NA aspheric lens, resulting in a focused beam waist of

$$\omega_0 = {}^{\lambda}\!/_{n*\pi*NA} = {}^{1.56\mu m}\!/_{1.65*\pi*0.5} = 0.602\mu m \tag{2-8}$$

and for a Gaussian beam, this results in a peak power intensity of 1.06 ×10^{12} W/cm^2.

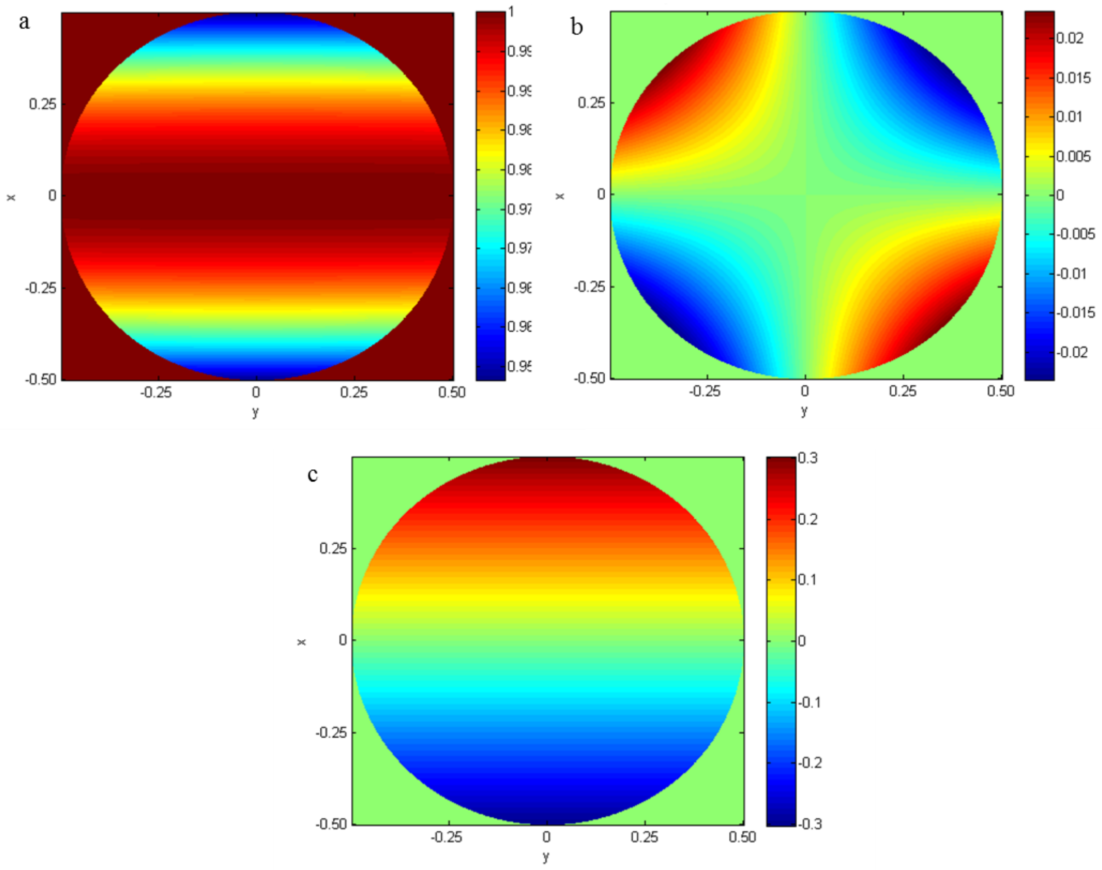

Figure 2-5: (a) *x*, (b) *y*, (c) *z* (axial) normalized polarization component magnitudes at the exit pupil of the microscope objective.

In a focusing system, the refractive device imparts polarization changes to the beam profile with respect to the incident wavefront.[124] In poled molecule systems, the magnitude of the second harmonic response is dependent on the alignment of the excitation polarization to the molecular orientation. For sufficiently high NA systems, this polarization effect must be taken into account in analyzing the measurement results. In the case of an aplanatic, well corrected system, such as an aspheric objective, this effect can be quantified using a geometry based ray bending analysis, disregarding the effects of aberration and losses as illustrated in Figure 2-3.[129] For the 0.5 NA objective used in this measurement and a collimated incident beam propagating in the z direction defined as a plane wave $\sigma_0 = (0,0,1)$, the x, y, and z components of the normalized ray unit vectors across the aperture after refraction are $\sigma_1 = (\sigma_x, \sigma_y, \sigma_z\ )$. The polarization components at the entrance and exit pupil of the lens are given by $E_0 = (1{,}0{,}0)$ (assumes linear polarization) and $E_1 = (1 - \frac{\sigma_x^2}{1+\sigma_z}, \frac{-\sigma_x^2\sigma_y^2}{1+\sigma_z}, -\sigma_x)$ respectively. The maximum extent of the aperture is determined through the normalization of the direction vector and is equal to the NA of the objective in the material (0.5/1.65 in this case). Figure 2-4 illustrates the output field vector directions $\sigma_1 = (\sigma_x, \sigma_y, \sigma_z)$ where the x vector (a) remains constant along any horizontal line, the *y* vector components (b) remain constant along any vertical angular line and the *z* component (c) exhibits radial symmetry.

Figure 2-5 shows the polarization components across the exit pupil of the microscope objective. Propagation of these fields to the focal plane of the lens would be required to know the polarization distribution at the sample plane. In our case, however, the objective is not being used in a standard microscope configuration to image where the pump illumination interacts with the material and generates 2nd and 3rd harmonic photons. This generation propagates in the same direction as the incident light, so only the energy that is reflected from subsequent surfaces is collected back through the microscope objective, where it is separated into 2nd and 3rd harmonic channels using filters and the intensity of the total signals are detected via photomultiplier tubes. The beam is rastered across the region of interest by an *x*-*y* scan mirror system. Due to this signal integration over the entire field of view of the microscope the polarization effect can also be integrated across the field regardless of focal position. Additionally, the total *E*-field energy density is a linear superposition of the individual components $|E_x|^2 + \left|E_y\right|^2 + |E_z|^2$. The magnitude of the E-field integrated across the aperture is $|E_x|^2 : \left|E_y\right|^2 : |E_z|^2$; 0.9819: 7.1467e-05: 0.0181. The *x* polarization in the illuminating beam is 1.3739e+04 times larger than the y polarization, indicating that no accounting for *y* polarization of the incident beam is

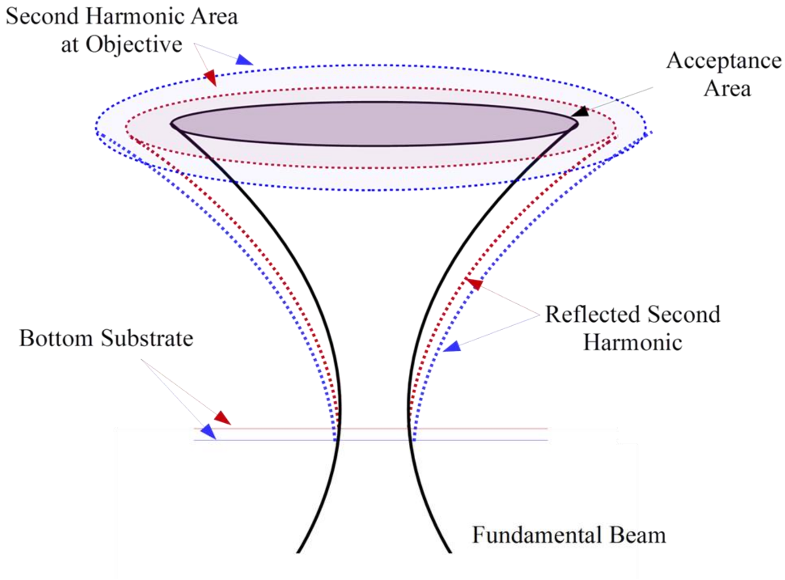

Figure 2-6: Diagram of reflection based SHG collection. Red lines indicate that the bottom substrate is below the focus of the beam, as is the case when probing the volume of the sample. The blue lines are a more extreme case.

necessary in further analysis. The z component accounts for nearly 2 % of the total energy density of the illumination but taking into account the $I(2\omega) \propto I^2(\omega)$ relation, the z polarization contribution to the measurements are negligible. These results indicate that an NA of 0.5 does not cause significant axial polarization and does not require consideration in the analysis of data collected through the use of this multi-photon microscope system.

Since this system functions in reflection, another effect to consider in the analysis of data taken at various vertical steps through the height of the device is the difference in the percent of light collected as a function of lateral position of the focus. Figure 2-6 illustrates the geometry of the collection of the second harmonic generated within the sample volume. The location of the second harmonic generation is confined within a few microns of the focal point of the microscope objective. Once it is generated, it continues in the same direction as the fundamental until it encounters the bottom substrate of the device under test. There, a fraction of the intensity is reflected and returns toward the microscope objective, now acting as a collection optic. When the focal point of the fundamental is located at the plane of the substrate, all of the reflected SHG is collected, but as the sample moves down to probe different depths, the beam is clipped at the collection optic. The Gaussian beam size at the collection optic is given by

$$\omega = \omega_0 \sqrt{1 + \left(2 * \Delta z + f \big/ z_R\right)^2} \tag{2-9}$$

where ω_0 is the focused beam size, z_R is the Rayleigh length, and Δz is the displacement of the focal point from the substrate. The power collected through the 4mm radius objective as a function of Δz is

$$P(\Delta z) = 1 - e^{-2*(4mm)^2/\omega^2(\Delta z)} \tag{2-10}$$

Across the depth of the sample (60 µm), the power collected drops linearly but only decreases by 1 % at the maximum measurement range. This indicates that the SHG collection dependence on focal location is negligible for a 0.5 NA system.

2.2.3 Four-Wave Mixing

Four-wave mixing (FWM) is the method by which the induced refractive index grating's diffraction ability is measured. This system is composed of writing and reference beams, generally with the same irradiance, and a separate probe, or reading beam which is used to interrogate the diffraction grating as shown in Figure 2-7. The writing beams, depicted in blue, are *s*-polarized to reduce energy transfer through gain and the probe beam is *p*-polarized to align with the direction of modulated birefringence. The irradiance of the probe beam is much lower than that of the writing beams so that it does not erase the grating during the measurement. Measurements in which the probe beam is the same wavelength as the writing beams, or degenerate four-wave mixing (DFWM) measurements, require precise back-propagation of the probe beam along one of the writing beam paths in order to meet the Bragg conditions for thick holograms. For efficient diffraction from a volume grating, the angular deviation ($\Delta\theta_R$) is restricted to

$$\Delta\theta_R \approx {}^{\Lambda}/_{(2L)^2} \tag{2-11}$$

which in the case of a 100 µm thick polymer and 2µm grating period is $\Delta\theta_R \approx 0.6°$. Non-degenerate four-wave mixing (NDFWM) incorporates a probe beam which is of a different wavelength ($\lambda_R{}'$) than the writing beams. In this configuration, the probe beam Bragg angle will be shifted ($\theta_R{}'$) from that of the writing beams due to the chromatic dispersion of the diffraction as related in (2-12) where Ψ is the tilt angle of the bisector of the writing beams with respect to the sample normal.

$$\frac{\lambda_R}{sin(\theta_R - \Psi)} = 2n\Lambda = \frac{\lambda_R{}'}{sin(\theta_R' - \Psi)} \tag{2-12}$$

The efficiency with which the probe beam is diffracted is the parameter of interest in FWM measurements and is obtained by recording the intensities of the transmitted (I_T) and diffracted (I_D) probe beams. The internal diffraction efficiency is defined as the ratio of the diffracted power of the probe beam to the sum of the diffracted and transmitted powers of the probe beam. This definition of diffraction efficiency does not take into account any losses due to scattering, absorption and reflection and can reach 100 % for some systems. An alternate definition, the external diffraction efficiency, takes these losses into account and is defined as the ratio of I_D to the initial intensity of the probe beam (I_R). This value is generally around 60 % to 70 %.

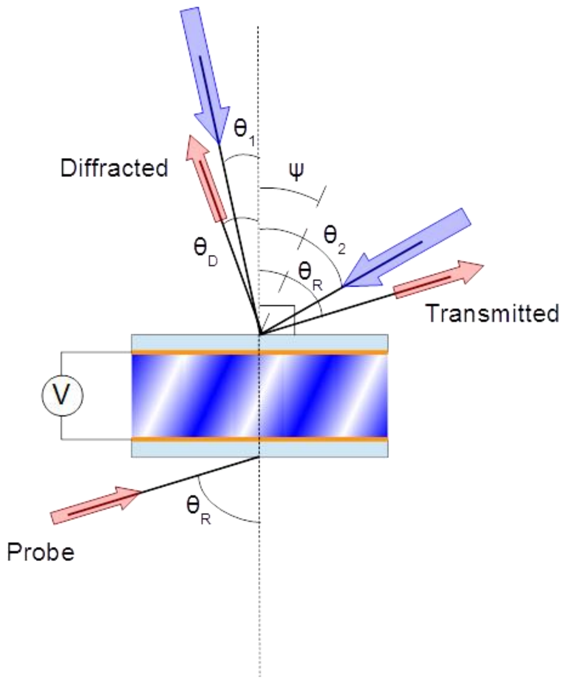

Figure 2-7: Illustration of non-degenerate four wave mixing geometry in which the probe beam is of a different wavelength than the writing beams.

The transients of FWM measurements are used in order to investigate parameters such as the photorefractive rise and decay times. While FWM does not provide proof of photorefractivity as the probe beam does not require a phase shift to diffract, it does characterize the holographic nature of the film and its applicability as a recording media. Transient and steady state FWM measurements are used to probe the response of the grating under various experimental conditions such as writing intensity and contrast, electric field, and temperature.

The relationship between the diffraction efficiency of a minimally lossy dielectric volume grating and the various physical parameters has been developed by Kogelnik[2] and takes the form

$$\eta = sin^2\left(\frac{\sqrt{\nu^2+\xi^2}}{1+{\xi^2}/{\nu^2}}\right) \tag{2-13}$$

in which ν and ξ contain the material parameters and measurement configuration and are defined in (2-14) and (2-15) where Λ is the fringe spacing, d is the grating thickness and the angle terms are defined in Figure 2-7.

$$\nu = \frac{\pi\,\Delta n\,d}{\lambda\sqrt{c_R c_S}};\ c_R = cos\,\theta_R\,;\ c_S = cos\,\theta_R + \frac{\lambda}{n\Lambda} sin(\Psi) \tag{2-14}$$

$$\xi = \frac{\vartheta d}{2c_S} \tag{2-15}$$

ϑ is a dephasing parameter containing the deviation from the recording wavelength (Δλ) and angle ($\Delta\theta_R$)

$$\vartheta = \Delta\theta_R \frac{2\pi}{\Lambda} cos(\Psi - \theta_R) - \Delta\lambda \frac{\pi}{n\Lambda^2} \tag{2-16}$$

The Δn term in (2-14) is a sum of the contributions from the electro-optic response ((1-41) and (1-42)) and from the orientational enhancement of the birefringence ((1-46) and (1-47)) with variables defined in Section 1.4.3:

$$\begin{gathered}\Delta n_s = \frac{4\pi N}{15n}(B-D)E_0|E_{SC}|\,cos\,\varphi \\ \begin{aligned}\Delta n_p = \frac{4\pi N}{15n}E_0|E_{SC}|\big[&(B-D)\,cos\,\varphi\,cos\,\alpha_1\,cos\,\alpha_2 \\ &+ (3B+2D)\,cos\,\varphi\,sin\,\alpha_1\,sin\,\alpha_2 \\ &+ \left(B + {}^{3D}\!/_{2}\right) sin\,\varphi\,sin(\alpha_1+\alpha_2)\big]\end{aligned} \\ B = \frac{2\mu^*\beta^*_{ZZZ}}{k_B T}; D = \frac{\Delta\alpha}{3}\left(\frac{\mu^*}{k_B T}\right)^2\end{gathered} \tag{2-17}$$

The electric field dependence can be seen to relate to the diffraction efficiency as $\eta \propto \sin^2(CE_0E_{SC})$ in which C contains all of the other relevant parameters. If the approximation that the majority of the refractive index modulation response is due to the orientational enhancement, (2-17) can be simplified to

$$\Delta n_s = \frac{4\pi N}{15n}\frac{\Delta\alpha}{3}\left(\frac{\mu^*}{k_B T}\right)^2 E_0|E_{SC}|\,cos\,\varphi \tag{2-18}$$

$$\Delta n_p = \frac{4\pi N}{15n}\frac{\Delta\alpha}{3}\left(\frac{\mu^*}{k_B T}\right)^2 E_0|E_{SC}|\big[\cos\varphi\cos\alpha_1\cos\alpha_2 \\ + 2\cos\varphi\sin\alpha_1\sin\alpha_2 + {}^3\!/_2\sin\varphi\sin(\alpha_1+\alpha_2)\big]$$

In this case, the temperature dependence of the diffraction efficiency takes the form $\eta \propto (E_{SC}/T^2)$, valid for conditions under which the oriented gas model is valid. The space charge field is temperature dependent through parameters such as the mobility and trapping/detrapping rates.

From (1-12), the contrast of the illuminating fringe pattern is linearly related to the magnitude of the space charge field, indicating a quadratic dependence of the diffraction efficiency on the intensity modulation. Likewise, in a device operating above the T_g, or not limited by re-orientation speed of the chromophores, the rate of photorefractive response is determined by the rate of the space-charge field formation. In this case, the diffraction efficiency is $\eta \propto C''E_{SC}^2$ with $\frac{d\eta}{dt}$ linearly related to E_{SC} and therefore the illumination intensity as well.

The photorefractive rise and decay response times are often parameterized by fitting the transient diffraction efficiency curves to (2-13), in which the refractive index modulation is expressed as the product of two bi-exponentials, one describing the photorefractive rise and one the decay.

$$\Delta n \propto \left[1 - m_1 e^{-t/\tau_1} - (1-m_1)e^{-t/\tau_2}\right] \times \left[m_2 e^{-t/\tau_3} + (1-m_2)e^{-t/\tau_4}\right] \tag{2-19}$$

Each bi-exponential has two terms, τ_1 and τ_3 describing the fast time response of the rise and decay, and τ_2 and τ_4 describing the slow time response, respectively. The weighting factors, m_1 and m_2 relate the fast and slow rates within the rise or decay and are proportional to the weighted photorefractive rise and decay response time (τ_{rise}, τ_{decay}) through

$$\tau_{rise} = m_1\tau_1 + (1-m_1)\tau_2;\;\; \tau_{decay} = m_2\tau_3 + (1-2)\tau_4 \tag{2-20}$$

2.3 Photorefractive Device Preparation

The process for preparing photorefractive devices for test is as follows:

1. Etch or purchase transparent ITO on glass electrodes.
2. Make the photorefractive polymer blend, including drying the PATPD and purifying the ECZ if either of these compounds are used.
3. Fabricate the devices using the melt-processing technique.

2.3.1 ITO Etching for standard electrodes

We provide the basic procedure for etching ITO electrodes with centimeter scale features. First, cut 1” slides of transparent ITO coated glass (Colorado Concept Coatings, LLC, 60 Ohm ITO coated float glass used here). Cover the ITO coated side with a similarly sized piece of Parafilm, applying pressure to ensure the removal of air bubbles. Briefly heat the film with a heat gun to promote adhesion which is complete when the Parafilm becomes uniformly clear. After the film is cool use a mask in the desired electrode shape to cut away Parafilm from the area to be etched. It is important that the Parafilm be cut in a smooth curve with no rough edges. These will translate to regions of high electric field concentration and result in the dielectric breakdown of the devices.

Make a solution of 10.282 grams $FeCl_3$ (hexahydrate is fine) in 200 mL of 12 M HCl in a 400 mL beaker. Heat to near boiling (~160 °C), stirring with a magnetic stirrer constantly at about 200 rpm. Be careful not to overheat or heat without sufficiently stirring as a large gas bubble will form on the bottom of the beaker and when it pops, acid will spill outside the container. Dip the prepared slides into the acid and agitate slowly. Bubbles will form at the ITO surface; keep the slides in the etching solution until bubbling subsides, (approximately 15 seconds) indicating complete etching.

Remove slides from the etching solution and rinse immediately with copious amounts of DI water to remove residual etching solution. Dry the slides under a stream of air before stripping off the remaining Parafilm coating. The film should remove cleanly unless overheated with the heat gun, in which case it will tear.

Sonicate the slides in hexanes for 15 minutes followed by sonication twice for 15 minutes in DI water, once more with Ethanol then store in Ethanol. Alternatively, if substrates are to be used immediately, after removing the remaining Parafilm, they may be sonicated in hexanes and used.

2.3.2 Lithographic Electrode Fabrication for Coplanar Electrodes

Before preparing the slides for etching, it is best to make the developer solution and let it sit to remove bubbles. This solution consists of a ratio of 1:5 Microposit MF-321 developer to DI water, respectively; the dilution of the developer increases the time required to develop, but also increases the timing error tolerance. Cut transparent ITO coated glass (Colorado Concept Coatings, LLC, 60 Ohm ITO coated float glass used here) into 1” square slides and clean using acetone and isopropanol. This is followed by O_2 plasma cleaning for one minute. Then spin-coat the positive photoresist Microposit S1813 (Shipley) onto the ITO covered surface of the slide. Apply enough resist using a syringe and 0.2µm filter to completely cover the slide, spin at 500 RPM for five seconds, and then at 5000 RPM for 30 seconds. This will produce a film approximately 1.25 µm thick. Heat on the hotplate at 115 °C for 60 seconds to soft bake.

The chrome-on-glass mask was custom designed and purchased from Microtronics, Inc. The mask is aligned to the exposure system (contact lithography) and exposed with a radiant fluence of 150 mJ/cm^2 corresponding to 20 seconds at an irradiance of 7.5 mW/cm^2. Submerge the exposed slide in the developer solution and agitate slowly until the removal of the exposed photoresist is complete (resist is red). Rinse well with DI water to remove all developer. No hard bake is necessary in this procedure.

Prepare a solution of 4:1 hydrochloric acid and DI water in a large beaker. Immerse the slide and slowly agitate, etching for 2.5 minutes. Rinse well with DI water. Check the conductivity of the exposed areas and continue etching if necessary until no conductivity remains. Remove unexposed photoresist by agitating in acetone for approximately 60 seconds. The width of the electrodes ranges from 5 to 100 µm, so while these times are appropriate for the 10 µm features used in the following studies, optimization will be necessary for different sizes.

2.3.3 PATPD Drying

The polymer host, PATPD is mildly hydrophilic and over time will absorb moisture from the atmosphere. This causes increased probability of dielectric breakdown in samples. Place about 200 mg of the powder in a 20 mL vial and dry under vacuum at 100 °C for 10 hours (the lid will melt at this temperature) – wrap in foil to keep clean and set aside. The final product will remain in clumps but is dry.

2.3.4 ECZ Purification Technique

Purification of ECZ, as received from Sigma-Aldrich, is necessary to obtain electronic grade material. The yield of this purification is on the order of 50 %. Slow crystallization is the key to increased yield and high purity. This process takes approximately a week but is not extremely time or skill intensive.

Measure 10 g of ECZ into a 400 mL beaker, add 200 mL of EtOH and sonicate the solution for 1 hour. Filter the solution using a syringe and 0.2 µm PTFE syringe filter(s) into another 400 mL beaker to remove any large particulate matter. Heat the solution to drive off EtOH until it reaches 75-100 mL. The original concentration is necessary to filter the solution effectively, but the next steps require a super-saturated solution. Remove from heat, label, and cover with parafilm. Place in the hood to crystallize overnight.

Carefully pour the EtOH solution into another 400 mL beaker and cover with parafilm. Label and store in the hood. Add 100 mL of EtOH to the beaker containing the crystals and cover with parafilm, sonicating for 1 hour to dissolve. Place in the hood and allow to crystallize overnight. Repeat as before, adding any further crystals from the remaining EtOH solution to the solution prior to sonication. Perform three crystallizations. Dry the final crystals in the oven under vacuum at 40 °C overnight to complete the purification. Crush finely and store in an airtight container.

2.3.5 Polymer Blend

Cleanliness is crucial here. All supplies must be exceptionally clean and dry to prevent contamination which leads to dielectric breakdown. Covering the workspace with foil helps as does keeping all beakers and supplies covered to prevent dust accumulation while processing. Significant activity in the lab also leads to dust in the material.

The components needed for this process are a polymer host, plasticizer, chromophore, and sensitizer. The sensitizer should be dissolved in a dilute solution in the appropriate solvent in order to facilitate the accurate measurement of sub-milligram quantities. PCBM is generally most soluble in toluene while the BBP (liquid at room temperature) is soluble in tetrahydrofuran (THF).

Measure all of the chemicals in the appropriate ratios into a 40mL beaker and add approximately 20 mL of solvent for 100 mg material unless directed otherwise. Typically the solvent will be toluene for PATPD/ECZ/PCBM based systems. Cover the beaker with foil and sonicate for approximately 20 minutes to ensure that all of the components are completely dissolved.

Filter the mixture using a syringe and 0.2 µm PTFE syringe filter into a watch glass. This is easiest if the watch glass is already situated in the oven before filling. A convenient stand to keep the watch glass upright can be made by forming foil into a two inch diameter ring and pressing the glass down on it until it is stable and flat. Cover with foil to keep out debris and contaminants while in the vacuum oven. Don’t seal too tightly so that the solvent can escape.

Heat the oven for 7-12 hours at 70 °C for toluene. If the solvent has a lower boiling point than Toluene, bake at approximately 30 °C below that temperature.

When the oven is cool, place the watch glass on a hotplate and heat until the material is slightly pliable, about 120 °C. Scrape the material with a knife onto a large 2”×3” 1 mm thick glass slide and melt. The temperature range varies but is generally around 85 °C to 90 °C and is correct when the material just becomes malleable. Knead the material with the knife, pressing and scraping toward the center of the slide to remove bubbles and mix. Increase the temperature to about 145 °C, or the temperature at which the material becomes transparent when sandwiched between the two slides. Place the other glass slide on top and press down, rotating the top slide to mix while pressing. Remove from heat to a heat sink and cool. Allow the hot plate to cool to less than 90 °C.

Pull the top plate back off and place both slides material side up on the hotplate and repeat, kneading material and then mixing by rotating the plates. Repeat this about three times for the initial pre-cake. Store wrapped in aluminum foil. Note: don’t manipulate the material when it is too hot since it sticks to the knife and will not knead. Also too cold just creates air pockets and increases the number of bubbles. The best temperature is one where the material is not runny but hot enough that the knife will stick if left in contact for more than a second or two. Waiting for the hot plate to cool to below 90 °C is necessary as well since putting the material on a hot plate causes small bubbles to form.

2.3.6 APC Buffer Layer Deposition

The amorphous polycarbonate (APC) must be pre-dissolved in chloroform at a low concentration in order to effectively filter the particulate matter from the APC. Start with 3 g APC and make a 5 wt% solution in chloroform, sonicating until uniformly dispersed. Filter out any remaining particulate matter through a 1 µm syringe filter into a round-bottomed flask and use the rotovap to remove all of the chloroform from the APC. Add cyclopentanone to the APC to make a 20 wt% solution and sonicate for 30 minutes.

Completely cover a clean electrode with the solution and spin at a high acceleration to 600 rpm for 6.5 seconds (including acceleration time) to achieve a final film thickness of 10 µm. A 7µm film can be obtained by spinning for 10 sec and a 12 µm film by spinning for 5 sec. Films cast in this manner thicker than 12 µm exhibit significant orange-peel and are unsuitable for use in devices.

Hold the sample under vacuum for 2 hours with no heat, and then slowly increase the temperature to 80 °C for at least 12 hours. Still under vacuum, follow with 1hr at 130 °C to anneal the film. The drying process outlined here is necessary in this order to prevent delamination of the film from the surface of the electrode. The annealing step does remedy any residual delamination from the drying. Chromophore doped films can be produced in the same manner (generally at 5 wt% loading with respect to the amount of APC) by adding the chromophore when the APC is dissolved in cyclopentanone and proceeding in the same manner.

2.3.7 Device Preparation Instructions

Clean 2 etched ITO electrodes by sonicating them in acetone or EtOH for 15 minutes. Test the ITO electrode conductivity across multiple points to ensure good performance then mark the electrode outline on the back of the slide with a permanent marker. Apply 100 µm (or other appropriate bead size) spacer beads suspended in vacuum grease down each side of one slide along the direction of the electrode but not touching it in 6 total locations, trying to get just enough for a single bead or so in each location. This is to prevent stacking of beads, which leads to an uneven sample thickness.

Put the electrodes on the hot plate during the next step. Pull apart the pre-cake slides and melt them on the hotplate at the correct working temperature (~80 °C-90 °C) until soft enough to cut off enough for a device (a standard 100 mg precake will make 4-5 samples). Knead the chunk a little to remove air bubbles and form into a cylinder shape and cut in half, making pieces that are approximately cubes. Place half on each slide in the center of the desired final active area. Re-cover the pre-cake in as close to the same orientation as it started to mitigate additional bubble formation.

Set the hot plate temperature to 164 °C for ECZ based devices (174 °C for BBP) and wait until the material begins to melt. Put the slides together, slightly overlapping the materials and press together while sliding the slides outward to ensure that the polymer sections are completely overlapping and that they cover the entire desired active area. Leave on the hotplate for three minutes at the correct temperature to ensure random orientation of the chromophores throughout the bulk of the device. Remove the sample to a heat sink for quick cooling, preventing crystallization. When cool, apply epoxy to all edges to prevent additional exposure to air.

3 REAL-TIME IMAGING OF CHROMOPHORE ALIGNMENT IN PHOTOREFRACTIVE POLYMER DEVICES THROUGH MULTIPHOTON MICROSCOPY

3.1 Introduction

A model with which to predict the effect of coplanar electrode geometry on diffraction uniformity in photorefractive (PR) polymer display devices was developed. Assumptions made in the standard use cases with constant electric field throughout the bulk of the media are no longer valid in the regions of extreme electric fields present in this type of device. Using electric field induced second harmonic generation (EFISHG) through multiphoton microscopy, the physical response in regions of internal electric fields which fall outside the standard regimes of validity were probed. Adjustments to the standard model were made, and the results of the new model were corroborated by holographic four-wave mixing measurements.

The PR polymer in this study was composed of four main components; a hole-conducting

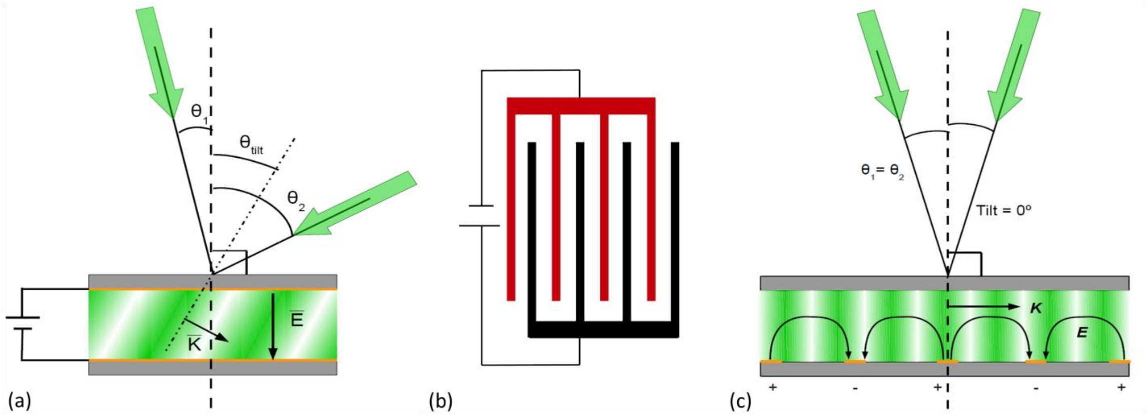

Figure 3-1: a) Diagram of the electric field applied by the standard sandwich electrode configuration and the required use case for transmission hologram recording; b) top view of the coplanar interdigitated electrode configuration; c) side view of the electric field orientations and writing geometry for devices using coplanar electrodes.

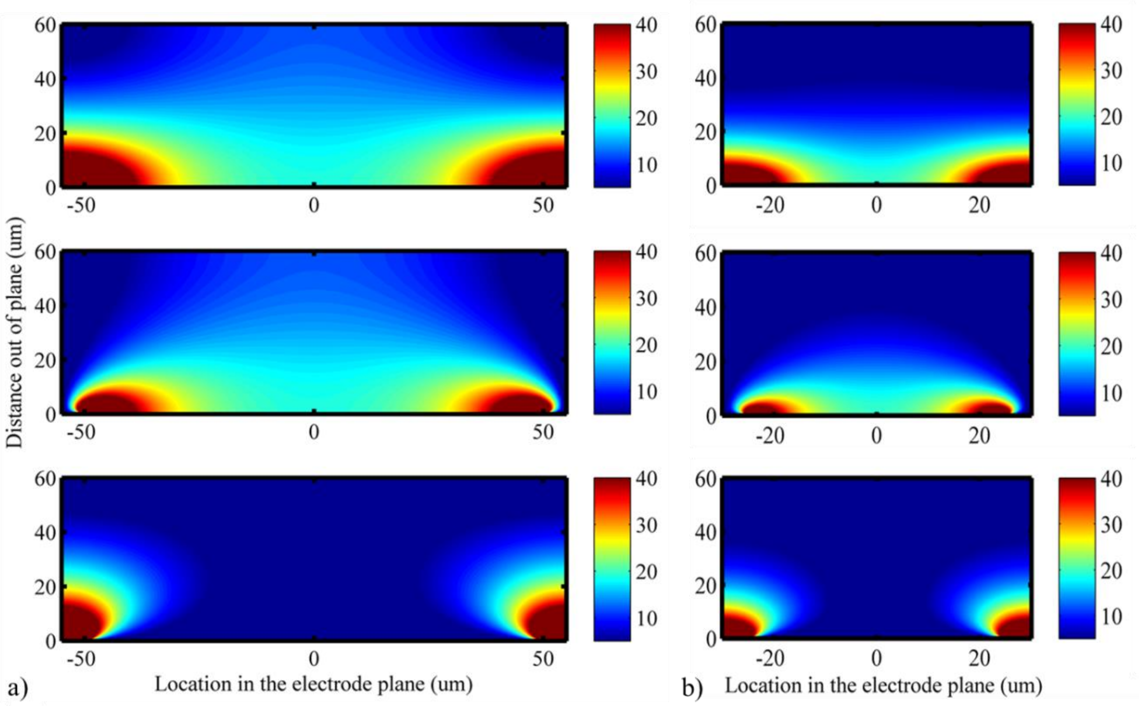

Figure 3-2: Cross-section representation in the same plane as Figure 3-1c of the coplanar electric field model. Scale bar units are in V/µm in response to 40 V/µm applied across a) 10 µm wide electrodes with 100 µm spacing (4000V bias) and b) 10 µm wide electrodes with 50 µm spacing (2000 V bias). The top figures show field magnitude while the middle and bottom figures show the horizontal and vertical field projection respectively.

polymer polyacrylic-tetraphenyldiaminobiphenyl (PATPD), the plasticizer ethyl carbazole (ECZ), 4-homopiperidino benzylidine-malonitrile (7-DCST) chromophore and a sensitizer [6,6]-phenyl-C61-butyric acid methyl ester (PCMB) in a ratio of 51.5:20:28:0.5 wt%, respectively. The polymer preparation procedure is detailed in Section 2.3.5, the electrode fabrication in Section 2.3.1 and the device preparation in Section 2.3.6.

Conventionally, to apply a bias across the films, the polymer material is pressed between two transparent conductive electrodes as illustrated in Figure 3-1a. In order for excited charges to drift into the dark regions, the grating vector (oriented perpendicular to the interference fringes) must have some projection in the direction of the applied electric field. This requires the device to be tilted at an angle θ_{tilt} with respect to the bisector of the two recording beams, an angle

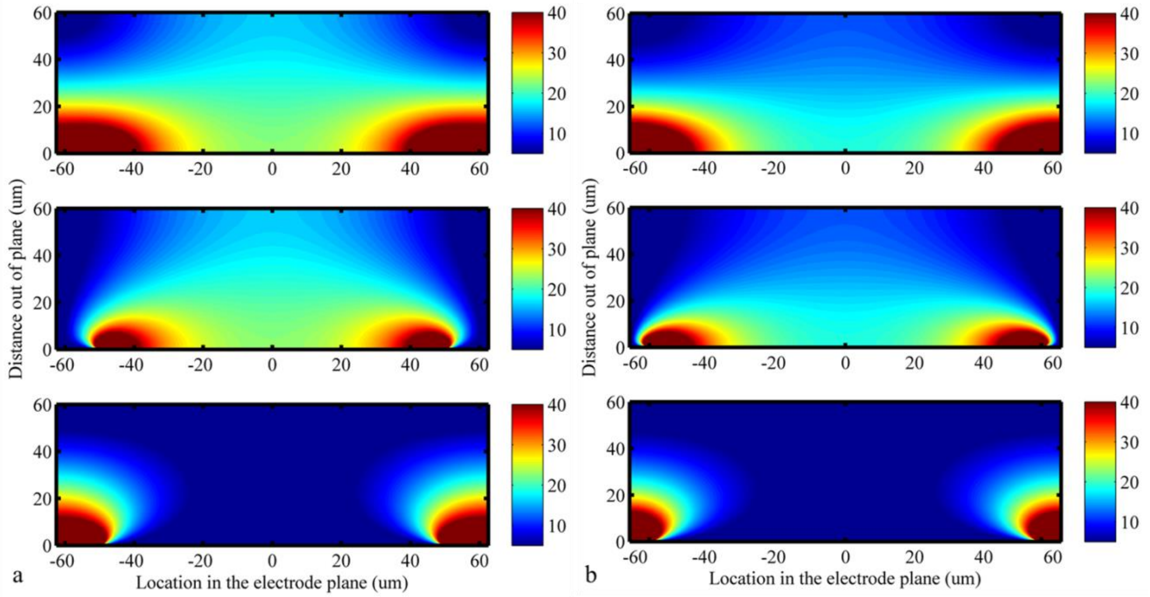

Figure 3-3: Cross-section representation in the same plane as Figure 3-1c of the coplanar electric field. Scale bar units are in V/µm due to 40 V/µm applied across a) 25 µm wide electrodes with 100 µm spacing and b) 10 µm wide electrodes with 100 µm spacing. The top figures show field magnitude while the middle and bottom figures show the horizontal and vertical field projection respectively.

generally on the order of 40° to 50°. In a recent study, a new type of electrode configuration was implemented, and, as illustrated in Figure 3-1b, consisted of interdigitated electrodes.[119] This geometry applies the electric field within a single plane, causing it to arc upward into the bulk of the polymer, as illustrated in Figure 3-1c maximizing the grating vector projection onto the electric field vector. This removes the necessity of tilting the device and can enable systems that do not support the tilted geometry.

In developing these new electrodes for use with PR polymers, the electrode width and spacing are both parameters that will affect the final device performance. Larger spacing between electrodes requires the application of higher bias in order to reach the same electric field inside the material, shown in Figure 3-2. The model is across a single repeating electrode structure with half electrodes on the sides and the inter-electrode spacing in the middle. Wider electrodes themselves leads to more area in which the electric field is not parallel to the grating

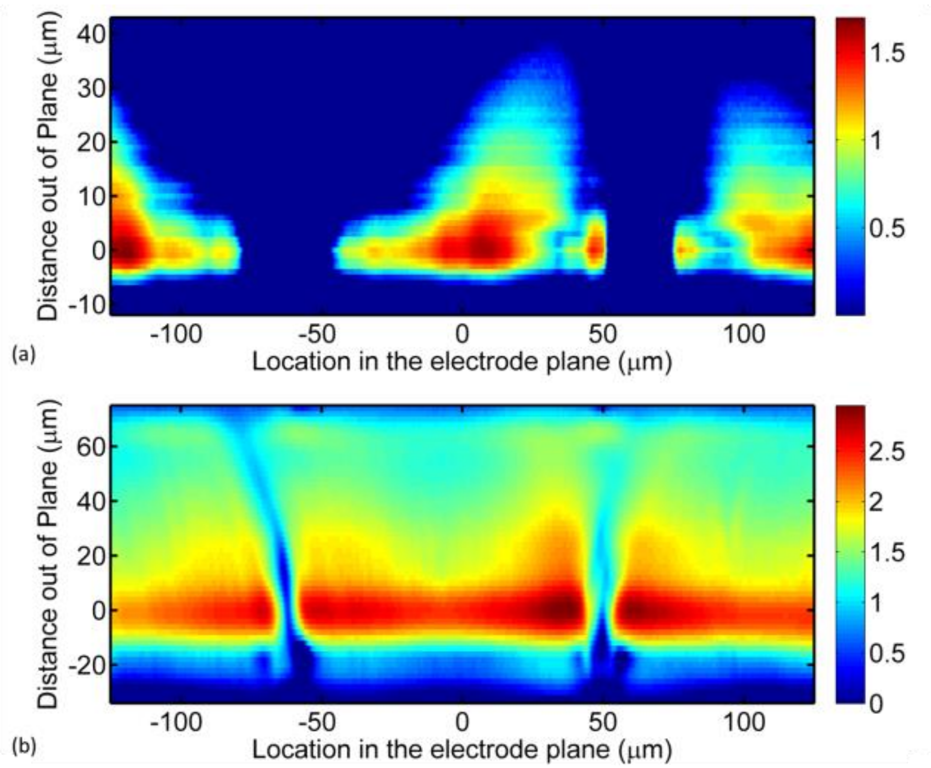

Figure 3-4: Cross-section of the intensity ($\log_{10}$ (counts)) of the second harmonic signal measured through the thickness of the polymer in the case of a) hole-conducting PATPD, 2000 V applied bias and b) non-conductive polystyrene, 4000 V applied bias. The grounded electrode is the right electrode imaged, located ~50 μm.

vector as illustrated in Figure 3-3. On the other hand as these parameters decrease, the larger scale spatial inhomogeneity of the electric field increases. This leads to the necessity of modeling the response of the PR polymer to various electrode geometries in order to determine the optimal use case.

Standard PR dynamics predictions make a series of assumptions which invalidate their use in low (< 10 V/μm) and high (> 60 V/μm) internal electric fields. In standard sandwich style electrode configuration, the use case is generally within this regime and the models accurately predict the behavior. In coplanar electrode devices, the field magnitude varies significantly throughout the bulk of the polymer and a method of extending the current model to

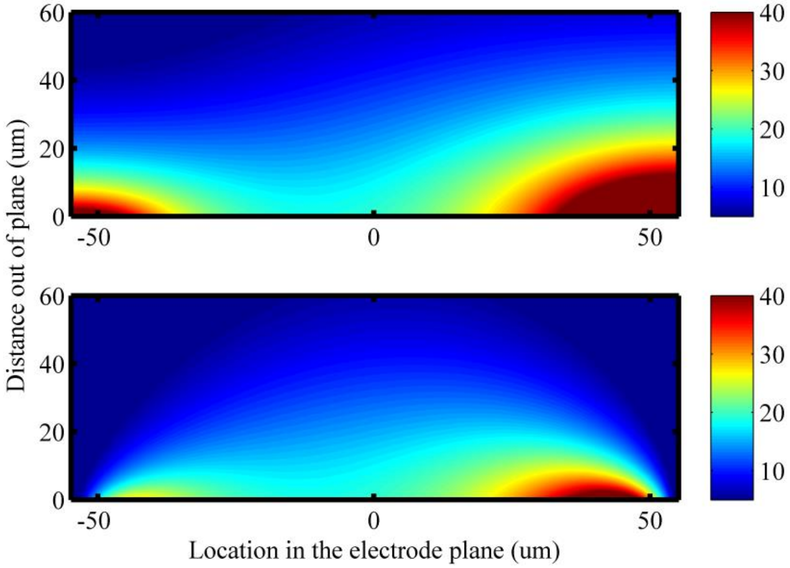

Figure 3-5: Cross-section representation in the same plane as Figure 3-1c of the coplanar electric field model including conductivity in the analysis. Scale bar units are in V/µm due to 40 V/µm applied across 10 µm wide electrodes with 100 µm spacing. The top figure shows field magnitude while the bottom figure shows the horizontal field projection.

accurately take into account these regimes must be developed in order to make accurate predictions.

One of the advantages of this coplanar geometry is that it enables the direct imaging and characterization of material response to electric fields through the use of techniques such as EFISHG. Investigation of these properties using either the standard sandwich style electrodes or a corona discharge type geometry has been performed in previous works, but these configurations limited the analysis to the bulk response of the material. This method effectively integrates both the material response and electric field inhomogeneities throughout the thickness of the polymer film.[130–133]

3.2 EFISHG Through Multiphoton Microscopy

The magnitude of the second-order susceptibility for this type of poled polymer system is relatively small, requiring high fundamental frequency intensity to produce a significant signal at

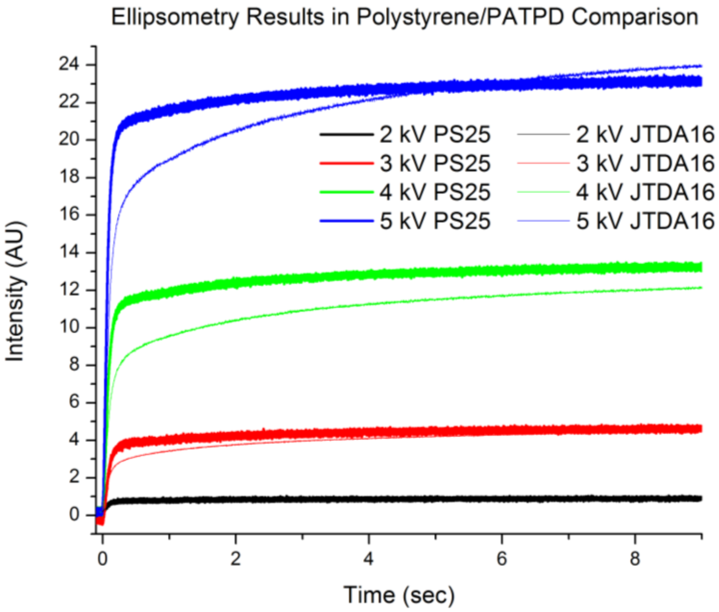

Figure 3-6: Dynamic transmission ellipsometry results for comparison of orientational response of the standard conductive material (JTDA16) and the non-conductive substitute (PS25) at a variety of applied voltages.

the second harmonic frequency. The system employed in these measurements was a near-IR laser scanning microscope, described in detail in Section 2.2.2.

The interdigitated electrodes were 100 nm thick indium tin oxide (ITO) on glass and were lithographically fabricated with 10 µm electrode width, 100 µm inter-electrode spacing, and 5 mm finger length, the procedure of which is described in detail in Section 2.3.1. The polymer composite was prepared by melt processing between the electrode and a blank glass cover slide with an active thickness of 60 µm. The second harmonic signal (780 nm) was collected with 0.5 µm in-plane microscope resolution and in 2 µm vertical steps through the bulk of the PR polymer.

Each measurement plane was parallel to the electrode plane. Figure 3-4 shows a log scale cross-section through the resulting volume of the second harmonic signal in false color ($\log_{10}$ (counts)) with an applied bias of 4000 V. The central 100 µm repeating structure

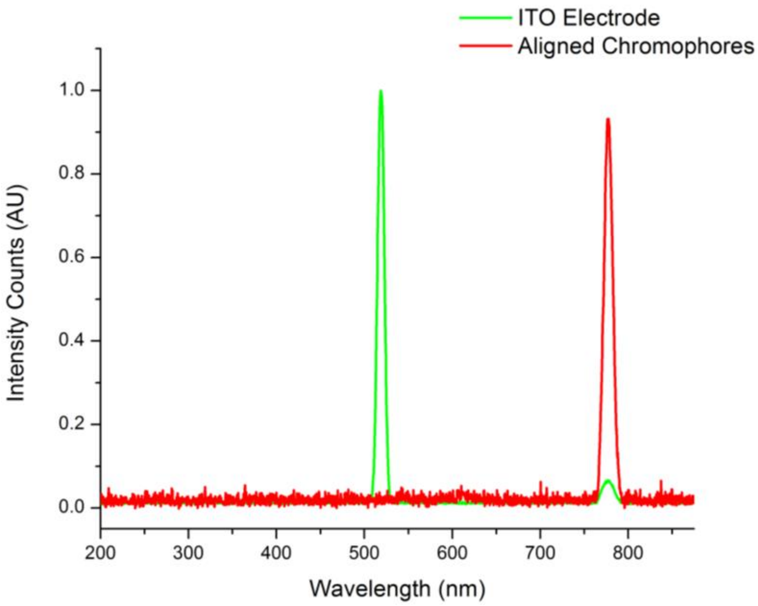

Figure 3-7: Spectra of the collected signal from the multi-photon microscope. The green curve is the signal with no applied voltage and no chromophore alignment. The red curve is with 2000 V applied across the electrodes. The wavelengths correspond to the second and third harmonic of the 1560 nm pump.

corresponds to the region between two electrode fingers of opposite polarity with the electrodes located at the zero point on the vertical graph axis.

Preliminary EFISHG investigations were undertaken using the standard hole conducting polymer base PATPD, with results shown in Figure 3-4a. The asymmetric form of the SHG signal is due to a decrease in electric field magnitude near the bias electrode. This indicates the presence of photoconductivity in the device and the location near the bias electrode signifies that the mobile species are holes, as would be expected in a hole-conducting polymeric system such as this (Figure 3-5). Typically the bulk effect of photoconductivity is relatively small but in the presence of intense optical fields, this effect obscures the direct electric field relationship to the intensity of the second harmonic signal. Subsequent characterizations were performed on a reduced conductivity system to decrease the number of assumptions that had to be made in the analysis. The polymer composite used in the final EFISHG characterizations (see sample

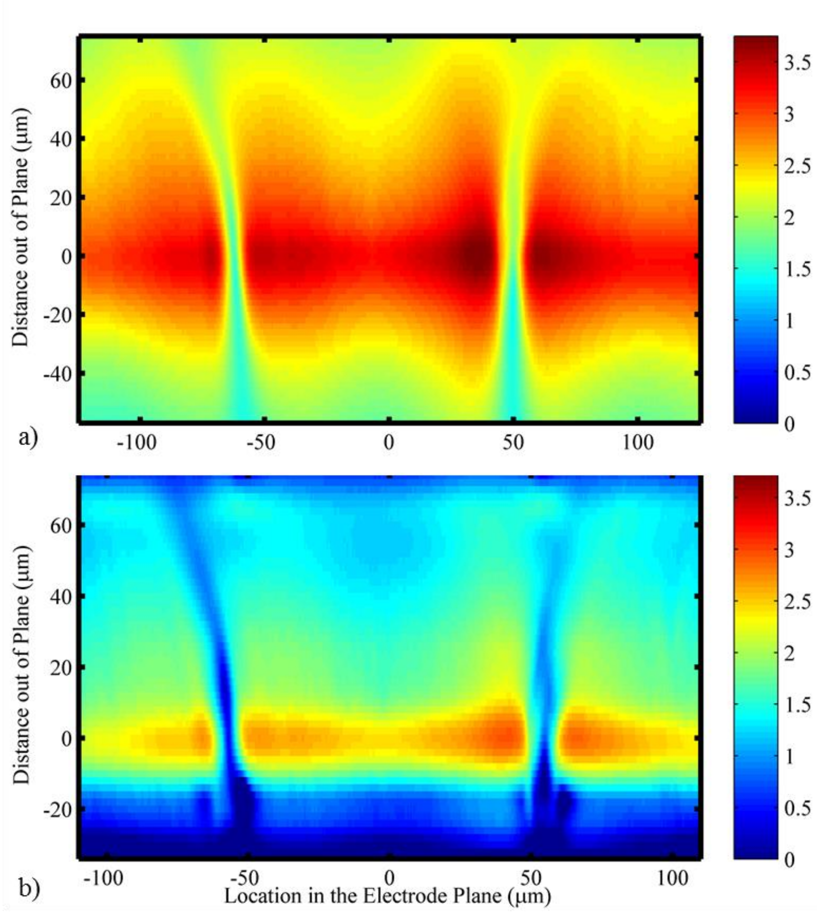

Figure 3-8: a) Slice of raw SHG signal volume and b) the results after deconvolution with the microscope transfer function.

measurement in Figure 3-4 (b)) was composed of the non-conductive polymer polystyrene, ECZ and 7-DCST in the weight percent ratio of 55:20:25.

The polystyrene composite was comparable to that of the standard PATPD based formulation in glass transition temperature (-4 °C measured by differential scanning calorimetry) and chromophore orientation speed and magnitude (characterized by transmission ellipsometry, results shown in Figure 3-6), ensuring that the EFISHG results would be applicable to the PATPD PR uniformity analysis. Photoconductivity measurements were not a valid comparison as the conductivity of the polystyrene system was extremely low.

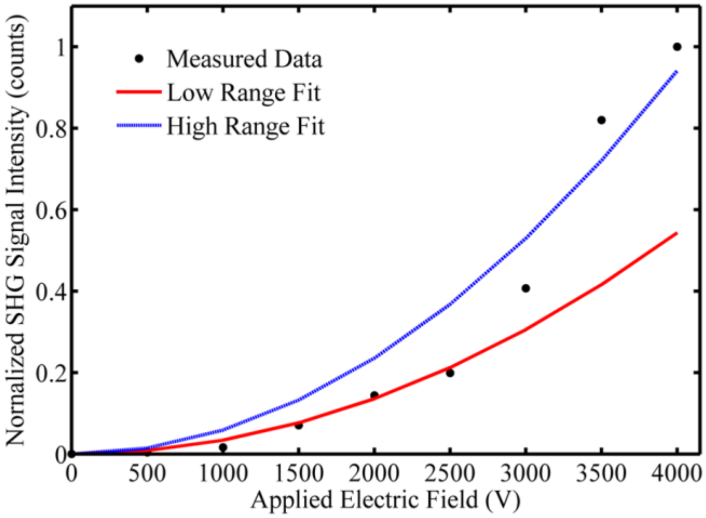

Figure 3-9: Intensity of the second harmonic signal as a function of applied electric field. Low range fit is for applied electric fields < 2500 V while the high range fit is for the > 2500 V range.

Measurements were taken over a range of applied electric fields from 0 to 4000 V and were confined to the central lengthwise region of the electrodes, far from the ends. Analysis along the length of the electrodes verifies that the orientational response is uniform in that direction in this measurement area. Verification of second (aligned chromophores) and third harmonic (ITO-electrode interface) generation was performed using a spectrometer with results shown in Figure 3-7. Figure 3-8a shows a cross section of the raw signal taken from the SHG volume of data. Deconvolution of this data from the transfer function of the microscope produces the data used in the following analysis (b). The transfer function was calculated using the no bias measurement of the THG signal in which the only signal was generated from a thin section on the surface of the substrate. The function was calculated such that deconvolution resulted in a line image.

The intensity of the second harmonic signal taken in the plane of the electrode (0,0) is shown in Figure 3-9. Based on the quadratic relation between the SHG signal and applied field, all of the data points would be expected to lie on the same $(E^0)^2$ curve. The results, however, indicate the existence of an effective orientational barrier between 2500 and 3000 V, below which the applied field was not high enough to fully overcome the thermal reorientation of the chromophores. The SHG intensity vs. applied electric field was fit to $I(2\omega) = C * (E^0)^2$ for the low and high field cases with the resulting trends shown in Figure 3-9. Above 3000 V applied bias, the standard chromophore orientation response to the electric field in the PR response models was valid. As indicated by the results at low bias, an orientational threshold voltage exists for the system under test and a modification to the following model was necessary for the regions of the device with lower field magnitudes.

3.3 Diffraction Uniformity Model

A map of the electric field was calculated for the experimental coplanar electrode geometry for use in the PR model to predict diffraction uniformity. By assuming an infinite extent of the electrodes along their length, this 3D geometry can be reduced to a 2D analysis, producing the applied electric fields and orientation in the PR material with minimal computation time. This assumption is valid due to the configuration of our electrodes, with the length 50 times larger than the electrode width and spacing and the illumination occurring well away from the ends of the electrodes. The Laplace equation, $\nabla^2 V = 0$, describes the electrostatic potential in a non-conductive media according to Dirichlet boundary conditions which set the applied bias at the electrodes, and Newmann conditions which constrain the form of the response along the remaining boundaries.

The response of the polymer system to an external bias depends on the overall magnitude of the electric field (Figure 3-10a) in some cases; in others it is the projection of the electric field vector onto the grating vector that is the dominant factor. Figure 3-10b shows the calculated electric field projection onto a horizontal grating vector resulting from an untilted geometry.

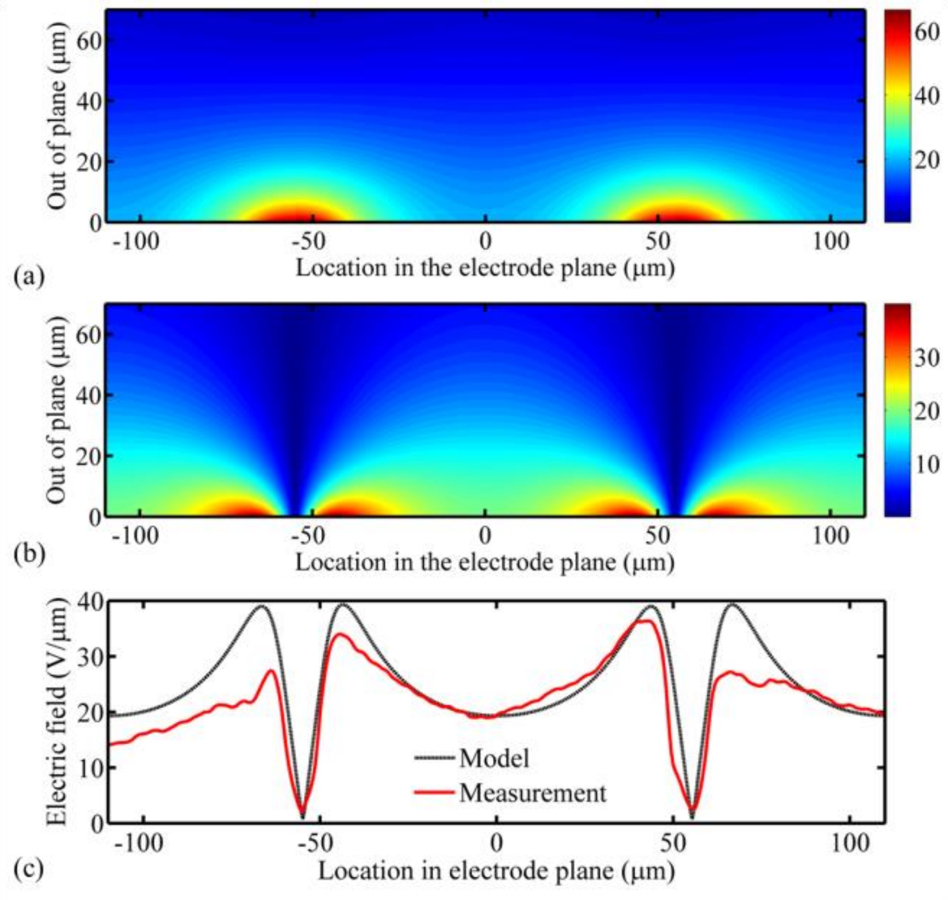

Figure 3-10: a) Electric field magnitude and b) horizontal vector component applied by coplanar electrodes at 4000 V bias. Electrode width 10 μm, spacing between electrodes 100 μm, magnitude units in V/μm; c) comparison of theoretical horizontal electric field component at the electrode surface (*z*=0) to the value obtained from EFISHG measurements at 4000 V applied bias.

Figure 3-10 (c) displays the comparison of the theoretical horizontal projection of the applied electric field and the square-root of the EFISHG values ($I(2\omega) \propto (E^0)^2$) in the plane of the electrode (z=0) at 4000 V applied bias.

Since the EFISHG measurements are qualitative in nature for this application, the measurement was normalized to the central field value for the model. It can be seen that there is a good degree of agreement between the electric field model and the measurement which means that upon taking into account the low-field orientation correction factor, this electric field model can be used for predicting PR response to coplanar electrodes. The decreased peak intensity of the SHG signal at the edges of the range seen in Figure 3-10c is due to the slightly curved focal plane of the scanning beam across the extent of the image plane. The central electrode region spanning from -55μm to +55 μm in Figure 3-10 is the section over which the generated signal that was collected originates from the same 2 μm vertical measurement step. Outside this range, the focal location of the fundamental beam is higher, reducing the peak intensity with which the second harmonic was generated. Due to this, the central electrode region is the one that is used for measurement analysis, such as in Figure 3-9.

Dynamic models of photorefractivity in polymers have long been used to direct the formulation of new and more efficient PR devices. Ostroverkhova modified the Schildkraut and Buettner model describing the relationship between material parameters and electric fields and their contribution to the PR response.[20–22] The response depends on a variety of material parameters such as sensitizer densities and trap levels, but in this case the focus is on the effect of the electric field dependent parameters. These are the photogeneration cross-section (s), hole drift mobility (μ), and trapping (γ) and recombination (γ_T) rates with field dependencies on either the magnitude of the applied field (E_{ext}) or the projection of the field onto the grating vector(E_{proj}) as follows

$$s = s(E_{ext})\left({}^{E}\!/_{E_{ext}}\right)^{p} \tag{3-1}$$

$$\mu = \mu(E_{proj})e^{\beta_\mu\left(E^{1/2} - E_{proj}^{1/2}\right)} \tag{3-2}$$

$$\gamma = \gamma(E_{proj})e^{\beta_\mu\left(E^{1/2} - E_{proj}^{1/2}\right)} \tag{3-3}$$

$$\boldsymbol{\gamma_T = \gamma_T(E_{proj})e^{\beta_\gamma\left(E^{1/2} - E_{proj}^{1/2}\right)}} \tag{3-4}$$

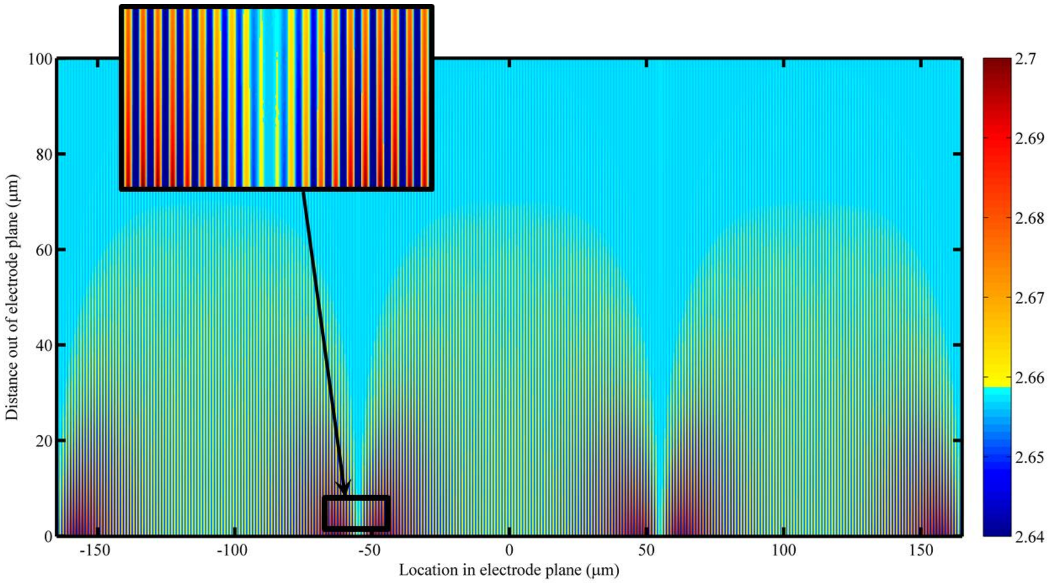

Figure 3-11: Sample n^2 across 10 μm wide 100 μm spacing electrodes illustrating the large scale modulation with 110 μm repeating period due to the underlying electrode structure and the smaller ~1 μm repeating structure due to the interference of the writing beams.

The system described in (1-2) through (1-7) is simplified through Fourier decomposition, the assumption that the incident light field takes the form of

$$I = I_0 + I_1 \cos kx \tag{3-5}$$

and the parameter solutions take the form of

$$\xi = \xi_0(t) + \xi_1(t)\left(C_{\xi 1} \cos kx + C_{\xi 2} \sin kx\right) \tag{3-6}$$

The zeroth and first spatial Fourier components are used to analyze the photoconductivity under homogeneous illumination and the dynamics under the sinusoidal field, respectively. These models are then fit to experimental photoconductivity and four-wave mixing results in order to determine the material parameters and analyze the dynamics of the system. The calculation parameters for this analysis were set to match the subsequent test cases, with angle of 30° between the two writing beams, tilt angles ranging from 0° to 20° with respect to the sample normal (effectively changing the orientation of the grating vector with respect to the sample normal), a recording wavelength of 532 nm, and illumination of 30 mW/cm^2.

Using the electric field model to evaluate these parameters across the electrodes, and incorporating the low field adjustments from EFISHG measurements, the resulting space-charge field was used to calculate the refractive index modulation of the form (from (2-18))

$$\Delta n = constant * E^0 * |E_{SC}| * cos\, \varphi \tag{3-7}$$

where φ is the angle between the grating vector and the electric field vector. The constant term is related to material parameters and is not field dependent. The orientational corrections to the electric field from Figure 3-9 are applied in this calculation and decrease the low applied field contribution to the index modulation.

The index modulation calculated here results in the diffraction grating that is recorded in response to the interference of the writing beams in the material, so the decrease in electric field with increasing distance from the electrodes (Figure 3-10a and b) leads to a refractive index modulation whose magnitude is an order of magnitude higher near the edges of the electrodes than in the remaining bulk of the material, affecting the diffraction of the reading beam. Computational propagation of the reconstruction beam through the grating (Figure 3-11) in order to analyze diffraction uniformity across the beam was performed using the Crank-Nicholson method.[134] Implementation of periodic boundary conditions took advantage of the repeating nature of the electrode structure, so only three repeating electrode structures were used along with a device thickness of 100 µm. Solution verification was performed by calculating the diffraction grating due to a uniform electric field under the same writing conditions and propagating both planar and Gaussian wavefront optical fields through it. Both incident field results showed the expected 100 % uniformity of the diffracted beam. These tests additionally

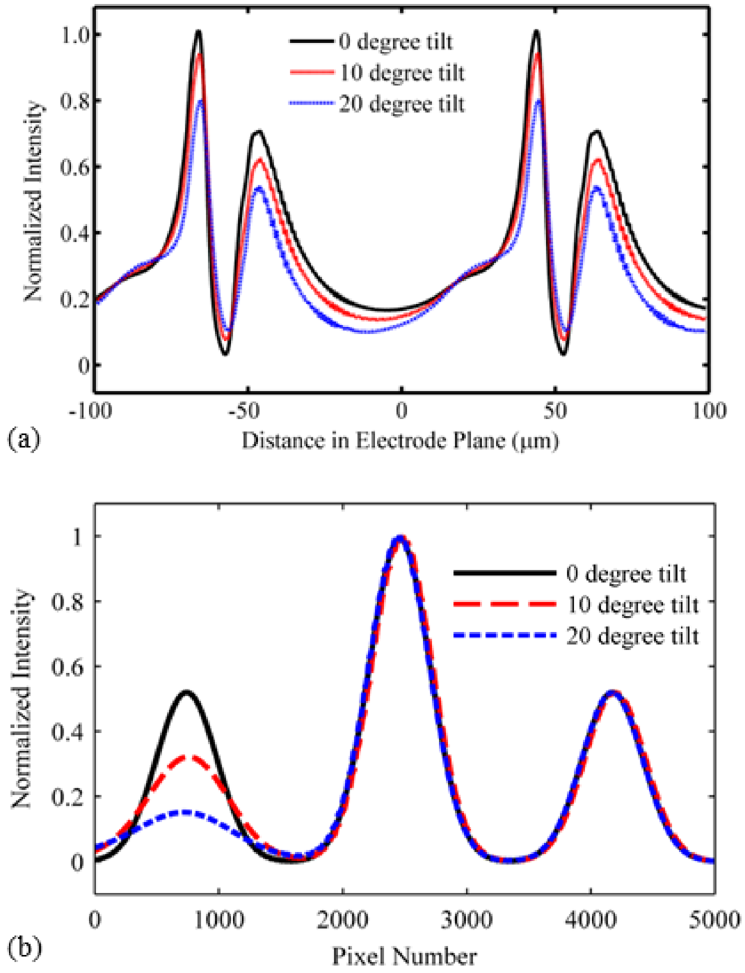

Figure 3-12: Propagated reconstructed beam at 0, 10, and 20 degree tilt angle geometries of the recording beams in a) electrode and b) full beam scales.

validated the use of an infinite extent plane wave in the following analysis to remove the Gaussian envelope from the uniformity analysis. Figure 3-12a shows the results of the spatial distribution of the diffracted beam after propagation through the PR polymer across one period of the electrode structure. The effect of the spatially inhomogeneous electric fields is to concentrate diffraction of the reconstructed beam near the electrode edges, which affects the resulting beam uniformity in a high spatial frequency manner. Tilting the writing beams with respect to the normal to the sample plane increases the number of these high index regions that the reconstruction beam encounters. For a range of tilt angles from 0 to 20 degrees, the high frequency components peak power to root-mean-squared (RMS) ratio decreases by 15 %. Also called the crest factor in signal processing, the peak to RMS ratio is a measure of how extreme the peaks are in a signal, and indicates an increase in the spatial homogeneity of the reconstructed beam with increasing tilt angle.

To analyze the low spatial frequency effects of diffraction from the underlying electrode structure, an 800 µm diameter Gaussian beam was propagated through basic split-step beam propagation and absorbing boundary conditions with a 40 mm analysis space. The grating parameters and thickness remained the same with respect to the previous model. The change in the analysis method used here was due to the increased robustness of this propagator at larger sampling steps (to counter the larger analysis space in computation time), which, while obscuring some of the fine detail represented in Figure 3-12a, reproduced the lower spatial frequency results accurately. Figure 3-12b shows the propagation results of the full width of the reading beam in the output plane (total diffracted angle 30°). The central portion is the primary diffracted beam from the high frequency grating and is Bragg matched to that grating. The presence of side lobes is due to diffraction from the underlying low spatial frequency refractive index modulation from the periodicity of the applied electric field (Figure 3-11). The angle of diffraction from this grating period is only ~0.09° and both of the side lobes deviate slightly from the Bragg angle of the high frequency grating, reducing the efficiency of their diffraction. With increasing tilt angle, the diffracted order that is closer to the sample normal than the reconstructed Bragg angle (left peak) is less efficiently diffracted by the base structure due to its increasing Bragg mismatch.

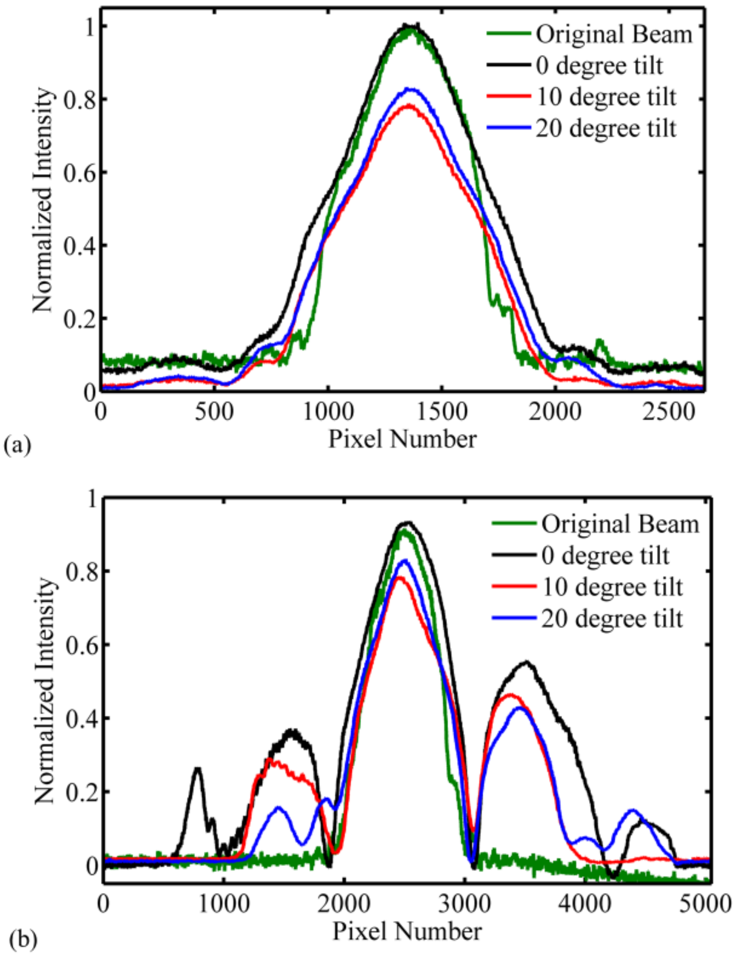

Figure 3-13: Cross-sections of the measured incident and diffracted beam profiles taken a) out of the plane of diffraction and b) in the plane of diffraction for various tilt angles.

3.4 Model Validation Using Four-Wave Mixing

Experimental verification of the applicability of these adjusted models in device design was executed. Non-degenerate four-wave mixing measurements were performed (see Section 2.2.3 for additional detail) in which a grating was formed by two *s*-polarized 532 nm mutually coherent beams with an inter-beam angle of 30°. The orientation of the coplanar electrodes was also such that the electrodes extended in the *s*-polarization direction, ensuring that the generated charges traveled across the fringes to become trapped instead of along them. A 633 nm reading beam counter-propagating at the appropriate angle accounting for the wavelength mismatch diffracted from the grating and was monitored by a CMOS detector for 0, 10, and 20 degree tilt angles. Figure 3-13a shows the original and diffracted beam profiles taken in a cross-section perpendicular to the plane of diffraction. As expected, there was no significant change in the profile of the beam since this is the direction along the fringes and perpendicular to the underlying electrode index modulation. Figure 3-13b is a cross-section in the plane of the electrode index modulation and multiple orders flanking the primary diffracted beam are present. Note that the original beam intensity was scaled to the range of the central diffracted lobes. Variability between the intensity of the central lobes for the different tilt angles is due to minor alignment deviations between the configurations but normalization of these results would have unduly emphasized the fine structure of some of the measurements. The decrease in the intensity of the left order follows that of the theoretical model (Figure 3-12b). The fine structure inhomogeneity from the micron-scale diffraction analysis is seen in the side lobes orders but is insignificant in the magnitude of the full diffracted beam. This indicates that the non-uniformity due to the spatial electric field modulation is a more significant effect on the secondary orders.

3.5 Conclusions

Interdigitated electrodes are a novel electrode configuration for use in photorefractive polymer devices that enables diffraction without applying tilt in the recording geometry. This pattern, however, generates a highly inhomogeneous electric field within the bulk of the material that impacts the diffraction amplitude and uniformity. In this paper, the EFISHG technique was used to directly image the orientation of the chromophores to the electric field. The observed response was used to adjust the standard model of refractive index modulation in PR polymer devices to take into account the non-uniform electric fields. The corrected PR response model was used to calculate the recorded holographic gratings and enabled predictions of diffraction uniformity across the beam through computational wavefront propagation. Observations of diffracted beam uniformity correlate to the model predictions, indicating that this model is valid in predicting the effect of the coplanar geometries, including the extreme field magnitude regions.

Future work will include using this validated model to optimize the electrode parameters for maximum diffraction uniformity. These devices will then be fabricated for further testing and characterization. Additionally, the EFISHG technique may be used in studies of new conductive polymers for PR application as it was seen to afford an in-situ qualitative measure of conductivity. In dispersive transport systems such as PR polymers where time-of-flight measurements are inconclusive for measuring mobilities, this technique may yet provide an alternative analysis method.

4 NINE ORDER OF MAGNITUDE PULSE RESPONSE OF PHOTOREFRACTIVE POLYMERS TOWARD VIDEO-RATE HOLOGRAPHIC DISPLAY

The recent development of a single mode fiber-based pulsed laser with variable pulse length, energy, and repetition rate has enabled the characterization of photorefractive devices in a previously inaccessible regime located between millisecond and nanosecond pulse recording. A pulse width range of nine orders of magnitude opens the door to device and supporting laser optimization for use in video-rate holographic display. Device optimization has resulted in 5x improvement in single pulse four-wave mixing diffraction efficiencies to 10 - 11.5 % at pulse widths ranging between 6 ns and 100 µs. The grating recording time was likewise reduced by 5x to 16 ms at an applied bias of 72.5 V/µm. These improvements support 30 Hz update rates, which combined with the 3.3 - 10 kHz repetition rate pulsed laser, pave the way a for real-time updatable holographic display.

4.1 Introduction

The world of two-dimensional images and displays is a familiar one, with computer monitors and televisions integrated into many aspects of daily life. Within these photographs and videos, a number of visual clues are assimilated, giving a sense of depth and reality to the viewer. Shading, linear perspective, and the occlusion of more distant objects by those that are nearer are a few of the main indicators of three-dimensional spatial relationships in a two-dimensional representation. In an accurate three-dimensional representation, there are additional clues such as binocular disparity, motion parallax, accommodation and vergence that are instrumental in the three-dimensional interpretation. Binocular disparity is the presentation of different views of a scene to each eye due to their horizontal offset while motion parallax is the changing of the scene itself based on viewer movement. Together these phenomena are the basis for stereopsis; the

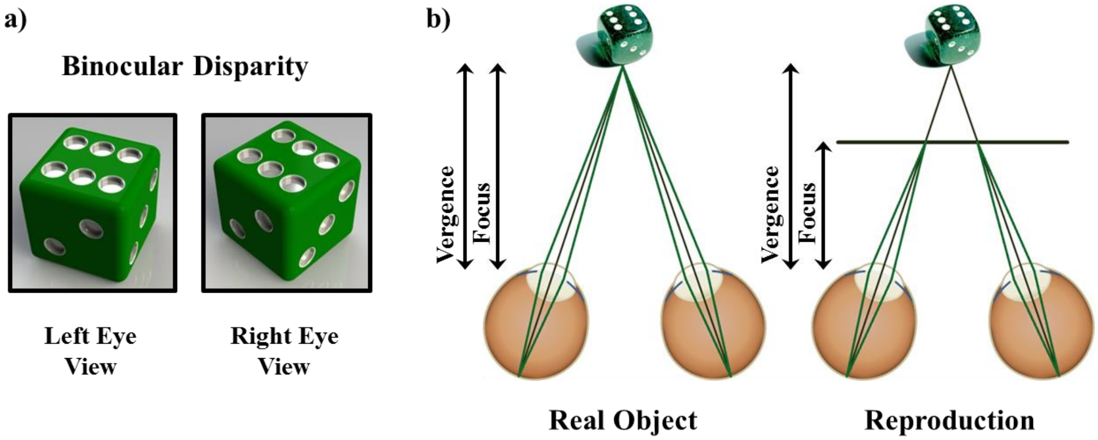

Figure 4-1: An illustration of visual system parameters used to interrogate a three dimensional scene. a) Binocular disparity is the presentation of different scenes to each eye and is used to determine depth and distance in a process called stereopsis. b) In real objects, both eyes rotate to look at an object with the eyes focusing at the same location. Vergence-accommodation conflict occurs in stereographic systems where parallax maintaining images are displayed on a two dimensional screen. The eyes rotate in response to the image shear but the focus of the eyes remains at the screen displaying the image, causing a disparity between these two clues.

ability of the brain to distill depth, distance and size information from the various images (Figure 4-1a). Accommodation and vergence are the acts of focusing and rotating the eyes to look at an object as shown in Figure 4-1b, with both providing additional information to the brain regarding specific features of the scene.

State-of-the-art commercial systems have attempted to utilize some of these clues through the implementation of two-view stereoscopic displays. These types of systems impart binocular disparity by presenting both of the images needed to reproduce a particular viewing location and use a filtering device such as glasses to ensure that the correct scene is displayed to each eye. Two problems with this approach are the failure to reproduce motion parallax and the production of conflicting signals based on the vergence and accommodation of the eyes. When observing a real object, the information from each of these parameters agree, but for a scene displayed by a two-view system, the eyes converge to the correct position but focus on the screen of the display.[120] In many viewers, the mismatch of these visual cues can cause dizziness and discomfort over extended viewing periods. To alleviate this issue, the display should reproduce not only the necessary images for each eye, but also the direction from which each image is originating (binocular disparity) as well as the distance of the object from the viewer (vergence and accommodation).

A hologram is precisely suited to this task as it can reproduce the amplitude and wavefront of the scene. Computer generated holography has enabled the rendering of any object without requiring its physical presence by calculating the wavefronts as they would appear had they originated from a real object. These wavefronts are then computationally interfered with a reference beam creating a holographic fringe pattern that is displayed by a spatial light modulator (SLM). When the SLM is illuminated by a real wavefront matching that of the reference beam used to calculate the fringes, the computer generated object is displayed in three dimensions.[135] One drawback of this technique is the difficulty of calculating wavefronts and fringes for real scenes captured by video or photographs from a variety of angles. Another is the extreme resolution necessary to display the holographic pattern on a light modulation device. The resolution of a holographic display is related to the pixel count on the SLM while the size of the reproduction is inversely related to the size of the fringes themselves. For a 20 inch display with a resolution matching that of the human visual system, the pixels on the SLM must be a fraction of a micrometer, quickly updatable and number in the trillions. Running a three-color, 8-bit, 30 Hz system of this type would require transmission of 10^{16} bits per second, nine orders of magnitude more than a standard 1080i HDTV.

Holographic stereography, or integral image holography, bridges the gap between two-view stereograms and the bandwidth-hungry hologram. These systems holographically record the directionality of light for a discrete series of viewing locations, providing static and motion parallax without having to resort to direct fringe computation and display. They are also inherently amenable to the recording of real scene footage taken from multiple viewpoints. As the number of distinct viewing locations or views increases, the reproduced scene begins to resemble the original scene more closely. This eliminates the vergence-accommodation conflict for objects reproduced near the film plane when the wavefront of the projected image approaches that of the object and, for a system with similar parameters to the holographic one described above, requires only 10^{12} bits per second to be transmitted to the device.[136] Utilizing photorefractive polymer as the recording medium in this type of display opens the door to eye-wear free, real-time updating holographic displays.

Improvements in photorefractive polymers have advanced this technology from a small, slowly refreshing proof-of-concept system to one that is nearing its premiere as a truly video-rate holographic display. Previous work focused on optimizing the diffractive response of the devices to respond to 6ns pulses delivering 200 mJ per pulse at a 50 Hz repetition rate while reducing the absorption of the material itself in the blue region to enable full-color image reconstruction.[5] These improvements enabled the recording of a 300 mm×150 mm display in less than 8 seconds and full-color reconstruction with a color gamut extending beyond the NTSC CIE color space.

Progress toward faster refresh rates was previously limited by a combination of the need to improve the sensitivity of the PR polymer to the recording intensity and the availability of current laser technology, which fell short of the need for a 532 nm wavelength range pulsed laser with tens of millijoules per pulse and kHz repetition rates supporting video-rate recording. The development of a new, single mode fiber based laser enabled the characterization and optimization of the PR polymer devices across a previously inaccessible region of pulse lengths between the 6 ns Q-switched pulse and a 1 ms externally chopped CW beam. The new system was capable of delivering up to 100 µJ of pulse energy across a range of pulse lengths from 250 ns to 1 ms and repetition rates of up to 10 kHz. In analyzing the time response and diffractive performance of the current systems in this new area, it was possible to concentrate the performance optimization on a region of pulse lengths and energies supporting 30 Hz refresh rates.

4.2 Photorefractive Polymers for Updatable Display Holography

The PR polymer in this study was based on a modified version of the PATPD used in the previous chapter in which carbaldehyde aniline (CAAN) was attached to the PATPD copolymer chain in a ratio of 10:1 (TPD:CAAN). This additional component reduces the tendency of the low T_g guest-host system to phase separate, increasing the loading limit of the chromophore, fluorinateddicyanostyrene 4-homo- piperidino benzylidine malononitrile (FDCST). The plasticizer in this case was benzyl butyl phthalate (BBP), and the sensitizer was [6,6]-phenyl-C61-butyric acid methyl ester (PCBM). The components were in a ratio of TPD:CAAN/FDCST:BBP:PCBM (56.23:33.74:9,84:0.2 wt%) and prepared in the standard sandwich style device configuration with the polymer preparation procedure detailed in Section 2.3.5 and the device preparation in Section 2.3.7. The electrodes (with in-house etching procedure described in Section 2.3.1) were commercially purchased from Thin Film Devices. The samples with buffer layers have a 10 µm amorphous polycarbonate (APC) layer on one electrode, the procedure for which is outlined in Section 2.3.6 and otherwise the device fabrication is the same as for the samples with no buffer layer.

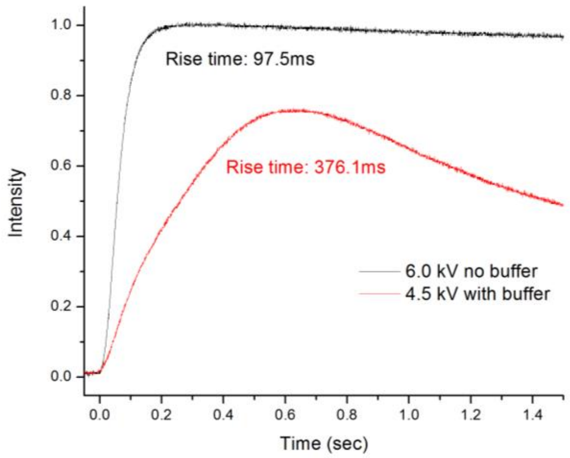

Figure 4-2: Ellipsometry measurement comparing speed of chromophore orientation for the buffered and un-buffered device configurations.

4.3 Pulse Response Dynamics Through Four-Wave Mixing

Three primary time-dependent phenomena contribute to the development of a refractive index grating in a photorefractive polymer. The first is photogeneration of charges in response to the incident illumination, taking on the order of picoseconds. As this is three orders of magnitude faster than a nanosecond pulse, it is not a process that will be significantly affected by the pulse lengths under investigation here. On the other hand, this effect is highly intensity dependent and will play a large role in the trend between the magnitude of the diffraction efficiency and the pulse energy. Additionally, the photogeneration efficiency is electric field dependent, leading to an expected difference in performance between the buffered and unbuffered devices. The second step is the transport and trapping of the now excited charge carriers, with characteristic times on the order of 0.1-5 ms, well within the range of pulse width interest. These processes are highly field dependent and are also expected to play a role in the buffer/no buffer comparison. The final step is chromophore orientation to the space-charge field, taking on the order of 0.1 ms to 1 ms, again on the scale of interest and again a highly field dependent effect.

Application of a 10 µm non-conductive APC buffer layer to one of the electrodes results in a decrease of the bias across the sample at which the overmodulation of the diffraction efficiency occurs. This reduces the working bias of the material for maximum diffraction efficiency compared to the same composite in an un-buffered configuration. The only electric field dependent parameter in this behavior, as given in (1-18), is the refractive index modulation. An increase in its magnitude at a lower applied bias indicates an increase in the effective trap density due to the thin injection barrier of the APC on one of the electrodes as shown in Figure 1-5 relating the magnitude of the induced space charge field to the trap density and externally applied field. Lowering the bias applied across the device in response to the new overmodulation peak also affects the those material parameters whose dynamic responses are dependent on the external field, such as the mobility (see (3-2)) and the speed of chromophore orientation. Figure 4-2 shows the results of dynamic ellipsometric measurements (Section 2.2.1) of the sample with and without a buffer layer. The overall time to reach maximum chromophore alignment is nearly four times longer for the buffered sample. This combination of effects results in a device that has a better diffractive performance at lower applied bias but also has a slower response. The goal of these studies was to determine if the response of this type of device was sufficient for video-rate display and explore avenues for improvement.

4.3.1 Nanosecond, microsecond and CW sources for FWM

The standard method of characterizing the time response of grating recording is using four-wave mixing, described in detail in Section 2.2.3. Since the lasers used here were pulsed or chopped, a separate 633 nm HeNe continuous wave laser was used as the probe beam. The use of three different lasers enabled measurements of PR polymer response to pulse width and energy from 6 ns to 1 sec, covering nine orders of magnitude. The shortest time scale measurements were

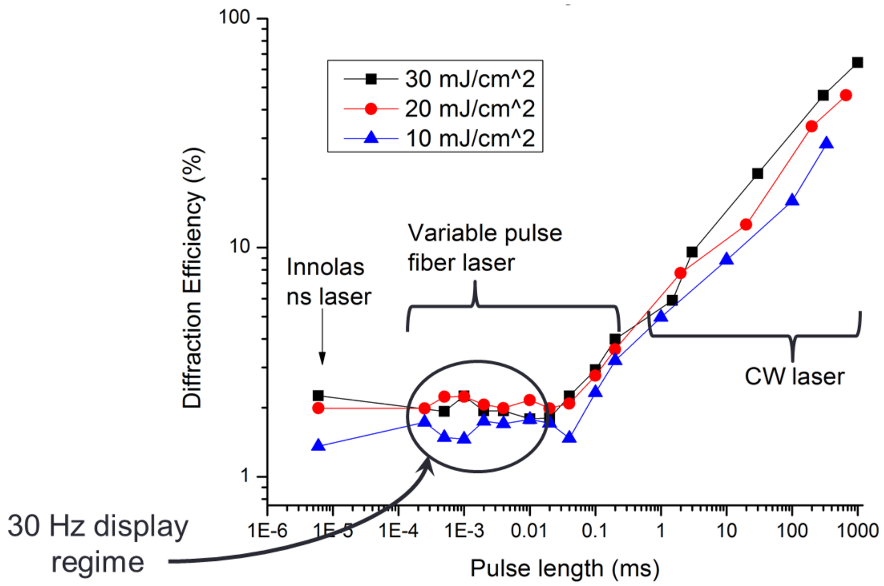

Figure 4-3: Diffraction efficiency vs. pulse width for a range of pulse energies on samples with a 10 μm APC buffer layer.

performed using a 6ns 532 nm InnoLas SpitLight laser with single pulse capabilities and energies ranging up to 200 mJ per pulse. Lenses of 250 mm focal length focused the writing and probe beams onto the sample plane, resulting in a beam waist at the sample plane of 57 μm.

The intermediate pulse length measurements utilized the new variable pulse length fiber laser with pulse energy of up to 100 μJ, pulse lengths from 250 ns to 1 ms and repetition rates of up to 10 kHz. This laser was based on a 1030 nm solid-state fiber laser externally modulated to create a pulse train with appropriate pulse width, shape, and repetition rate using a fiber-coupled acousto-optic modulator (AOM) driven by an arbitrary waveform generator. The shape of the waveform was adjusted here such that the convolution with the effects of subsequent distortions resulted in a Gaussian temporal pulse shape. The final pulses were frequency doubled to 514 nm and again externally modulated using a free-space AOM to select single pulses. The coherence length of the doubled signal was significantly shorter than the pump signal, the mechanism of which is still under analysis. The final coherence length of 1 cm was measured using an external

Michelson interferometer system at 50 % fringe visibility. The path length of both writing arms in this FWM system was tightly constrained to maximize the intensity modulation of the recording fringes. Lenses of 250 mm focal length focused the writing and probe beams, resulting in a beam waist at the sample plane of 82 µm.

The longer time scale pulses were created using a 532 nm Coherent Verdi V18, a single longitudinal mode CW optically pumped semiconductor laser with a maximum power of 18 W. The beam was externally modulated using an AOM to create single pulses with widths ranging from 1.5 ms to 1 sec. Lenses of 250 mm focal length focused the writing and probe beams, resulting in a beam waist at the sample plane of 17 0µm.

Four-wave mixing measurements were performed on AS-J2 samples with a single 10 µm APC buffer layer in order to characterize the current state-of-the-art device across a range of pulse energies, from 10 mJ/cm^2 to 30 mJ/cm^2 and across the entire range of pulse widths. The results are shown in Figure 4-3, displayed in log scale to show the microsecond pulse width regime clearly.

4.3.2 Comparison of devices with and without a buffer layer

For longer pulse lengths, depicted by the linearly decreasing region on the plot, the decrease in diffraction efficiency is due to a combination of photoelectric, orientational and diffractive effects. The process of grating formation in photorefractive polymers begins with absorption of the interfering pulses in the bright regions of the fringes. The rate of space-charge field formation at a constant external bias depends on the number of excited charge carriers. As the energy per pulse is decreased for constant pulse width, the number of mobile charge carriers decreases, correlating to a decrease in the space charge field and refractive index modulation.

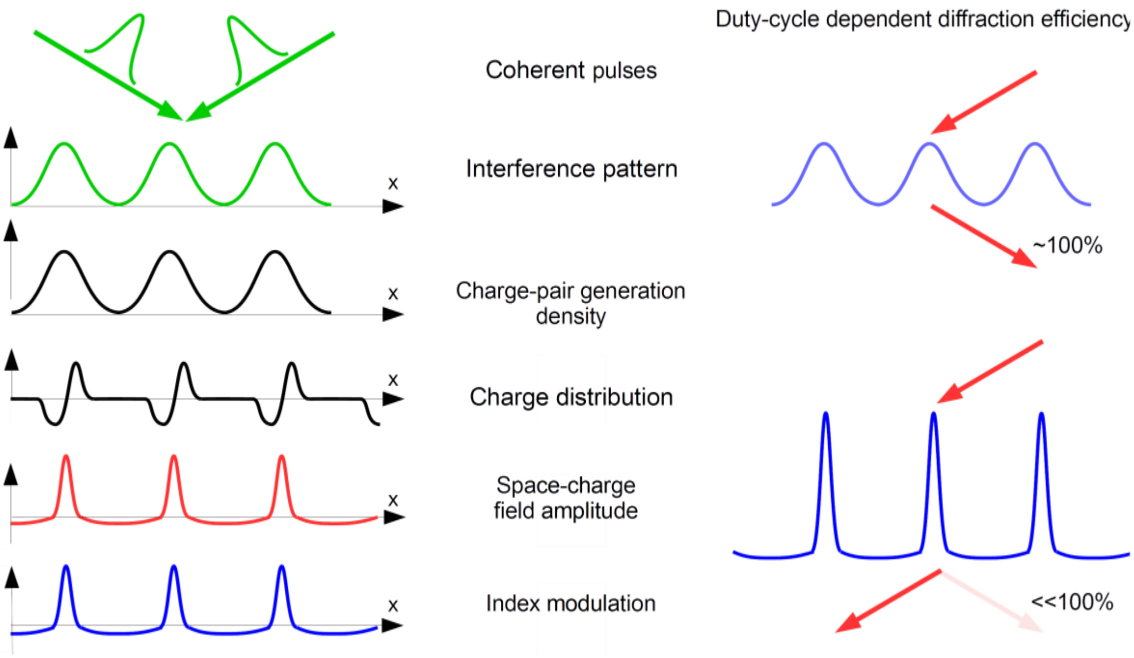

Figure 4-4: (left) Effect of short pulse illumination on the photoelectric and orientational response of the photorefractive polymer. (right) Effect of the refractive index modulation duty cycle on the diffraction efficiency.

These result in the reduction in diffraction efficiency with decreasing pulse energy, as seen in Figure 4-3.

At constant pulse energy, longer pulses expose the material with a lower instantaneous flux, but the exposure time is longer, with continuous illumination supporting multiple excitation/transport/absorption events for each charge carrier until it reaches a dark fringe (Figure 1-1). As the illumination time decreases below the threshold necessary for transport across the fringe spacing, the charge distribution is no longer sinusoidal in form. The duty cycle of the space-charge field begins to decrease, while the peak-to-peak value increases due to the smaller separation of the same population of charges. Figure 4-4 illustrates the extreme case in this scenario in which only a single excitation/transport/absorption event occurs, and the duty cycle of the resulting refractive index modulation is significantly less than the optimal 0.5. The

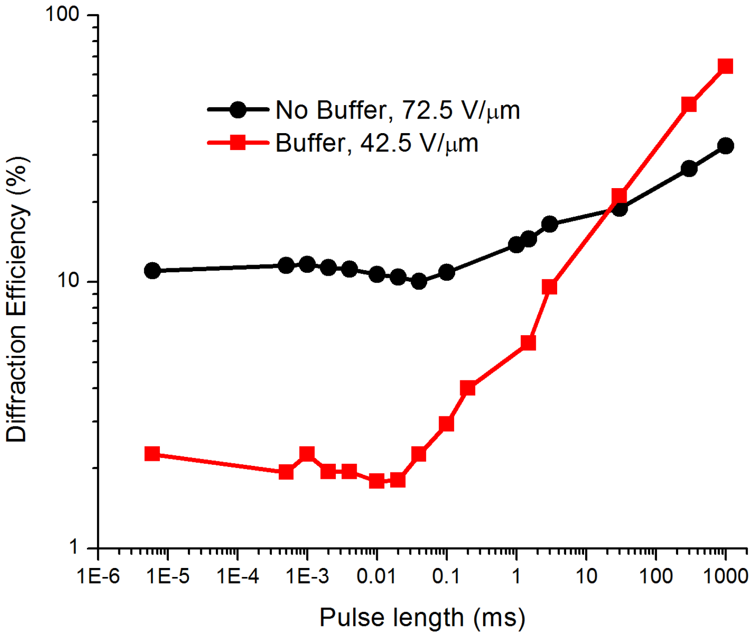

Figure 4-5: Diffraction efficiency across range of pulse lengths with (red squares) and without (black circles) a buffer layer.

right side of Figure 4-4 illustrates the effect that this duty cycle change has on the efficiency of diffraction from the grating itself, following a $\sin^2$(duty cycle) relation.

For pulses shorter than about 20 μs, decreasing the pulse width causes no significant effect on the diffraction efficiency, indicating that a minimum of a single excitation/transport event has been reached. As shown in Figure 4-3, the region of interest for 30 Hz update rate is in the 1 μs to 10 μs pulse width range, but the performance of this single APC buffer layer device is relatively weak. In discovering that the response is constant in this region, no gains can be made by shifting the pulse length. Additionally, for all parameters the response time was too long for video-rate refresh rates, indicating changes in device geometry were necessary in order to reach the required performance.

Faster response speed can be achieved by increasing the bias applied across the sample, increasing the rate of charge generation, transport, and chromophore orientation. In the case of

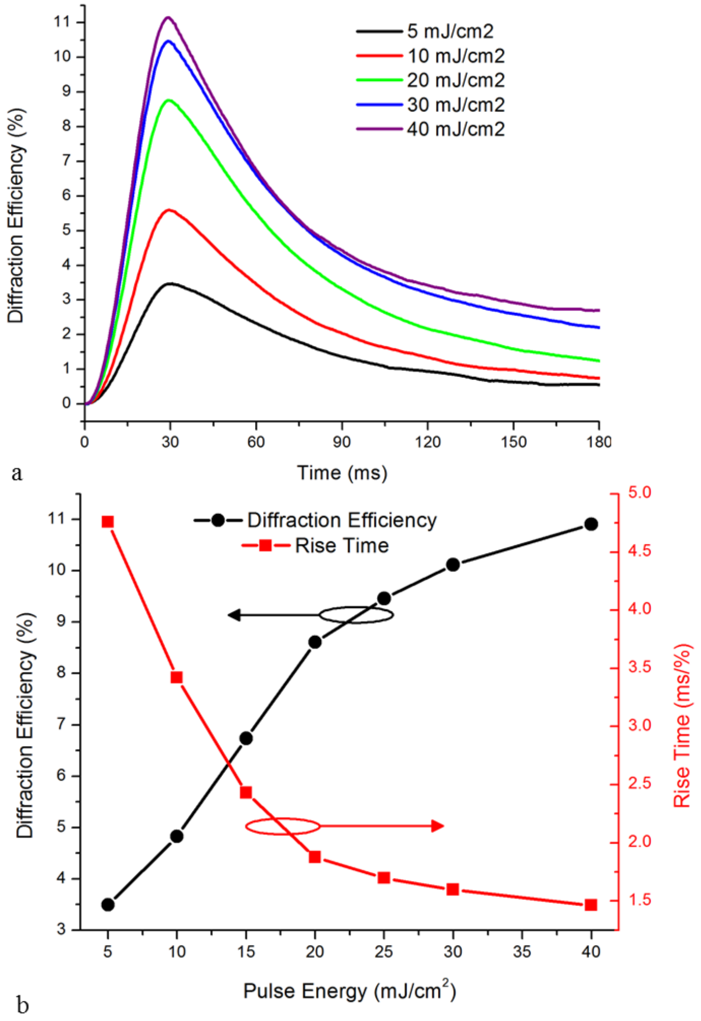

Figure 4-6: 10 µs pulse length FWM results of AS-J2 (no buffer) showing a) diffraction grating growth and decay dynamics for various pulse energies and b) peak diffraction efficiency and rise time in units of ms/% diffraction efficiency.

the buffered samples, increasing the bias above the working voltage of 42.5 V/µm causes the refractive index modulation to increase and the overall diffraction efficiency to decrease, as indicated in Figure 1-26 for a value of ν larger than π/2. Prior works had achieved diffraction efficiencies of greater than 50 % and response times of 1.8 ms, but these devices required a bias of 95 V/µm to exhibit this behavior. At such high voltages applied across the device, the lifetime of the display device shortens significantly.[28] Generally, the response of novel formulations and geometries are characterized using CW illumination, with the goal being high speeds and diffraction efficiencies for exposure times longer than a few seconds. In this case, the system optimized by the integration of a buffer layer was designed for high performance at long exposures and was not optimal for use in short pulse applications.

Removing the buffer layer on subsequent AS-J2 samples samples and working under a bias of 72.5 V/μm increased the maximum diffraction efficiency by shifting the over-modulation inflection to higher voltage and increasing the speed of the grating formation, resulting in much faster recording dynamics. Figure 4-5 shows the pulse length dependent diffraction efficiency for both the devices with (red squares) and without (black circles) the buffer layer. At constant pulse energy of 30 mJ/cm^2, the diffraction efficiency of the unbuffered device in response to pulses shorter than 1 ms remains constant, but compared to the performance of the buffered device in this range, the magnitude of the diffraction efficiency increased by a factor of five from 2.1 % to 11 %. The speed of the response also saw a 5x improvement, with the time of grating formation decreasing from 82 ms to 16 ms. Longer exposures show the expected increase in diffraction efficiency as the number of transport events increases, but the peak efficiency is limited to 32 %, due to the fast response of the device, causing it to be more sensitive to environmental instabilities such as vibrations and air currents. Figure 4-6a shows the refractive index grating growth and decay dynamics in response to 10 μs pulses of various energies. The constant time to peak diffraction indicates that the 10 μs pulse is well within the single charge excitation/transport event regime while the increase in peak diffraction efficiency (and rate of rise) with increasing pulse energy appears to slow above 20 mJ/cm^2 and nears saturation above 30 mJ/cm^2 (Figure 4-6b). The rise time shown on the right axis of Figure 4-6b is defined as the ratio of the peak diffraction efficiency to the time required to achieve that response. More diffraction in the same period of time results in a reduced rise time. These trends indicate that there is negligible benefit to increasing the pulse energy above 30 mJ/cm^2 with respect to increasing the speed or magnitude of the diffractive response.

4.4 Conclusions

Photorefractive polymer devices have been developed which perform five times better in both diffraction efficiency and grating formation speed than the currently implemented systems using a pulsed laser for updatable displays. These results were achieved at 72.5 V/µm, significantly lower than the previously high-performing and fast devices. The new kHz repetition rate, variable pulse width laser enabled unprecedented characterizations of these devices within the range necessary for video-rate recording, proving that the un-buffered AS-J2 devices provide the transition to the regime necessary for implementation of a real-time updatable display, with a 5x improvement in both diffraction efficiency and recording speed Future work includes optimizing the laser for performance at 10 kHz, and in the 1 ms pulse regime. Additionally, the final design and implementation stage of the video-rate holographic display system can begin.

5 CONCLUSION AND OUTLOOK

Recent advances described in this work have brought the actuality of real-time updating holographic displays closer than ever. Work on improving the writing geometry led to new understandings with respect to the limits of current models that predict photorefractive polymer behavior in response to externally applied electric fields. Interdigitated electrodes generate extremely inhomogeneous electric fields throughout the bulk of the medium, in contrast to the uniform field obtained with the standard sandwich configuration electrodes. As the magnitude, speed and uniformity of diffraction from a photorefractive grating is intricately tied to these fields, deeper understanding was necessary to effectively design and optimize electrode geometries. In order to do this, the electric-field enhanced second harmonic generation (EFISHG) technique was used to directly image the orientation of the chromophores to the electric field. The observed response was used to adjust the standard model of refractive index modulation in PR polymer devices to take into account the non-uniform electric fields. The corrected PR response model was used to calculate the recorded holographic gratings and enabled predictions of diffraction uniformity across the beam through computational wavefront propagation.

Observations of diffracted beam uniformity made by imaging the diffracted field of a four-wave mixing measurement correlate to the model predictions, indicating that this model is valid in predicting the effect of the coplanar geometries, including the extreme field magnitude regions. Future work will include using this validated model to optimize the electrode parameters for maximum diffraction uniformity. These devices will then be fabricated for further testing and characterization.

Another area of advancement in this work was the shift from PR devices that had been optimized to work with the 6 ns 50 Hz laser. The development of a new kHz repetition rate, variable pulse width laser enabled new characterizations of these devices within the range necessary for video-rate recording, showing that some of these optimizations were counter productive to the higher repetition rates of real-time update. Photorefractive polymer devices have been developed which perform five times better in both diffraction efficiency and grating formation speed than those currently implemented in pulsed writing displays. These results were achieved at 72.5 V/µm, significantly lower than the 95 V/µm required for the previously high-performing and fast devices, lengthening the device lifetime considerably. The un-buffered AS-J2 devices provide the transition to the regime necessary for implementation of a real-time updatable display. The laser parameters can now be optimized to match the material characteristics and the final design stages on the video-rate display mechanical system can begin.

The APC buffer layer that was removed from these devices does play a role in reducing the probability of dielectric breakdown as it reduces the conductivity between the two electrodes. The edge of the electrodes is where the majority of breakdown occurs since the sharp edges concentrate the electric field. If a non-conductive buffer is applied only in these regions of high electric field concentration, device lifetimes can be extended while maintaining the diffraction speed and magnitude gains made in this study.

Results from the variable pulse length measurements indicate that an exposure time threshold of charge transport exists. Pulses shorter than this time result in decreasing diffraction efficiency due to a combination of photo-electric and diffractive effects. The standard methods of testing material parameters such as space-charge field formation depend on the assumption that the final refractive index modulation is sinusoidal in form. In this case, this assumption is not valid and a new method of determining characteristic parameters is necessary in this time regime. Imaging the space-charge field formation in response to the illumination pattern and external field could be done using a method such as EFM or conductive tip AFM. Direct measurement of the refractive index modulation within the material could be performed with a high resolution interferometric method, which combined with the new space-charge understanding would lead to an entirely new regime of PR dynamic models.

Novel methods of sensitization have been a hot topic since the explosion of C_{60} alternatives was jump started by the interest in organic solar cell research. Preliminary photoconductivity data indicating that molecules such as single walled carbon nanotubes and perylene bisimides are viable options has been collected but additional research needs to be performed to validate the gain and diffractive characteristics of these compounds. One difficulty in the integration of new species is matching the solubility with that of the host polymer and other moieties. Functionalization of sensitizers for use in this type of highly doped system also has significant room to progress.

Another direction of advancement in PR improvement is in the conductive polymer host, currently PATPD. In the last few years, a number of conductive alternatives have come on the market but characterizing the improvement of the entire composite is difficult. Most of the more straight forward methods employed do not distinguish between electron and hole transport, and mobilities in such dispersively transporting polymer blends are typically difficult to pinpoint with any accuracy. In light of the extreme sensitivity of the EFISHG technique to conductivity that was observed, this method may be valuable in future studies of new conductive polymers for PR applications.

REFERENCES

1 D. Gabor, “A new microscopic principle,” *Nature* **161**, 777–778 (1948).

2 H. Kogelnik, “Coupled wave theory for thick hologram gratings,” *Bell Syst. Tech. J.* **48**(9), 2909–2947 (1969).

3 T.A. Shankoff, “Phase holograms in dichromated gelatin,” *Appl. Opt.* **7**(10), 2101–2105 (1968).

4 D.H. Close, A.D. Jacobson, J.D. Margerum, R.G. Brault, and F.J. McClung, “Hologram Recording on Photopolymer Materials,” *Appl. Phys. Lett.* **14**(5), 159–160 (1969).

5 P.-A. Blanche *et al.*, “Holographic three-dimensional telepresence using large-area photorefractive polymer,” *Nature* **468**(7320), 80–83 (2010).

6 S. Jolly, “Direct fringe writing architecture for photorefractive polymer-based holographic displays: analysis and implementation,” *Opt. Eng.* **52**(5), 055801 (2013).

7 M. Salvador *et al.*, “Three-dimensional holographic imaging of living tissue using a highly sensitive photorefractive polymer device,” *Opt. Express* **17**(14), 11834–11849 (2009).

8 Y. Suzuki, P. Lai, X. Xu, and L. V Wang, “High-sensitivity ultrasound-modulated optical tomography with a photorefractive polymer.,” *Opt. Lett.* **38**(6), 899–901 (2013).

9 A. Ashkin *et al.*, “Optically-induced refractive index homogeneities in LiNb03 and LiTa03,” *Appl. Phys. Lett.* **9**(1), 72–74 (1966).

10 F.S. Chen, “A laser-induced inhomogeneity of refractive indices in KTN,” *J. Appl. Phys.* **38**(8), 3418–3420 (1967).

11 F.S. Chen, J.T. LaMacchia, and D.B. Fraser, “Holographic storage in lithium niobate,” *Appl. Phys. Lett.* **13**(7), 223–225 (1968).

12 S. Ducharme, J.C. Scott, R.J. Twieg, and W.E. Moerner, “Observation of the photorefractive effect in a polymer,” *Phys. Rev. Lett.* **66**(14), 1846–1849 (1991).

13 K. Meerholz, B.L. Volodin, Sandalphon, B. Kippelen, and N. Peyghambarian, “A photorefractive polymer with high optical gain and diffraction efficiency near 100%,” *Nature* **371**, 497–500 (1994).

14 M. Eralp *et al.*, “Photorefractive polymer device with video-rate response time operating at low voltages.,” *Opt. Lett.* **31**(10), 1408–1410 (2006).

15 D.P. West and D.J. Binks, *Physics of photorefraction in polymers* (CRC Press, Florida, 2005).

16 P. Yeh, *Introduction to Photorefractive Nonlinear Optics* (John Wiley & Sons, Inc., New York, 1993).

17 W.E. Moerner, S.M. Silence, F. Hache, and G.C. Bjorklund, “Orientationally enhanced photorefractive effect in polymers,” *J. Opt. Soc. Am. B* **11**(2), 320–330 (1994).

18 M.G. Moharam and L. Young, “Hologram writing by the photorefractive effect,” *J. Appl. Phys.* **48**(8), 3230–3236 (1977).

19 N. V Kukhtarev, V.B. Markov, S.G. Odulov, M.S. Soskin, and V.L. Vinetskii, “Holographic storage in electrooptic crystals . i . steady state,” *Ferroelectrics* **22**(September), 949–960 (1979).

20 J.S. Schildkraut and A. V Buettner, “Theory and simulation of the formation and erasure of space-charge gratings in photoconductive polymers,” *J. Appl. Phys.* **72**(5), 1888–1893 (1992).

21 J.S. Schildkraut and Y. Cui, “Zero-order and first-order theory of the formation of space-charge gratings in photoconductive polymers,” *J. Appl. Phys.* **72**(11), 5055–5060 (1992).

22 O. Ostroverkhova and K.D. Singer, "Space-charge dynamics in photorefractive polymers," *J. Appl. Phys.* **92**(4), 1727–1743 (2002).

23 J.-W. Oh, C. Lee, and N. Kim, "Influence of chromophore content on the steady-state space charge formation of poly[methyl-3-(9-carbazolyl) propylsiloxane]-based polymeric photorefractive composites," *J. Appl. Phys.* **104**(7), 073709 (2008).

24 J.-W. Oh, C. Lee, and N. Kim, "The effect of trap density on the space charge formation in polymeric photorefractive composites.," *J. Chem. Phys.* **130**(13), 134909 (2009).

25 J.H. Slowik and I. Chen, "Effect of molecular rotation upon charge transport between disordered carbazole units," *J. Appl. Phys.* **54**(8), 4467–4473 (1983).

26 N. Martinelli *et al.*, "Charge Transport in Organic Semiconductors: A Multiscale Modeling," in *Funct. Supramol. Archit.*, edited by P. Samori and F. Cacialli (Wiley-VCH, Weinheim, 2011), pp. 3–37.

27 A. Hagfeldt, G. Boschloo, L. Sun, L. Kloo, and H. Pettersson, "Dye-sensitized solar cells.," *Chem. Rev.* **110**(11), 6595–663 (2010).

28 M. Eralp *et al.*, "Submillisecond response of a photorefractive polymer under single nanosecond pulse exposure," *Appl. Phys. Lett.* **89**(11), 114105 (2006).

29 S. Kober *et al.*, "Influence of the sensitizer reduction potential on the sensitivity of photorefractive polymer composites," *J. Mater. Chem.* **20**(29), 6170–6175 (2010).

30 N. Tsutsumi, K. Kinashi, A. Nonomura, and W. Sakai, "Quickly updatable hologram images using poly(N-vinyl carbazole) (PVCz) photorefractive polymer composite," *Materials (Basel).* **5**(12), 1477–1486 (2012).

31 F. Gallego-Gomez *et al.*, "Millisecond photorefractivity with novel dicyanomethylenedihydrofuran-containing polymers," *J. Mater. Chem.* **22**(24), 12220–12228 (2012).

32 A.D. Grishina, T. V Krivenko, V. V Savel'ev, R.W. Rychwalski, and A. V Vannikov, "Photoelectric, nonlinear optical, and photorefractive properties of polyvinylcarbazole composites with graphene," *High Energ. Chem.* **47**(2), 46–52 (2013).

33 X. Li, J.W.M. Chon, and M. Gu, "Nanoparticle-based photorefractive polymers," *Aust. J. Chem.* **61**, 317–323 (2008).

34 T.K. Daubler, R. Bittner, K. Meerholz, V. Cimrova, and D. Neher, "Charge carrier photogeneration , trapping , and space-charge field formation in PVK-based photorefractive materials," *Phys. Rev. B* **61**(20), 515–527 (2000).

35 L. Onsager, "Deviations from Ohm's Law in Weak Electrolytes," *J. Chem. Phys.* **2**(9), 599–615 (1934).

36 L. Onsager, "Initial Recombination of Ions," *Phys. Rev.* **54**, 554–557 (1938).

37 J. Noolandi and K.M. Hong, "Theory of photogeneration and fluorescence quenching," *J. Chem. Phys.* **70**(7), 3230–3236 (1979).

38 O. Ostroverkhova and W.E. Moerner, "Organic photorefractives: mechanisms, materials, and applications.," *Chem. Rev.* **104**(7), 3267–3314 (2004).

39 J. Merski, "Piezomodulation spectroscopy of molecular crystals. I. Methods and principles," *J. Chem. Phys.* **75**(8), 3691–3704 (1981).

40 L.E. Lyons, "Photo- and semi-conductance in organic crystals. Part V. Ionized states in molecular crystals," *J. Chem. Soc.* 5001–5007 (1957).

41 C.L. Braun, "Electric field assisted dissociation of charge transfer states as a mechanism of photocarrier production," *J. Chem. Phys.* **80**(9), 4157–4161 (1984).

42 E. Hendrickx, B. Kippelen, S. Thayumanavan, S.R. Marder, A. Persoons, and N. Peyghambarian, "High photogeneration efficiency of charge-transfer complexes formed between low ionization potential arylamines and C60 between low ionization potential arylamines and C 60," *J. Chem. Phys.* **112**(21), 9557–9561 (2000).

43 G. Weiser, "Absorption and Electroabsorption on Amorphous Films of Polyvinylcarbazoie and Trinitrofluorenone," *Phys. Stat. Sol. A* **18**, 347–359 (1973).

44 G. Weiser, "Densities of complexed and uncomplexed molecules in amorphous films of trinitrofluorenone and polynvinylcarbazole," *J. Appl. Phys.* **43**(12), 5028–5033 (1972).

45 M. Fuoss and F. Accascina, *Electrolytic Conductance* (Interscience, New York, 1959).

46 P.M. Borsenberger and D.S. Weiss, *Organic photoreceptors for xerography* (Marcel Dekker, Inc., New York, 1998).

47 K.-Y. Law, "Organic Photoconductive Materials: Recent Trends and Developments," *Chem. Rev.* **93**, 449–486 (1993).

48 A. Grunnet-Jepsen *et al.*, "Spectroscopic determination of trap density in C 60 -sensitized photorefractive polymers," *Chem. Phys. Lett.* **291**, 553–561 (1998).

49 J. Ashley *et al.*, "Holographic data storage," *IBM J. Res. Dev.* **44**(3), 341–368 (2000).

50 J. Thomas, C.W. Christenson, P.-A. Blanche, M. Yamamoto, R.A. Norwood, and N. Peyghambarian, "Photoconducting polymers for photorefractive 3D display applications," *Chem. Mater.* **23**, 416–429 (2011).

51 S.M. Silence *et al.*, "Subsecond grating growth in a photorefractive polymer," *Opt. Lett.* **17**(16), 1107–1109 (1992).

52 I.K. Moon, J. Choi, and N. Kim, "High-Performance Photorefractive Composite Based on Non-conjugated Main-Chain, Hole-Transporting Polymer," *Macromol. Chem. Phys.* **214**(4), 478–485 (2013).

53 K. Ditte, W. Jiang, T. Schemme, C. Denz, and Z. Wang, "Innovative sensitizer DiPBI outperforms PCBM.," *Adv. Mater.* **24**(16), 2104–2108 (2012).

54 A. V Vannikov *et al.*, "Photorefractive Polymer Composites for the IR Region Based on Carbon Nanotubes," *Opt. Spectrosc.* **99**(4), 643–648 (2005).

55 N.K. Lingam, S. Kalghatgi, and J.G. Winiarz, "Enhanced photorefractivity in a polymeric composite photosensitized with carbon nanotubes grafted to a photoconductive polymer," *J. Appl. Phys.* **109**(2), 023106 (2011).

56 A. V Vannikov, A.D. Grishina, A.S. Laryushkin, T. V Krivenko, V. V Savel'ev, and R.W. Rychwalski, "Photoelectric, nonlinear optical, and photorefractive properties of polymer composites including carbon nanotubes and cyanine dyes," *Phys. Solid State* **55**(3), 572–580 (2013).

57 F. Gallego-Gomez *et al.*, "Phthalocyanines as Efficient Sensitizers in Low- T g Hole-Conducting Photorefractive Polymer Composites," *Chem. Mater.* **21**(13), 2714–2720 (2009).

58 F. Aslam and C. von Ferber, "Shape dependent properties of CdSe nanostructures," *Chem. Phys.* **362**(3), 114–119 (2009).

59 C. Fuentes-Hernandez, D.J. Suh, B. Kippelen, and S.R. Marder, "High-performance photorefractive polymers sensitized by cadmium selenide nanoparticles," *Appl. Phys. Lett.* **85**(4), 534–536 (2004).

60 J.G. Winiarz, "Enhancement of the Photorefractive Response Time in a Polymeric Composite Photosensitized with CdTe Nanoparticles," *J. Phys. Chem. C* **111**(5), 1904–1911 (2007).

61 J.G. Winiarz, L. Zhang, M. Lal, C.S. Friend, and P.N. Prasad, “Photogeneration , charge transport , and photoconductivity of a novel PVK/CdS-nanocrystal polymer composite,” *Chem. Phys.* **245**, 417–428 (1999).

62 X. Li, J. Van Embden, R.A. Evans, and M. Gu, “Type-II core/shell nanoparticle induced photorefractivity,” *Appl. Phys. Lett.* **98**(23), 231107 (2011).

63 J. Zhu *et al.*, “Enhanced photorefractivity in a polymer/nanocrystal composite photorefractive device at telecommunication wavelength,” *Appl. Phys. Lett.* **97**(26), 263108 (2010).

64 C. Li, X. Li, L. Cao, G. Jin, and M. Gu, “Exciton-plasmon coupling mediated photorefractivity in gold-nanoparticle- and quantum-dot-dispersed polymers,” *Appl. Phys. Lett.* **102**, 251115 (2013).

65 M. Grell, “Organic light emitting devices,” in *Handb. Optoelectron.*, edited by J.P. Dakin and R.G.W. Brown (CRC Press, Boca Raton, 2006), pp. 693–718.

66 S.J. Zilker, “Materials Design and Physics of Organic Photorefractive Systems,” *ChemPhysChem* **1**(2), 72–87 (2000).

67 S.L. Rosen, *Fundamental principles of polymeric materials*, 2nd ed. (John Wiley & Sons, Inc., New York, 1993).

68 H. Li, R. Termine, N. Godbert, L. Angiolini, L. Giorgini, and A. Golemme, “Charge photogeneration and transport in side-chain carbazole polymers and co-polymers,” *Org. Electron.* **12**(7), 1184–1191 (2011).

69 R.A. Marcus, “Electron transfer reactions in chemistry. Theory and experiment,” *Rev. Mod. Phys.* **65**(3), 599–610 (1993).

70 P.M. Borsenberger and J.J. Fitzgerald, “Effects of the Dipole Moment on Charge Transport in Disordered Molecular Solids,” *J. Phys. Chem.* **97**, 4815–4819 (1993).

71 A. Dieckmann, H. Bässler, and P.M. Borsenberger, “An assessment of the role of dipoles on the density-of-states function of disordered molecular solids,” *J. Chem. Phys.* **99**(10), 8136–8141 (1993).

72 M. Van der Auweraer, F.C. De Schryver, P.M. Borsenberger, and H. Bassler, “Disorder in charge transport in doped polymers,” *Adv. Mater.* **6**(3), 199–213 (1994).

73 P.F. Barbara, T.J. Meyer, and M.A. Ratner, “Contemporary issues in electron transfer research,” *J. Phys. Chem.* **100**, 13148–13168 (1996).

74 J.-L. Brédas, D. Beljonne, V. Coropceanu, and J. Cornil, “Charge-transfer and energy-transfer processes in pi-conjugated oligomers and polymers: a molecular picture.,” *Chem. Rev.* **104**(11), 4971–5004 (2004).

75 V. Coropceanu, J. Cornil, D.A. da Silva Filho, Y. Oliver, R. Silbey, and J.-L. Bredas, “Charge transport in organic semiconductors,” *Chem. Rev.* **107**, 926–952 (2007).

76 W.E. Moerner and S.M. Silence, “Polymeric photorefractive materials,” *Chem. Rev.* **94**(1), 127–155 (1994).

77 P.P. Banerjee *et al.*, “Time dynamics of self-pumped reflection gratings in a photorefractive polymer,” *J. Appl. Phys.* **111**(1), 013108 (2012).

78 F. Würthner and K. Meerholz, “Systems chemistry approach in organic photovoltaics.,” *Chem. Eur. J.* **16**(31), 9366–9373 (2010).

79 A. Goonesekera and S. Ducharme, “Effect of dipolar molecules on carrier mobilities in photorefractive polymers,” *J. Appl. Phys.* **85**(9), 6506–6514 (1999).

80 L.B. Schein, A. Rosenberg, and S.L. Rice, "Hole transport in a molecularly doped polymer: p-diethylaminobenzaldehyde-diphenyl hydrazone in polycarbonate," *J. Appl. Phys.* **60**(12), 4287–4292 (1986).
81 Y. Zhang, Y. Cui, and P.N. Prasad, "Observation of photorefractivity in a fullerene-doped polymer composite," *Phys. Rev. B* **46**(15), 9900–9902 (1992).
82 W.D. Gill, "Drift mobilities in amorphous charge-transfer complexes of trinitrofluorenone and poly-n-vinylcarbazole," *J. Appl. Phys.* **43**(12), 5033–5040 (1972).
83 S. Mansurova, K. Meerholz, E. Sliwinska, U. Hartwig, and K. Buse, "Enhancement of charge carrier transport by doping PVK-based photoconductive polymers with LiNbO3 nanocrystals," *Phys. Rev. B* **79**(17), 174208 (2009).
84 K. Kinashi, Y. Wang, W. Sakai, and N. Tsutsumi, "Optimization of Photorefractivity Based on Poly(N -vinylcarbazole) Composites: An Approach from the Perspectives of Chemistry and Physics," *Macromol. Chem. Phys.* **214**(16), 1789–1797 (2013).
85 J.A. Herlocker *et al.*, "Stabilization of the response time in photorefractive polymers," *Appl. Phys. Lett.* **77**(15), 2292–2294 (2000).
86 I.K. Moon, C.-S. Choi, and N. Kim, "Synthesis and photorefractivity of polysiloxanes bearing hole-conductors doped with a nonlinear optical chromophore," *Opt. Mater.* **31**(6), 1017–1021 (2009).
87 J.-W. Oh, I.K. Moon, and N. Kim, "The influence of photosensitizers on the photorefractivity in poly[methyl-3-(9-carbazolyl)propylsiloxane]-based composites," *J. Photochem. Photobiol., A* **201**(2-3), 222–227 (2009).
88 H. Chun, I.K. Moon, D.-H. Shin, and N. Kim, "Preparation of Highly Efficient Polymeric Photorefractive Composite Containing an Isophorone-Based NLO Chromophore," *Chem. Mater.* **13**, 2813–2817 (2001).
89 J. Wolff, S. Schloter, U. Hofmann, D. Haarer, and S.J. Zilker, "Speed enhancement of photorefractive polymers by means of light-induced filling of trapping states," *J. Opt. Soc. Am. B* **16**(7), 1080–1086 (1999).
90 O.-P. Kwon, S.-H. Lee, G. Montemezzani, and P. Günter, "Layer-Structured Photoconducting Polymers: A New Class of Photorefractive Materials," *Adv. Funct. Mater.* **13**(6), 434–438 (2003).
91 O. Kwon, S. Lee, G. Montemezzani, and P. Günter, "Highly efficient photorefractive composites based on layered photoconductive polymers," *J. Opt. Soc. Am. B* **20**(11), 2307–2312 (2003).
92 O.-P. Kwon, S.-J. Kwon, M. Jazbinsek, P. Günter, and S.-H. Lee, "Layered photoconductive polymers: anisotropic morphology and correlation with photorefractive reflection grating response.," *J. Chem. Phys.* **124**(10), 104705 (2006).
93 K. Ogino, T. Nomura, T. Shichi, S. Park, and H. Sato, "Synthesis of Polymers Having Tetraphenyldiaminobiphenyl Units for a Host Polymer of Photorefractive Composite," *Chem. Mater.* **9**, 2768–2775 (1997).
94 J. Thomas *et al.*, "Bistriarylamine Polymer-Based Composites for Photorefractive Applications," *Adv. Mater.* **16**(22), 2032–2036 (2004).
95 S. Tay *et al.*, "An updatable holographic three-dimensional display.," *Nature* **451**(7179), 694–698 (2008).
96 U. Bach, K. De Cloedt, H. Spreitzer, and M. Gratzel, "Characterization of Hole Transport in a New Class of Spiro-Linked Oligotriphenylamine Compounds," *Adv. Mater.Mater.* **12**, 1060–1063 (2000).

97 N. Tsutsumi, T. Murao, and W. Sakai, “Photorefractive response of polymeric composites with pendant triphenylamine moiety,” *Macromolecules* **38**, 7521–7523 (2005).

98 S. Tsujimura, K. Kinashi, W. Sakai, and N. Tsutsumi, “High-Speed Photorefractive Response Capability in Triphenylamine Polymer-Based Composites,” *Appl. Phys. Express* **5**(6), 064101 (2012).

99 S.R. Marder, B. Kippelen, A.K.-Y. Jen, and N. Peyghambarian, “Design and synthesis of chromophores and polymers for electro-optic and photorefractive applications,” *Nature* **388**, 845–851 (1997).

100 B. Kippelen, “Organic photorefractive materials and their applications,” in *Photorefractive Mater. their Appl. 2*, edited by P. Günter and J.-P. Huignard (Springer New York, New York, NY, 2006), pp. 487–534.

101 J.W. Wu, “Birefringent and electro-optic effects in poled polymer films: steady-state and transient properties,” *J. Opt. Soc. Am. B* **8**(1), 142–152 (1991).

102 B. Kippelen, F. Meyers, N. Peyghambarian, and S.R. Marder, “Chromophore design for photorefractive applications,” *J. Am. Chem. Soc.* **119**, 4559–4560 (1997).

103 F. Würthner, R. Wortmann, and K. Meerholz, “Chromophore design for photorefractive organic materials.,” *ChemPhysChem* **3**(1), 17–31 (2002).

104 D.P. West, M.D. Rahn, C. Im, and H. Bässler, “Hole transport through chromophores in a photorefractive polymer composite based on poly(N-vinylcarbazole),” *Chem. Phys. Lett.* **326**(5-6), 407–412 (2000).

105 M.A. Diaz-Garcia, D. Wright, J.D. Casperson, B. Smith, E. Glazer, and W.E. Moerner, “Photorefractive Properties of Poly (N -vinyl carbazole)-Based Composites for High-Speed Applications,” *Chem. Mater.* **11**, 1784–1791 (1999).

106 W. You, S. Cao, Z. Hou, and L. Yu, “Fully Functionalized Photorefractive Polymer with Infrared Sensitivity Based on Novel Chromophores,” *Macromolecules* **36**, 7014–7019 (2003).

107 V.-M. Herrera-Ambriz *et al.*, “Highly Efficient Photorefractive Organic Polymers Based on Benzonitrile Shiff Bases Nonlinear Chromophores,” *J. Phys. Chem. C* **115**, 23955–23963 (2011).

108 J.K. Fink, *High Performance Polymers* (William Andrew Inc., Norwich, 2008).

109 S. Kober, M. Salvador, and K. Meerholz, “Organic photorefractive materials and applications,” *Adv. Mater.* **23**, 4725–4763 (2011).

110 N. Cheng, B. Swedek, and P.N. Prasad, “Thermal fixing of refractive index gratings in a photorefractive polymer,” *Appl. Phys. Lett.* **71**(13), 1828–1830 (1997).

111 G. Li and P. Wang, “Efficient local fixing of photorefractive polymer hologram using a laser beam.,” *Appl. Phys. Lett.* **96**(11), 111109 (2010).

112 J. Thomas, R.A. Norwood, and N. Peyghambarian, “Non-linear optical polymers for photorefractive applications,” *J. Mater. Chem.* **19**(40), 7476–7489 (2009).

113 R. V Johnson and A.R. Tanguay Jr, “Stratified volume holographic optical elements,” *Opt. Lett.* **13**(3), 189–191 (1988).

114 G.P. Nordin and A.R. Tanguay Jr, “Photopolymer-based stratified volume holographic optical elements.,” *Opt. Lett.* **17**(23), 1709–11 (1992).

115 J.J. Stankus, S.M. Silence, W.E. Moerner, and G.C. Bjorldund, “Electric-field-switchable stratified volume holograms in photorefractive polymers.,” *Opt. Lett.* **19**(18), 1480–1482 (1994).

116 R. De Vre and L. Hesselink, “Diffraction analysis of layered structures of photorefractive gratings,” *J. Opt. Soc. Am. A* **13**(2), 285–295 (1996).

117 A. Grunnet-Jepsen, C.L. Thompson, and W.E. Moerner, “Spontaneous Oscillation and Self-Pumped Phase Conjugation in a Photorefractive Polymer Optical Amplifier,” *Science (80-.).* **277**(5325), 549–552 (1997).

118 Y. Hayasaki, N. Ishikura, H. Yamamoto, and N. Nishida, “Thick photorefractive polymer device with coplanar electrodes,” *Rev. Sci. Instrum.* **74**(8), 3693–3696 (2003).

119 C.W. Christenson *et al.*, “Interdigitated coplanar electrodes for enhanced sensitivity in a photorefractive polymer,” *Opt. Lett.* **36**(17), 3377–3379 (2011).

120 S.A. Benton and V.M. Bove, Jr., *Holographic imaging* (Wiley-InterScience, New York, 2008).

121 C.W. Christenson *et al.*, “Materials for an Updatable Holographic 3D Display,” *J. Disp. Technol.* **6**(10), 510–516 (2010).

122 B. Lynn *et al.*, “Recent advancements in photorefractive holographic imaging,” *J. Phys. Conf. Ser.* **415**, 012050 (2013).

123 L.R. Dalton, A.W. Harper, and B.H. Robinson, “The role of London forces in defining noncentrosymmetric order of high dipole moment-high hyperpolarizability chromophores in electrically poled polymeric thin films,” *Proc. Natl. Acad. Sci. USA* **94**(May), 4842–4847 (1997).

124 M. Born and E. Wolf, *Principles of Optics*, 7th ed. (Cambridge University Press, Cambridge, 1999).

125 C. Bosshard, J. Hulliger, M. Florsheimer, and P. Gunter, *Organic Nonlinear Optical Materials* (2001).

126 R.W. Boyd, *Nonlinear Optics*, 3rd ed. (Elsevier Science, Philidelphia, 2008).

127 K. Kieu, S. Mehravar, R. Gowda, R.A. Norwood, and N. Peyghambarian, “Label-free multi-photon imaging using a compact femtosecond fiber laser mode-locked by carbon nanotube saturable absorber,” *Biomed. Opt. Express* **4**(10), 334–336 (2013).

128 K. Kieu and M. Mansuripur, “Femtosecond laser pulse generation with a fiber taper embedded in carbon nanotube / polymer composite,” *Opt. Lett.* **32**(15), 2242–2244 (2007).

129 M. Mansuripur, *Classical Optics and its Application*, 2nd ed. (Cambridge University Press, Cambridge, 2009).

130 K.D. Singer *et al.*, “Electro-optic phase modulation and optical second-harmonic generation in corona-poled polymer films,” *Appl. Phys. Lett.* **53**(19), 1800 (1988).

131 O. Ostroverkhova, A. Stickrath, and K.D. Singer, “Electric field-induced second harmonic generation studies of chromophore orientational dynamics in photorefractive polymers,” *J. Appl. Phys.* **91**(12), 9481 (2002).

132 G. Lüpke, C. Meyer, C. Ohlhoff, H. Kurz, S. Lehmann, and G. Marowsky, “Optical second-harmonic generation as a probe of electric-field-induced perturbation of centrosymmetric media.,” *Opt. Lett.* **20**(19), 1997–9 (1995).

133 A. V Vannikov, Y.G. Gorbunova, A.D. Grishina, and A.Y. Tsivadze, “Photoelectric, nonlinear optical, and photorefractive properties of polymer composites based on supramolecular ensembles of Ru(II) and Ga(III) complexes with tetra-15-crown-5-phthalocyanine,” *Prot. Met. Phys. Chem. Surf.* **49**(1), 57–65 (2013).

134 W.H. Press, S.A. Teukolsky, W.T. Vetterling, and B.P. Flannery, *Numerical Recipes 3rd Edition: The Art of Scientific Computing*, 3rd ed. (Cambridge University Press, Cambridge, 2007).

135 J. Goodman, *Introduction to Fourier optics*, 3rd ed. (Roberts and Co Publishers, New York, 2005).

136 N.S. Holliman, N.A. Dodgson, G.E. Favalora, and L. Pockett, “Three-dimensional displays: a review and applications analysis,” *IEEE Trans. Broadcast.* **57**(2), 362–371 (2011).